Bunch Length Measurements using Electro-optical Sampling at the SLS Linac

Diplomarbeit
von
Axel Winter

vorgelegt an der
Fakultät für Mathematik, Physik und Informatik
der RWTH Aachen

angefertigt am
Deutschen Elektronen-Synchrotron (DESY) Hamburg

Hamburg, Juni 2004

Gutachter der Diplomarbeit:	Prof. Dr. M. Tonutti (RWTH Aachen)
	Prof. Dr. P. Schmüser (Universität Hamburg)

Abstract

A mode-locked titanium-sapphire laser with 15 fs pulse width is used to determine the time profile of the picosecond electron bunches in the Swiss Light Source linac of the Paul Scherrer Institute, Villigen Switzerland. This was done using the electro-optic effect in Zinc-Telluride crystals and sampling the change induced by coherent transition radiation with the TiSa laser. The development, implementation and results of an analouge synchronisation system to synchronise the repetition rate of the TiSa laser to the radio frequency of the accelerator with a short term stability of 40 fs is presented. The experimental setup of the bunch length measurements is described and results are presented on the coincidence measurements between the laser pulses and the coherent transition radiation pulses generated by the electron bunches.

Zusammenfassung

Im Rahmen dieser Arbeit wird das longitudinale Zeitprofil der Picosekunden langen Elektronenpulse des Linearbeschleunigers der Swiss Light Source des Paul Scherrer Institutes in Villigen durch elektro-optische Abtastung bestimmt. Hierzu wird durch kohärente Übergangsstrahlung der lineare elektro-optische Effekt in einem Zink-Tellurid Kristall induziert, und die resultierende Doppelbrechung des Kristalls wird mit Hilfe eines 15 fs langen TiSa-Laserpulses abgetastet. Der experimentelle Aufbau und die Resultate der Synchronisation der Wiederholrate des TiSa Lasers auf die zentrale Beschleuniger Hochfrequenz mit einer Kurzzeitstabilität von 40 fs wird präsentiert, sowie Aufbau und Resultate der Bunchlängenmessung.

Contents

1. Introduction

Structural research on an atomic and subatomic level is not only important in physics, but also in many other sciences. In order to use light to investigate the microscopic structure of a material, the wavelength of the light has to be smaller than the size of the structure one wishes to investigate. X-rays with a wavelength of below 0.1 nm offer the possibility to resolve atomic structures.
Synchrotron Radiation from circular particle accelerators laid the foundation for the development of a new class of X-ray sources with brilliances (number of photons per area and time) much higher than those of conventional X-ray sources. Third generation synchrotron light sources like the ESRF[1] in Grenoble reach a peak brilliance of up to 1000 photons/$(s \cdot mrad^2 \cdot mm \cdot 0.1\%\Delta\lambda)$. The temporal resolution of a light source is determined by the pulse length of the radiation. Using modern laser systems it is possible to achieve pulse lengths in the femtosecond regime. In 1977 laser radiation using a particle accelerator has been generated at SLAC (Stanford Linear Accelerator Center). Using the SASE[2]-process, the generation of laser radiation is possible without using a laser resonator and thus without mirrors. This enables the expansion of the wavelength regime to the subnanometer level.
Free electron lasers are very promising candidates for X-ray sources of the next generation. They allow the combination of ultrashort laser pulses and the high spatial resolution of X-rays. The XFEL[3], which will begin operating at DESY in 2012, will exceed the brilliance of presently existing facilities by some ten orders of magnitude [Bri02].
The beam quality required by UV and X-ray FELs is very high: small normalised emittance of around 1 mm·mrad, low energy spread of 0.01% and high peak current of several kA in the bunches. These high local charge densities cannot be obtained from the electron gun directly, because the strong internal Coulomb forces would lead to a larger emittance. Therefore the length of the bunches emitted from the gun is in the order of 3 mm. The bunches receive an energy chirp during the acceleration and are compressed using magnetic chicanes to a length of some ten micometers or below. During this compression, the charge does not stay evenly distributed throughout the bunch, so measuring the longitudinal bunch structure is a very important part of beam diagnostics of a free electron laser facility.

[1]European Synchrotron Radiation Facility
[2]Self Amplified Spontanious Emission
[3]European X-ray Free Electron Laser

With a streak camera, the best achievable resolution up to now is around 450 fs [HaSS01].
The technique of electro-optic sampling (EOS) provides the possibility to measure the longitudinal charge distribution with a greatly improved resolution. A crystal showing the Pockels-effect (becoming birefringent when an external electromagnetic field is present) is installed near the electron bunch. The electric field of the relativistic electron bunch induces a transient birefringence which is sampled by a polarised femtosecond laser pulse focused on the crystal. By shifting the phase of the laser pulse relative to the electron bunch, one can obtain a bunch profile measurement by sampling over many bunches.
A birefringent crystal was first used for bunch length measurements using coherent transition radiation coupled out of the beampipe at the infrared free electron laser FELIX[4] in Nieuwegein, the Netherlands [Oep99].
In principal, the resolution of the electro-optic sampling is only limited by the length of the probe laser pulse and the crystal response function. Commercially available lasers today have a pulse length of less than 15 fs. So the technique of electro-optic sampling in principle offers the possibility to measure the longitudinal electron bunch structure with such precision.
One of the principal sources of jitter is the synchronisation between the femtosecond laser and the radio frequency (RF) of the linear accelerator (linac). The repetition rate of the laser is not stable enough to stay intrinsically locked to the RF of the linac. Thus a scheme has to be developed to make sure the frequency of the laser is always synchronous to the linac RF. This is done through a PLL (phase locked loop). The quality of the PLL is one of the key factors toward a very high resolution. The PLL compares the two frequencies and the output is fed back into the laser to regulate the repetition rate. Noise on this error signal directly affects the quality of the PLL. For EOS experiments dealing with bunches of ten μm, a stability of around 10 fs is required. Main sources of noise are vibrations in the range up to some 100 Hz, electronic noise of 50 Hz and harmonics thereof and noise on the master reference frequency. The precise frequency distribution and timing system of the linac plays an important role in obtaining the best resolution possible.
In this thesis, an approach is presented and experimentally realised which reaches a short-term stability of better than 40 fs to measure the longitudinal bunch structures of the bunches at the 100 MeV linac of the Swiss Light Source (SLS) of the Paul Scherrer Institute, Villingen, Switzerland. Measurements with the system show a stability of 37 fs which is close to the limit of an analogue controlled regulator in combination with the femtosecond laser system used. This is an improvement over the previous design at the Telsa Test Facility (TTF) linac in its phase 1 by a factor of 20.
The expected bunch length from coherent transition radiation (CTR) measure-

[4] **F**ree **E**lectron **L**aser for **I**nfrared E**x**periments

ments [Sue04] is around 3ps FWHM, so the stability is sufficient to obtain good results.
In the nearer future, an EOS setup will be commissioned at the TTF Phase 2 at DESY in Hamburg. Based on the work of this thesis, it appears to be feasible to design a system for TTF, which meets the requirements due to the expected bunch length of $50\,\mu$m. The synchronisation built for the measurements at the PSI is an approach to reach the stability required for the EOS experiment at TTF2 and on the longer run for an EOS experiment at the XFEL.

2. Theoretical background

The linear electro-optic effect (Pockels effect) is the basis of the electro optic sampling technique. The Pockels effect will be described in this chapter, along with the technique of electro-optic sampling. The treatment follows partly [YY84, Bru03]. Furthermore the properties of optical and coherent transition radiation and the principle of the generation of femtosecond laser pulses will be described.

2.1. Wave propagation in anisotropic crystals

In an isotropic medium, the polarisation $\boldsymbol{P}$ induced by a wave with the electric field vector $\boldsymbol{E}$ is always parallel to the electric field and related to the field by a scalar factor, the susceptibility. The situation changes however, if the medium becomes anisotropic. Then the induced polarisation is not necessarily parallel to the electric field, so the susceptibility is now a tensor. The relation between polarisation and electric field can be found as (see e.g. [Jac99]):

$$\boldsymbol{P} = \varepsilon_0 \chi_{ij} \boldsymbol{E} \tag{2.1}$$

The coefficients of the susceptibility tensor χ_{ij} depend on the choice of the coordinate system relative to the crystal lattice. It is always possible to find a system where χ_{ij} becomes a diagonal matrix with only 3 independent entries. This leaves:

$$P_1 = \varepsilon_0 \chi_{11} E_1 \tag{2.2}$$
$$P_2 = \varepsilon_0 \chi_{22} E_2 \tag{2.3}$$
$$P_3 = \varepsilon_0 \chi_{33} E_3 \tag{2.4}$$

If the χ_{ii} are not all equal, the material exhibits birefringence. The axes, whose choice makes the susceptibility tensor a diagonal matrix, are called the principal axes of the crystal. Introducing the dielectric permittivity tensor

$$\varepsilon_{ij} = \varepsilon_0 (1 + \chi_{ij}) \tag{2.5}$$

the relation

$$\boldsymbol{D} = \varepsilon_0 \boldsymbol{E} + \boldsymbol{P} \quad \text{respectively} \quad D_i = \sum_j \varepsilon_{ij} E_j \tag{2.6}$$

is found. The argumentation for the susceptibility tensor is also valid for the permittivity tensor. In an anisotropic crystal, the phase velocity

$$v_p = \frac{c}{\sqrt{\varepsilon}} = \frac{c}{n} \tag{2.7}$$

of a plane electromagnetic wave

$$\boldsymbol{E} = E_0 e^{i(\omega t - \boldsymbol{k}\boldsymbol{z})} \tag{2.8}$$

$$\text{with} \quad \boldsymbol{k} = \omega\sqrt{\varepsilon}\hat{\boldsymbol{k}}, \quad \left|\hat{\boldsymbol{k}}\right| = \frac{\boldsymbol{k}}{k}$$

depends on the direction of propagation and the direction of polarisation. Along a given direction of propagation $\boldsymbol{u}$, two independent eigenvectors $\boldsymbol{D}^s$ and $\boldsymbol{D}^f$ with different phase velocities and thus different refractive indices exist. The refractive indices of these two modes are commonly called n^s and n^f ("s" for slow and "f" for fast).

So in general, the polarisation state of a linearly polarised wave propagating through the crystal will not remain invariant. Only if the polarisation of the incident wave is parallel to one of the eigenvectors $\boldsymbol{D}^s$ or $\boldsymbol{D}^f$, its polarisation state will remain unchanged. For any other direction of polarisation, the field vector can be split into two components parallel to both eigenvectors of the crystal. As each propagates with a different phase velocity, a phase shift between both components and thus a change of polarisation of the exiting wave relative to its initial state is induced.

2.1.1. The index ellipsoid

In order to find the two indices of refraction it is convenient to define the so-called "index ellipsoid". The energy density of an electric field is given by:

$$w = \frac{1}{2}\boldsymbol{E} \cdot \boldsymbol{D} = \frac{1}{2} \cdot \sum_{i,j} E_i \varepsilon_{ij} E_j \tag{2.9}$$

If one transforms to the coordinate system where the dielectric tensor is diagonal, one can rewrite equation 2.9 into:

$$\frac{D_1^2}{\varepsilon_1} + \frac{D_2^2}{\varepsilon_2} + \frac{D_3^2}{\varepsilon_3} = 2w \tag{2.10}$$

By defining a dimensionless vector

$$\begin{pmatrix} u_1 \\ u_2 \\ u_3 \end{pmatrix} = \frac{\boldsymbol{D}}{\sqrt{2\varepsilon_0 w}} \tag{2.11}$$

and introducing the main refractive indices

$$n_i = \sqrt{\varepsilon_i}, \qquad i = 1, 2, 3 \tag{2.12}$$

equation 2.10 can be normalised. The result is

$$\frac{u_1^2}{n_1^2} + \frac{u_2^2}{n_2^2} + \frac{u_3^2}{n_3^2} = 1. \tag{2.13}$$

The main axes of the index ellipsoid have the length $2n_i$ and are parallel to the main axis of the crystal. If one defines the impermeability tensor by

$$\boldsymbol{\eta} = \boldsymbol{\varepsilon}^{-1} \tag{2.14}$$

whose entries in the base system of the crystal are

$$\begin{pmatrix} \frac{1}{n_1^2} & 0 & 0 \\ 0 & \frac{1}{n_2^2} & 0 \\ 0 & 0 & \frac{1}{n_3^2} \end{pmatrix} \tag{2.15}$$

the equation of the index ellipsoid can be rewritten as

$$\boldsymbol{u} \cdot \boldsymbol{\eta} \cdot \boldsymbol{u} = 1 \tag{2.16}$$

The two refractive indices can be found by the following means: A plane through the origin of the index ellipsoid perpendicular to the direction of the propagating light ray will create an intersecting ellipse (see figure 2.1). The two axes of this intersecting ellipse are equal in length to $2\,n_s$ and $2\,n_f$, where n_f and n_s are the two indices of refraction the material shows. These axes are parallel to the eigenvectors of the impermeability tensor.

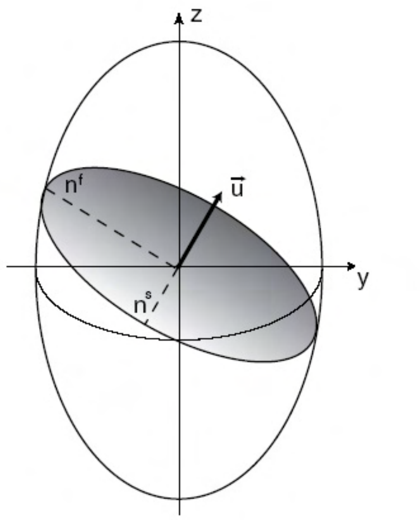

Figure 2.1.: Method of finding the two refractive indices. The shaded ellipse is the intersection of the index ellipsoid with the plane normal to the direction of incidence of the electromagnetic wave $\boldsymbol{u}$.

2.2. The Pockels effect

An external electric field changes the properties of an optically active crystal. The refractive index becomes a function of the external field which results in a change of the orientation of the index ellipse.

For high electric fields the polarisation becomes nonlinear in electric field strength and can be described by the following equation:

$$\boldsymbol{P} = \varepsilon_0(\boldsymbol{\chi}_e^{(0)}\boldsymbol{E} + \boldsymbol{\chi}_e^{(1)}\boldsymbol{E}^2 + \boldsymbol{\chi}_e^{(2)}\boldsymbol{E}^3 ...) \tag{2.17}$$

The linear susceptibility $\boldsymbol{\chi}_e^0$ induces the effects described in section 2.1. For weak electric fields, one can neglect all but the first term. The second order susceptibility $\boldsymbol{\chi}_e^1$ induces a dependency of the refractive index on the electric field (linear electro-optical effect or Pockels effect). $\boldsymbol{\chi}_e^2$ leads to a dependency of the refractive index on the intensity of the electric field (quadratic electro optical effect or Kerr effect).

As $\boldsymbol{\chi}$ and $\boldsymbol{\eta}$ are related by equations 2.5 and 2.14, the impermeability tensor also contains terms of higher order in the presence of a strong external electric field and can thus be expanded using a Taylor-expansion around $\boldsymbol{E}_{CTR} = 0$:

$$\eta_{i,j} = \eta_{ij}(0) + r_{ijk}E_k + s_{ijkl}E_kE_l + \ldots \tag{2.18}$$

Here, r_{ijk} are the Pockels coefficients and s_{ijkl} the Kerr coefficients. For ZnTe their order of magnitude is:

$$\begin{aligned} r_{ijk} &\approx 10^{-12}\frac{m}{V} \\ s_{ijkl} &\approx 10^{-21}\frac{m^2}{V^2} \end{aligned} \tag{2.19}$$

In our case, the Kerr effect can be neglected. The impermeability tensor thus becomes:

$$\boldsymbol{\eta}(\boldsymbol{E}) = \varepsilon^{-1}\boldsymbol{I} + \boldsymbol{r}\cdot\boldsymbol{E} \tag{2.20}$$

Inserting this into equation 2.13 yields:

$$\boldsymbol{u}\cdot\boldsymbol{\eta}(\boldsymbol{E})\cdot\boldsymbol{u} = \sum_{i,j=1,2,3}\left(\varepsilon^{-1}\delta_{i,j} + \sum_{k=1,2,3} r_{ijk}E_k\right)u_iu_j = 1 \tag{2.21}$$

As the tensor $\boldsymbol{\eta}$ is symmetric ($r_{ijk} = r_{jik}$), it is convention to simplify the tensor by introducing the following nomenclature:

$(ij) \to I$	
$(1,1) \to 1$	$r_{11k} \to r_{1k}$
$(2,2) \to 2$	$r_{22k} \to r_{2k}$
$(3,3) \to 3$	$r_{33k} \to r_{3k}$
$(2,3) \to 4$	$r_{23k} = r_{32k} \to r_{4k}$
$(1,3) \to 5$	$r_{13k} = r_{31k} \to r_{5k}$
$(1,2) \to 6$	$r_{12k} = r_{21k} \to r_{6k}$

(2.22)

The indices i, j are combined to form the new index I. In the end the indices are contracted according to table 2.22.

2.2.1. Electro-optic effect in ZnTe

The symmetry of a crystal influences the number of independent entries of the matrix $\{r_{ijk}\}$. Crystals of the zincblende structure (e.g. GaAs, CdTe, ZnS, ZnTe) are composed of two face-centred cubic lattices shifted by one quarter of the spatial diagonal and thus feature a high degree of symmetry. As a consequence, the matrix of Pockels coefficients has only one independent entry ($r_{41} = r_{52} = r_{63}$) and assumes the form:

$$r_{Ik} = \begin{pmatrix} 0 & 0 & 0 \\ 0 & 0 & 0 \\ 0 & 0 & 0 \\ r_{41} & 0 & 0 \\ 0 & r_{41} & 0 \\ 0 & 0 & r_{41} \end{pmatrix} \tag{2.23}$$

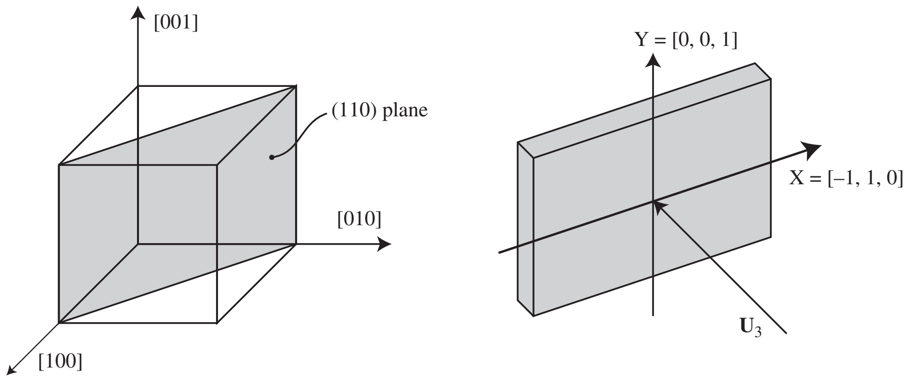

Figure 2.2.: Left: The (110)-plane in which the used crystals are cut. Right: the coordinate system (X,Y). Incident CTR-beam and laser pulse are parallel to the vector $\boldsymbol{U}_3$

.

As the ZnTe crystal is isotropic at vanishing electric fields, we have $n_1 = n_2 = n_3 = n_0$ and owing to the high degree of symmetry, equation 2.16 assumes the following form:

$$\frac{1}{n_0^2}(u_1^2 + u_2^2 + u_3^2) + 2r_{41}(E_1 u_2 u_3 + E_2 u_3 u_1 + E_3 u_1 u_2) = 1 \tag{2.24}$$

To obtain modified refractive indices, one now has to perform a principal axis transformation.

2.2.2. Determination of the main refractive indices

In the experiment, a crystal cut in the (110)-plane is used (see Figure 2.2). The CTR[1]-Pulse and the probe pulse are incident perpendicular to this plane, so their electric field vectors lie in the (110)-plane to achieve a maximum effect. We define a new coordinate system (X, Y) with

$$X = \frac{1}{\sqrt{2}} \begin{pmatrix} -1 \\ 1 \\ 0 \end{pmatrix} \quad \text{and} \quad Y = \begin{pmatrix} 0 \\ 0 \\ 1 \end{pmatrix} \tag{2.25}$$

Assuming perpendicular incidence to the XY-plane and an angle α of the electric field with aspect to the X-axis, the components of the electric vector $\boldsymbol{E_{CTR}}$ of the CTR in the base system of the crystal lattice are

$$\boldsymbol{E_{CTR}} = E_{CTR} \begin{pmatrix} -\frac{1}{\sqrt{2}} \cos \frac{\alpha}{2} \\ \frac{1}{\sqrt{2}} \cos \frac{\alpha}{2} \\ \sin \alpha \end{pmatrix} \tag{2.26}$$

[1]Coherent Transition Radiation

Inserting this into equation 2.20 yields

$$\boldsymbol{\eta}(\boldsymbol{E}_{CTR}) = \frac{1}{n_0^2}\begin{pmatrix} 1 & 0 & 0 \\ 0 & 1 & 0 \\ 0 & 0 & 1 \end{pmatrix} + r_{41}E_{CTR}\begin{pmatrix} 0 & \sin\alpha & \cos\alpha/\sqrt{2} \\ \sin\alpha & 0 & -\cos\alpha/\sqrt{2} \\ \cos\alpha/\sqrt{2} & -\cos\alpha/\sqrt{2} & 0 \end{pmatrix} \tag{2.27}$$

To find the main refractive indices and the principal axis, the eigenvalues and eingenvectors of the tensor $\boldsymbol{\eta}$ have to be calculated. The eigenvalues can be evaluated to

$$\lambda_{1,2} = \frac{1}{n_0^2} - \frac{r_{41}E_{CTR}}{2}\left(\sin\alpha \pm \sqrt{1+3\cos^2\alpha}\right) \quad , \quad \lambda_3 = \frac{1}{n_0^2} + r_{41}E_{CTR}\sin\alpha \tag{2.28}$$

The normalised eigenvectors are:

$$\begin{aligned} \boldsymbol{U}_1 &= \tfrac{1}{2}\sqrt{1+\tfrac{\sin\alpha}{\sqrt{1+3\cos^2\alpha}}}\begin{pmatrix} -1 \\ 1 \\ \frac{2\sqrt{2}\cos\alpha}{\sqrt{1+3\cos^2\alpha}+\sin\alpha} \end{pmatrix} \\ \boldsymbol{U}_2 &= \tfrac{1}{2}\sqrt{1+\tfrac{\sin\alpha}{\sqrt{1+3\cos^2\alpha}}}\begin{pmatrix} 1 \\ -1 \\ \frac{2\sqrt{2}\cos\alpha}{\sqrt{1+3\cos^2\alpha}-\sin\alpha} \end{pmatrix} \\ \boldsymbol{U}_3 &= \tfrac{1}{\sqrt{2}}\begin{pmatrix} -1 \\ -1 \\ 0 \end{pmatrix} \end{aligned} \tag{2.29}$$

The main refractive indices are given by

$$n_i = \frac{1}{\sqrt{\lambda_i}}. \tag{2.30}$$

Taking into account that $r_{41}E_{CTR} \ll 1/n_0^2$ the result for the main refractive indices is:

$$\begin{aligned} n_1 &= n_0 + \tfrac{n_0^3 r_{41}E_{CTR}}{4}\left(\sin\alpha + \sqrt{1+3\cos^2\alpha}\right) \\ n_2 &= n_0 + \tfrac{n_0^3 r_{41}E_{CTR}}{4}\left(\sin\alpha - \sqrt{1+3\cos^2\alpha}\right) \\ n_3 &= n_0 - \tfrac{n_0^3 r_{41}E_{CTR}}{2}\sin\alpha \end{aligned} \tag{2.31}$$

Looking at the normalised eigenvectors it becomes obvious that the third principal axis is perpendicular to the (110) crystal plane. This is also the direction of incidence of the CTR radiation. The vectors $\boldsymbol{U}_1$ and $\boldsymbol{U}_2$ are of course perpendicular to each other but may enclose an angle ψ with the X-axis (the [-1,1,0] axis). This angle can be evaluated by using the scalar product of $\boldsymbol{U}_1$ and $\boldsymbol{X}$ and applying the relation $\cos(2\psi) = 2\cos^2\psi - 1$. This yields

$$\cos 2\psi = \frac{\sin\alpha}{\sqrt{1+3\cos^2\alpha}}. \tag{2.32}$$

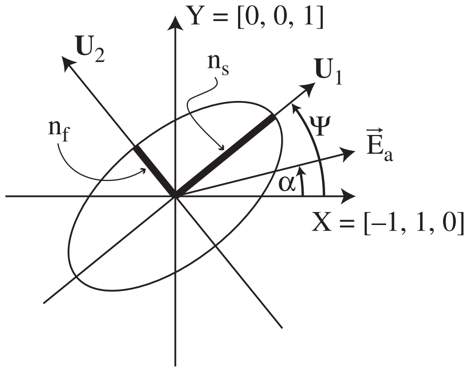

Figure 2.3.: The refractive index ellipsoid projected onto the (110) plane of the ZnTe crystal. The electric field vector $\boldsymbol{E}_{CTR}$ encloses an angle α with the X=[-1,1,0] axis of the crystal while the angle between the long half axis of the ellipse and the X axis is given by $\psi(\alpha)$. Both the CTR and laser pulse impinge along the normal to the (110) plane, given by the unit vector $\boldsymbol{U}_3 = (-1/\sqrt{2}, -1/\sqrt{2}, 0)$.

Care has to be taken in the evaluation of the vector $\boldsymbol{U}_2$ at the limit of $\alpha \to \pi/2$ as the normalisation factor vanishes and the third component tends to infinity. The result is

$$\boldsymbol{U}_2\left(\frac{\pi}{2}\right) = \begin{pmatrix} 0 \\ 0 \\ 1 \end{pmatrix}. \tag{2.33}$$

So for $\alpha = \pi/2$, the vectors $\boldsymbol{U}_1, \boldsymbol{U}_2$ point in the directions of X and Y respectively.

The principal indices of refraction corresponding to the first two principal axes are n_1 and n_2. The according refractive index ellipse is shown in figure 2.3.

The TiSa laser beam of angular frequency ω is incident on the ZnTe crystal along the eigenvector $\boldsymbol{U}_3$, so its electric vector $\boldsymbol{E}_{probe}$ lies in the (110) plane. In a crystal of the thickness d, the two components of $\boldsymbol{E}_{probe}$ along the principal axes $\boldsymbol{U}_1$ and $\boldsymbol{U}_2$ recieve a relative phase shift of

$$\Gamma(\alpha) = \frac{\omega d}{c}(n_1 - n_2) = \frac{\omega d}{2c} n_0^3 r_{41} E_{CTR} \sqrt{1 + 3\cos^2\alpha}. \tag{2.34}$$

This equation will be used in the following to evaluate the measurements. The phase shift is only sensitive to the electric field strength of the external electric field E_{CTR} and to the angle between field and X-axis.

2.3. Spectroscopy using electro-optical sampling

The principle of the electro-optical sampling relies on the measurement of the change of the refractive index due to the Pockels effect when the crystal is hit by an electromagnetic pulse. One possibility of detecting this change is by converting it into an intensity modulation of an ultrashort optical probe pulse passing through the crystal.

2.3.1. Corrections of the phase shift

The linearly polarised coherent transition radiation (CTR) used in our case to induce the Pockels effect is incident perpendicular to the (110) plane and has frequency components up to a few hundred GHz, depending on the bunch length. The electric field vector of the CTR radiation E_{CTR} has an angle α with the [-1,1,0] axis. If now a linear polarised optical probe pulse E_{probe} hits the crystal, the different refractive indices n_s and n_f (see equation 2.34) lead to a phase shift between the two components of the electric field of the probe pulse.

The relative phase shift between the two components is given by:

$$\Delta\Phi_{probe} = \left|\Delta n \frac{\omega}{c} d\right| = \left|\frac{n_0^3 r_{41} E_{CTR}\sqrt{1+3\cos^2\alpha}}{2}\frac{\omega d}{c}\right|, \tag{2.35}$$

where d is the thickness of the ZnTe crystal and ω the optical frequency of the probe pulse. The phase shift assumes a maximum for $\alpha = 0$, when the field vector of the CTR radiation is parallel to the X-axis (see section 2.2.2):

$$\Delta\Phi_{max} = \left|\frac{n_0^3 r_{41} E_{CTR}\omega}{c} d\right| \tag{2.36}$$

The phase difference depends on the polarisation direction of the probe laser pulse relative to the index ellipse. This can be easily understood by assuming a laser pulse polarised parallel to one of the main axes of the index ellipsoid. In this case, the state of polarisation remains unchanged. Thus there is no measurable signal on a detector. A detailed analysis of the dependencies of the measured signal with respect to the orientation of the fields E_{probe} and E_{CTR} taking our specific setup into account can be found in section 5.4. The orientation leading to the largest possible effect is shown in figure 2.4.

As the frequencies of the CTR-pulse and the probe pulse are significantly different, transmission effects in the crystal, absorption and reflexion effects have to be taken into account leading to corrections of equation 2.36. For a detailed description of the corrections applied see [Bak98].

1. frequency dependent refractive indices and absorption coefficients κ in the electro-optical crystal lead to a frequency dependent reflexion on the crystal surfaces:

$$\frac{I_{ref}}{I_o} = \frac{[n(\omega)-1]^2 + \kappa(\omega)^2}{[n(\omega)+1]^2 + \kappa(\omega)^2} \tag{2.37}$$

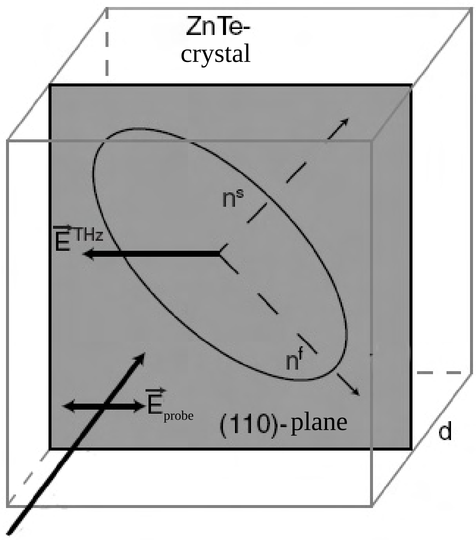

Figure 2.4.: Geometry leading to the largest electro-optical effect. The probe pulse is incident perpendicular to the (110) plane, has an angle α with the X-axis and is linearly polarised parallel to the [-110] axis, as is the CTR field.

It has to be taken into account that the optical as well as the CTR pulses may be reflected numerous times at the crystal surfaces, which gives an effect similar to a Fabry-Perot-Interferometer, leading to a modified measured phase shift which may be larger or smaller than the real phase shift.

2. The optical probe pulse is a 15 fs long pulse with a central wavelength of $\lambda_{probe} = 800\,\text{nm}$ and a spectral bandwidth of $\Delta\lambda_{probe} = 65\,\text{nm}$. Due to its high bandwidth, the probe pulse experiences dispersion in the crystal and sees a group refractive index of

$$n_g = n - \lambda_0 \frac{dn}{d\lambda_0} \tag{2.38}$$

and thus a group velocity of

$$v_g = \frac{c}{n_g}. \tag{2.39}$$

Furthermore, the probe pulse and the CTR pulse travel with different group velocities through the crystal. The refractive index of ZnTe for optical radiation is $n_{opt} = 2.85$ and for radiation with a frequency of 1 THz $n_{THz} = 3.05$ As the probe pulse is faster than the CTR pulse, the probe pulse will average over some oscillations of the CTR field. Thus the measured signal is diminished depending on the crystal thickness d. As the probe pulse is significantly shorter than the CTR pulse, it can be reasonably well described by a delta function

$$E_{probe} = E_0 \cdot \delta(\frac{x}{v_g} + t - \tau), \tag{2.40}$$

where τ is the delay between probe pulse and CTR pulse. The phase difference can be reconstructed from the measured signal using the following equation:

$$\Delta\Phi_{max} = \frac{\omega}{c} n_o^3 r_{41} \int_0^d dx \int_{-\infty}^{+\infty} dt E_{CTR}(x,t) \delta(\frac{x}{v_g} + t - \tau) \tag{2.41}$$

2.3.2. Electro-optic sampling

The length of the CTR pulse emitted by the electron bunch is significantly larger than the probe pulse. It is hence possible to image the form of the CTR pulse by sampling many closely spaced probe pulses. The principle of this scheme can be seen from figure 2.5.

The CTR pulse and probe pulse are brought to spatial and temporal overlap on the crystal and the detector signal at the time $t = 0$ is measured. The arrival time of the probe pulse can be delayed by a known time $t = \tau$. This measurement scheme allows a sampling of the CTR pulse with a resolution limited only by the accuracy of the synchronisation between laser repetition rate and master RF and the probe pulse duration. As this method samples many bunches, it can only deliver an accurate bunch shape if the shape variations from bunch to bunch are negligible.

2.3.3. Principle of signal detection

The TiSa laser beam with electric vector $\boldsymbol{E}_{probe}$ impinges along the normal to the XY-plane (see section 2.2.2) coinciding with the principal axis $\boldsymbol{U}_3$. The propagation of a polarised light ray can be described very elegantly using the Jones calculus, see e.g. [YY84]. Laser light with a horizontal or vertical polarisation is represented by the vectors

$$\boldsymbol{E}_h = E_b \begin{pmatrix} 1 \\ 0 \end{pmatrix}, \quad \text{or} \quad \boldsymbol{E}_v = E_b \begin{pmatrix} 0 \\ 1 \end{pmatrix} \tag{2.42}$$

The rotation of the polarisation plane can be described by the matrix

$$\boldsymbol{R}(\phi) = \begin{pmatrix} \cos\phi & \sin\phi \\ -\sin\phi & \cos\phi \end{pmatrix}. \tag{2.43}$$

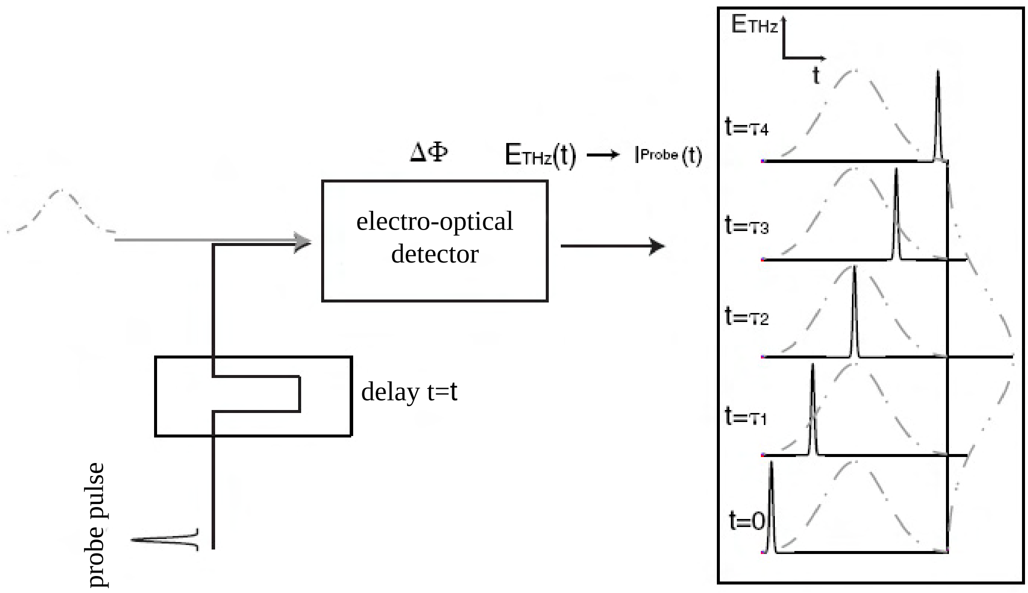

Figure 2.5.: Principle of electro-optic sampling

The matrix of a quarter wave plate is:

$$\boldsymbol{Q} = \begin{pmatrix} \exp(-i\pi/4) & 0 \\ -0 & \exp(+i\pi/4) \end{pmatrix}. \tag{2.44}$$

To describe the birefringent ZnTe crystal with the indices $n_s = n_1(\alpha), n_f = n_2(\alpha)$ and thickness d in the principal axis coordinate system the following matrix can be used:

$$\boldsymbol{ZT} = \begin{pmatrix} \exp(-in_s\omega d/c) & 0 \\ 0 & \exp(-in_f\omega d/c) \end{pmatrix} \tag{2.45}$$

One can rewrite this matrix by separating out the average phase change $\phi = (n_s + n_f)\omega d/c$:

$$\boldsymbol{ZT} = \begin{pmatrix} \exp(-i\Gamma(\alpha)/2 & 0 \\ 0 & \exp(-i\Gamma(\alpha)/2 \end{pmatrix} \cdot e^{-i\phi} \tag{2.46}$$

Here, $\Gamma(\alpha)$ is given by equation 2.34. As we are calculating intensities, the overall phase factor $\exp(-i\phi)$ can be omitted in the following. Using the unity matrix $\boldsymbol{I}$ and the matrix

$$\boldsymbol{J} = \begin{pmatrix} -i & 0 \\ 0 & i \end{pmatrix} \tag{2.47}$$

with the convenient property $\boldsymbol{J}^2 = -\boldsymbol{I}$, one can write 2.46 into

$$\boldsymbol{ZT}(\alpha) = \boldsymbol{I} \cdot \cos\frac{\Gamma(\alpha)}{2} + \boldsymbol{J}\sin\frac{\Gamma(\alpha)}{2}. \tag{2.48}$$

Two often used detection schemes will be discussed: crossed polarisers and a balanced diode detector. Assume a horizontally polarised laser beam. Its electric field vector can be expressed by

$$\boldsymbol{E}_{probe} = E_{probe}\begin{pmatrix} 1 \\ 0 \end{pmatrix} \tag{2.49}$$

The effect of a ZnTe crystal can be calculated by rotating the electric field vector into the base system of the crystal, applying the phase retardation of the ZnTe crystal and rotating the electric field vector back into the original (XY) coordinate system:

$$E_{probe} \cdot \boldsymbol{R}(-\psi) \cdot \boldsymbol{ZT}(\alpha) \cdot \boldsymbol{R}(\psi) \cdot \begin{pmatrix} 1 \\ 0 \end{pmatrix} \tag{2.50}$$

The angle ψ is the angle between the main axis of the index ellipsoid and the X-axis (see figure 2.3). The signal is detected by a photomultiplier behind a polariser rotated by 90°, so equation 2.46 has to be multiplied from the left by the vector (0, 1). The electric field at the photomultiplier is thus given by:

$$E_{probe} \cdot \begin{pmatrix} 0 & 1 \end{pmatrix} \boldsymbol{R}(-\psi) \cdot \boldsymbol{ZT}(\alpha) \cdot \boldsymbol{R}(\psi) \cdot \begin{pmatrix} 1 \\ 0 \end{pmatrix} \tag{2.51}$$

Inserting equation 2.46 yields for the intensity S at the detector:

$$S(\alpha) = E_{probe}^2 \sin^2(2\psi(\alpha)) \sin^2\left(\frac{\Gamma(\alpha)}{2}\right) \tag{2.52}$$

The alternative system uses a quarter-wave plate, a Wollaston prism and a balanced diode detector. We now show that it offers a much better sensitivity than the crossed polariser setup. Behind the ZnTe crystal, the light passes through a quarter-wave plate whose optical axis is oriented 45° with respect to the polarisation direction of the laser beam. That means one has to rotate the beam into the main coordinate system of the quarter-wave plate, apply the appropriate matrix and rotate it back. This yields a transfer function together with equation 2.51 of:

$$T = E_{probe} \cdot \boldsymbol{R}(-\pi/4) \cdot \boldsymbol{Q} \cdot \boldsymbol{R}(\pi/4)\boldsymbol{R}(-\psi) \cdot \boldsymbol{ZT}(\alpha) \cdot \boldsymbol{R}(\psi) \cdot \begin{pmatrix} 1 \\ 0 \end{pmatrix} \tag{2.53}$$

The Wollaston prism splits the beam into two orthogonal polarisation components, which are guided to the diodes of the balanced detector. The scheme is sketched in figure 5.11.

Assuming an angle $\alpha = 0 \rightarrow \psi = \pi/4$, which is equivalent to a maximum signal on the detector (see section 5.4.2), one inserts equation 2.53:

$$\begin{aligned} T &= E_{probe} \cdot \boldsymbol{R}(-\pi/4) \cdot \boldsymbol{Q} \cdot \boldsymbol{R}(\pi/4)\boldsymbol{R}(\pi/4) \cdot \\ & \left(\boldsymbol{I} \cdot \cos \frac{\Gamma(\alpha)}{2} + \boldsymbol{J} \sin \frac{\Gamma(\alpha)}{2} \right) \cdot \boldsymbol{R}(\pi/4) \cdot \begin{pmatrix} 1 \\ 0 \end{pmatrix} \end{aligned} \tag{2.54}$$

This can be rewritten by introducing $\widehat{I}$ and $\widehat{J}$ with

$$\begin{aligned} \widehat{I} &= \boldsymbol{R}(-\pi/4) \cdot \boldsymbol{Q} \cdot \boldsymbol{R}(\pi/4) \cdot \boldsymbol{R}(-\pi/4) \cdot \boldsymbol{I} \cdot \boldsymbol{R}(\pi/4) = \frac{1}{\sqrt{2}} \begin{pmatrix} 1 & -i \\ -i & 1 \end{pmatrix} \\ \widehat{J} &= \boldsymbol{R}(-\pi/4) \cdot \boldsymbol{Q} \cdot \boldsymbol{R}(\pi/4) \cdot \boldsymbol{R}(-\pi/4) \cdot \boldsymbol{J} \cdot \boldsymbol{R}(\pi/4) = -\frac{1}{\sqrt{2}} \begin{pmatrix} 1 & i \\ i & 1 \end{pmatrix}. \end{aligned}$$

If now the optical axis of the Wollaston prism is orientated such that one of the orthogonal polarisation components is parallel to the incoming polarisation direction of the beam, the laser amplitude seen on the detector diodes is:

$$\begin{aligned} A_1 &= E_{probe} \cdot \begin{pmatrix} 0 & 1 \end{pmatrix} \cdot \left(\widehat{I} \cos \Gamma/2 + \widehat{J} \sin \Gamma/2 \right) \cdot \begin{pmatrix} 1 \\ 0 \end{pmatrix} \\ &= E_{probe} \cdot \frac{1}{\sqrt{2}} \cdot (\cos(\Gamma/2) - \sin(\Gamma/2)) \\ A_2 &= E_{probe} \cdot \begin{pmatrix} 0 & 1 \end{pmatrix} \cdot \left(\widehat{I} \cos \Gamma/2 + \widehat{J} \sin \Gamma/2 \right) \cdot \begin{pmatrix} 1 \\ 0 \end{pmatrix} \\ &= -E_{probe} \cdot \frac{i}{\sqrt{2}} \cdot (\cos(\Gamma/2) - \sin(\Gamma/2)) \end{aligned} \tag{2.55}$$

The intensity difference seen by the balanced detector is:

$$|A_1|^2 - |A_2|^2 = E^2_{probe} \sin \Gamma \tag{2.56}$$

For reasonable THz fields of up to $10^{10}\,\frac{V}{m}$, the quantity Γ is $\ll 1$. Then the balanced detector signal is linear in the electric field E_{CTR} of the CTR pulse and therefore much larger than the signal of the crossed-polariser setup which is proportional to Γ^2.

Figure 2.6 shows the expected signal strengths for the set of parameters expected at the PSI, namely an electric field at the crystal of $E_{CTR} = 10^5\,\frac{\mathrm{kV}}{\mathrm{cm}}$, a crystal thickness of 1 mm, and an optical probe pulse wavelength of 800 nm.

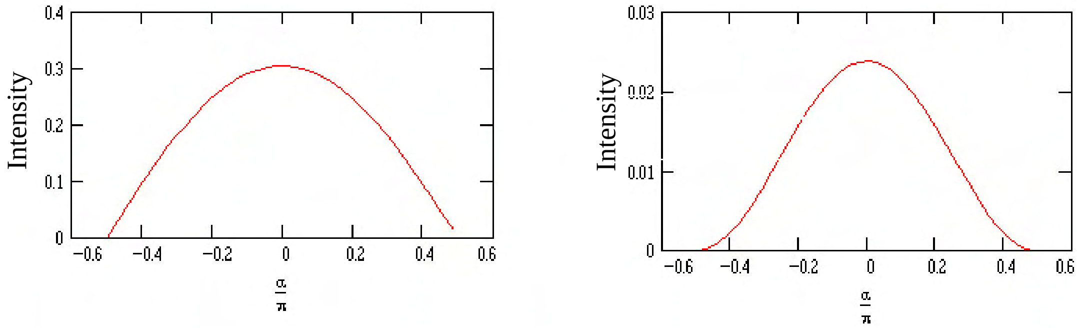

Figure 2.6.: Expected signal from the two detection schemes. Left: using a balanced diode detector; Right: using the crossed polariser scheme

3. The laser system

The temporal resolution of the electro-optic sampling depends on the length of the laser pulses. Commercially available Titanium-Sapphire (TiSa) laser systems can reach a pulse length of $< 15\,\mathrm{fs}$. In this experiment a Femtosource 20 from Femtolasers Vienna, Austria was used. The laser is a passively mode-locked TiSa oscillator, pumped by a 5 W frequency doubled $Nd:YVO_4$-Laser from Coherent Radiation Inc. In this chapter, some background of the TiSa oscillator will be given.

3.1. The TiSa oscillator

An electromagnetic pulse travelling in a resonator can be described by a superposition of plane waves with different wavelengths. The achievable laser pulse duration depends on the number of available longitudinal modes, which is limited by the bandwidth of the emission band. A suitable material for femtosecond pulses is Ti:Al_2O_3. A small percentage of the Al^{3+} Ions is replaced by Ti^{3+}-Ions. Such a doped sapphire crystal shows a fluorescence band in the regime from 670 nm to 1070 nm. A good pumping efficiency is due to an absorption band at around 500 nm.

3.1.1. Superposition of longitudinal modes

The possible wavelengths of the longitudinal modes in a resonator are given by the condition

$$n \cdot \lambda_n = 2 \cdot L, \tag{3.1}$$

where λ_n is the wavelength of the longitudinal mode and L the resonator length. In principal, a large number of modes of different frequency can exist at the same time. These modes will be independent in phase and amplitude. Thus the total electric field in the resonator is given by the sum of the field of all excited modes:

$$E(z,t) = \sum_n E_n(z,t) = \sum_n |E_{0,n}|\, e^{i\phi_n} e^{ik_n z - i\omega_n t}, \tag{3.2}$$

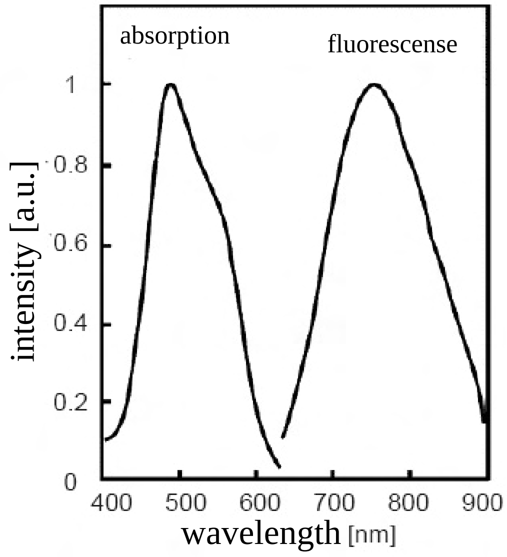

Figure 3.1.: Absorption and emission spectrum of titanium-sapphire

where $E_{0,n}$ is the complex amplitude of the n-th mode and ϕ_n its phase. Calculation of the intensity, assuming an equal amplitude for all modes yields

$$I(z,t) \propto E(z,t)E^*(z,t) = |E_0|^2 \sum_{n=1}^{N} \sum_{m=1}^{N} e^{i(\phi_n - \phi_m)} e^{i\Omega(\frac{z}{c}-t)}. \tag{3.3}$$

with

$$\Omega = \omega_{n+1} - \omega_n = \frac{\pi c}{L} \tag{3.4}$$

being the frequency difference between two neighbouring modes. If all modes have a fixed phase relation, equation 3.3 yields:

$$I(z,t) \propto |E_0|^2 e^{i\delta\phi} \sum_{n=1}^{N} \sum_{m=1}^{N} e^{i\Omega(\frac{z}{c}-t)}. \tag{3.5}$$

The second exponential function in equation 3.5 becomes equal to 1 for all terms of the sum if the condition

$$\frac{\omega}{c}(z - ct) = 2\pi \cdot j \quad \Leftrightarrow \quad z - ct = 2L \cdot j, \quad j = 0, 1, 2, ... \tag{3.6}$$

is fulfilled. The maximum of equation 3.5 under this condition is

$$I_{max} = N^2 |E_0|^2 \equiv N^2 I_0 \tag{3.7}$$

One can derive the spatial and temporal distances of consecutive pulses as a function of the intensity I_{max} from equation 3.6, which yields:

$$\Delta z = 2L, \quad \Delta t = \frac{2L}{c} \equiv T \tag{3.8}$$

That means the intensity maxima repeat with the revolution time T of the laser cavity and there is one maximum inside the resonator at any given time. Through a fixed phase relation between the many modes in the resonator, regular pulses with a peak intensity I_{max} will develop, proportional to the square of the number of involved modes (see figure 3.2). To calculate the FWHM of the pulses (see [HP98]), one can assume that at a fixed time $t = 0$ the superposition of N modes is similar to the interference of N planar waves. The interference pattern for a grid with a grid constant g is given through

$$I(z) = I_0 \frac{\sin(\frac{1}{2}Nk_z z)^2}{\sin(\frac{1}{2}k_z z)^2}, \quad k_z = k\frac{g}{D}, \tag{3.9}$$

where D is the distance between grid and screen and k the wave number of the interfering radiation. To transform this equation to the case of N superimposed modes, one has to substitute the wave number k_z by the wave number difference Δk of the modes. Besides the interference pattern for a fixed time, one can also use this relation for a fixed position, e.g. $z = 0$:

$$I(t) = I_0 \frac{\sin(\frac{N\Omega}{2}t)^2}{\sin(\frac{\Omega}{2}t)^2}, \quad \Omega = \frac{\pi c}{L} \tag{3.10}$$

Using equation 3.10, one can derive the FWHM of the pulses:

$$I(\Delta T) = \frac{1}{2}I_{max} \quad \rightarrow \quad \Delta T = \frac{1}{N}\frac{2L}{c} = \frac{1}{N}T \tag{3.11}$$

So the pulse width decreases with the number of superposed modes and is proportional to the revolution time of the laser cavity. For the laser used in the EOS experiment, the revolution frequency is 81 MHz, so the number of required pulses to achieve a pulse length of 12 fs is around 10^5. This in turn means that the chosen laser medium has to have a sufficiently broad emission band with many allowed states to support the number of required modes.

3.1.2. Achieving mode-lock

A rigid phase relation between superposing modes can be achieved by a modulation of the gain of the resonator (or the losses respectively) with the difference frequency Ω of adjecent modes. All mechanisms to achieve a mode-lock rely on that principle. Through the loss modulation, the electromagnetic field in the resonator acquires an additional time dependence:

$$\begin{aligned} E_n(z,t) &= (E_{0,n} + E_n^{mod}\cos\Omega t)e^{ik_n z - \omega_n t} \qquad (3.12) \\ &= \left[E_{0,n}e^{-i\omega_n t} + \frac{1}{2}E_n^{mod}\left(e^{-i\Omega t} + e^{i\Omega t}\right)e^{-i\omega_n t}\right]e^{ik_n z} \\ &= \left[E_{0,n}e^{-i\omega_n t} + \frac{1}{2}E_n^{mod}\left(e^{-i\omega_{n+1} t} + e^{-i\omega_{n-1} t}\right)\right]e^{ik_n z} \end{aligned}$$

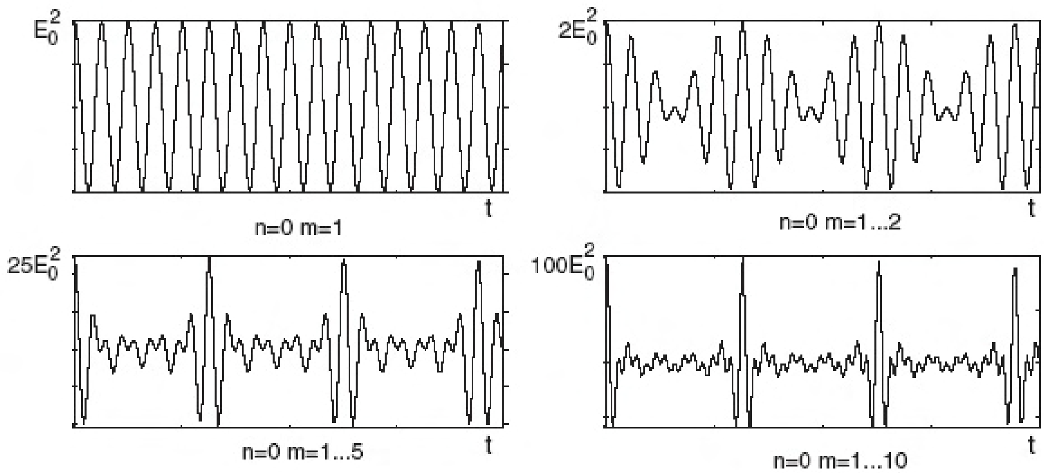

Figure 3.2.: Superposition of different number of longitudinal modes with a fixed phase difference. The intensity of these pulses scales quadratically with the number of involved modes.

Equation 3.12 shows that the time dependence induces sidebands in every mode whose frequencies coincides with the one of a neighbouring mode. As this principle is valid for the total bandwidth, a phase synchronisation between all longitudinal modes is reached. There are various possibilities to achieve this time dependence of the electromagnetic field. All active mode locking devices are limited in their speed of operation (fast pockels cells can switch in 10^{-9}s). To achieve ultrashort pulses, passive mode locking is used which is described in the following section.

Loss modulation through the Kerr lens

The Kerr effect describes the dependency of refractive index on the intensity of the incident beam (see equation 2.17). Assuming a Gaussian beam the variation of the refractive index can be written as [Rul98]

$$n(\boldsymbol{r}) = n_0 + \frac{1}{2} n_2 I(\boldsymbol{r}), \quad \text{with} \quad I(\boldsymbol{r}) = e^{-\frac{r^2}{2\sigma^2}}. \tag{3.13}$$

If n_2 is positive, the refractive index of a $\chi^{(2)}$ medium is larger at the axis of the beam than perpendicular to it. The relevant parameter for the propagation of a light ray is the optical path length, the product of the index of refraction n and the propagation distance d, $P(\boldsymbol{r}) = n(\boldsymbol{r}) \cdot d$. The lensing effect of the modulation of the refractive index can be seen by replacing the constant thickness d by a variable one, so the product with a constant refractive index leads to the same optical path length:

$$P(\boldsymbol{r}) = n(r)d = d(\boldsymbol{r})n_0. \tag{3.14}$$

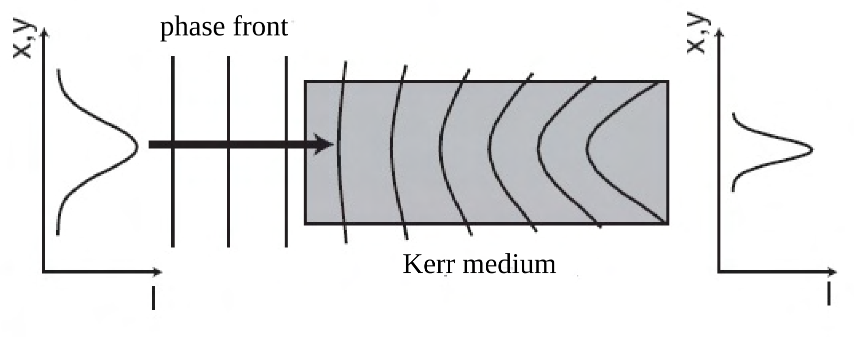

Figure 3.3.: Principle of the Kerr medium leading to a focusing of the laser beam

Then

$$d(\boldsymbol{r}) = \frac{d \cdot n(\boldsymbol{r})}{n_0} \tag{3.15}$$

and one obtains a Gaussian lens, focusing the optical beam. This effect is enhanced while the light beam propagates through a thick material, because focusing of the beam increases the focal power of the lens. The linear diffraction in the $\chi^{(2)}$ medium will at some stage create an equilibrium state, balancing the Kerr effect. This is called self-focusing and is of principal importance to the creation of ultrashort pulses, as the now commonly used TiSa-crystal shows this effect (see figure 3.3).

3.2. Building the oscillator

Figure 3.4 shows the principal setup of a titanium sapphire laser system. It is pumped by a frequency doubled $Nd:YLF$ Laser with a wavelength of 532 nm.

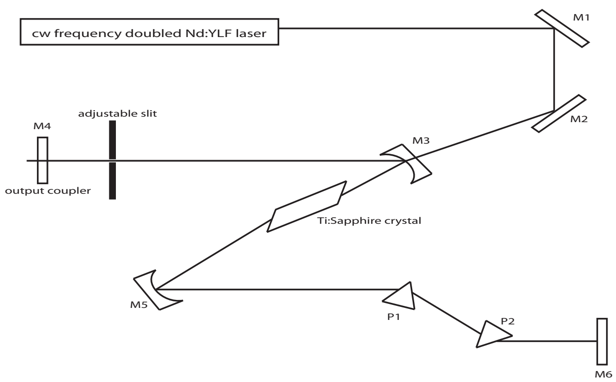

Figure 3.4.: Simplified setup of a TiSa laser system

The dicroic mirror M3 is transparent to the pumping wavelength, but reflects the emission wavelengths of TiSapphire. The two prisms P1 and P2 compensate the dispersion inside the cavity. As explained above, the refractive index inside the TiSa crystal is not constant for all parts of a Gaussian wave and thus it is focused. The self-focusing is much larger for strong intensity maxima, but the effect is negligible for weaker fields [Rul98]. As the transverse structures of strong intensity maxima have been reduced in size, they are less subject to losses while propagating through the cavity. A well adjusted pinhole aperture helps the self-focusing process.

The laser will not mode-lock automatically, as normally no sufficiently strong intensity fluctuations will arise to create a relevant Kerr effect, so cw operation is energetically favoured over mode locking. But one can create an intensity pulse by jolting quickly one of the mirrors. This then triggers off the process.

The reason why the pules become short and are stabilized can be seen by taking into account the influence of the self-focusing on the time structure of the pulse. The change of the refractive index according to equation 3.13 is also responsible for a rapid change of phase of the wave as a function of time, as the intensity $I(t)$ also varies rapidly with time. The self-modulation of the phase broadens the spectrum of the pulse and thus shortens its duration. Again an equilibrium is reached, when the dispersion compensates the self-modulation of the phase. To be able to control the group velocity inside the cavity, the prisms P1 and P2 are used. In the end one pulse will travel back and forth in the cavity while keeping its structure.

The oscillator is strongly temperature dependent, as mechanical changes due to a temperature drift affect the cavity length and thus the revolution frequency. Therefore, the laser is mounted on a temperature stabilized chiller plate.

The output laser pulse of a laser based on the Kerr lens to compress the bunch is not yet Fourier-limited, meaning that the pulse is not the shortest possible for the given bandwidth. Another effect of the linear dispersion in the Kerr medium is a positive chirp of the pulse. That means that low frequencies are at the head of the pulse and high ones at the tail. The bunch can be further shortened by using so called chirped mirrors (see figure 3.5), consisting of dielectric layers. Higher frequencies are reflected at the front layers and lower frequencies at inner layers. This leads to different path lengths for different frequencies and, if used correctly, these mirrors can compress the bunch to the shortest length permitted by the Fourier theorem.

In order to regulate the repetition rate, one mirror of the cavity is movable with a picomotor and a piezo crystal. Coarse adjustments can be made with the

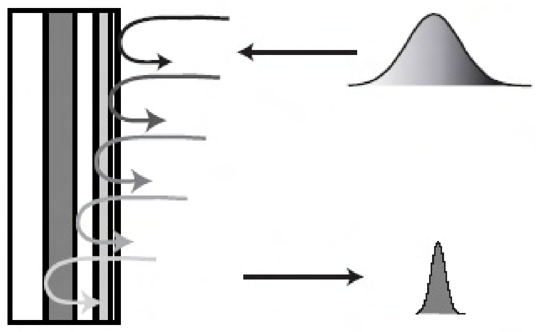

Figure 3.5.: Principle of chirped mirrors

picomotor, regulation at the femtosecond level can be achieved by using the piezo actuator.

4. Transition radiation

At the transition of one material to another with different dielectric properties, a charged particle emits electromagnetic radiation due to the boundary conditions. In the case of highly relativistic electron bunches, information about the charge distribution can be derived from this so-called transition radiation. In this chapter, the main properties of the transition radiation and its applications for the study of the longitudinal charge distribution will be summarized. For a detailed description, see e.g. [Gei99].

4.1. Optical transition radiation

The electric field of highly relativistic electrons is not spherically symmetric anymore, but is Lorentz contracted in a small disc perpendicular to the trajectory of the particle (see figure 4.1). Consider a charge q moving with a constant velocity $\boldsymbol{v}$ in the z-direction. Let the rest system of the electron be Σ' with coordinates x' and y' and the laboratory system Σ with coordinates x and y. The scalar and vector potential

$$\Phi\prime = \frac{-e}{4\pi\varepsilon_o r'}; \quad \boldsymbol{A} = 0 \tag{4.1}$$

in the rest system of the particle are converted into the laboratory system by a Lorentz transformation which yields as a function of the laboratory coordinates:

$$\Phi = \frac{-e}{4\pi\varepsilon_0} \cdot \gamma \cdot \frac{1}{\sqrt{\gamma^2(z-vt)^2 + y^2 + x^2}} \quad \text{and} \quad \boldsymbol{A} = \frac{\boldsymbol{v}}{c^2}\Phi \tag{4.2}$$

The electric field is now:

$$\begin{aligned} E_z &= -\frac{\partial \Phi}{\partial z} - \frac{\partial A_x}{\partial t} = \frac{-e}{4\pi\varepsilon_0} \cdot \gamma \cdot \frac{x - vt}{(\gamma^2(z-vt)^2 + y^2 + x^2)^{3/2}} \\ E_y &= -\frac{\partial \Phi}{\partial y} = \frac{-e}{4\pi\varepsilon_0} \cdot \gamma \cdot \frac{y}{(\gamma^2(z-vt)^2 + y^2 + x^2)^{3/2}} \\ E_x &= -\frac{\partial \Phi}{\partial x} = \frac{-e}{4\pi\varepsilon_0} \cdot \gamma \cdot \frac{z}{(\gamma^2(z-vt)^2 + y^2 + x^2)^{3/2}}, \end{aligned} \tag{4.3}$$

It is convenient to transform the field into cylindrical coordinates with $x = r\cos\phi$ and $y = r\cos\phi$ and z being the direction of propagation:

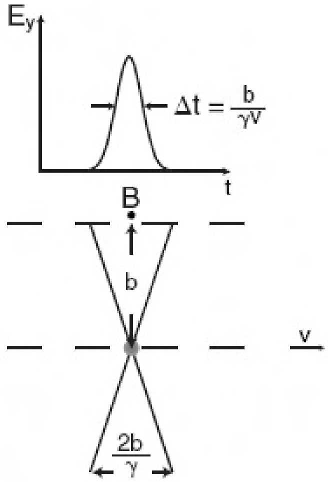

Figure 4.1.: Electric field of a relativistic charged particle. An observer at point B sees the electric field E(t) at a time t. The opening angle is $2/\gamma$.

$$E_z = \frac{-e}{4\pi\varepsilon_0} \cdot \gamma \cdot \frac{\zeta}{(\gamma^2\zeta^2 + r^2)^{3/2}} \tag{4.4}$$

$$E_r = \frac{-e}{4\pi\varepsilon_0} \cdot \gamma \cdot \frac{r}{(\gamma^2\zeta^2 + r^2)^{3/2},} \tag{4.5}$$

with $\zeta = z - vt$. The frequency composition can be found by applying a Fourier transformation which yields:

$$\widetilde{E}_r(k,r) = \frac{-e}{2\pi\varepsilon_0} \cdot \frac{k}{\gamma} \cdot K_1(\frac{k}{\gamma}r) \tag{4.6}$$

$$\widetilde{E}_r(k,r) = \frac{-e}{2\pi\varepsilon_0} \cdot \frac{-ik}{\gamma^2} \cdot K_0(\frac{\gamma}{y}r) \tag{4.7}$$

where K_1 and K_0 are the modified Bessel functions. As the longitudinal component is smaller by a factor of γ, it can be neglected in the following.

Consider a bunch of relativistic particles in vacuum approaching an infinite boundary to a medium with permittivity ε. The radiation energy U emitted into the backward hemisphere can be described by the Ginzburg-Frank formula:

$$U = \int_0^\infty \int_0^{2\pi} \int_0^\pi \sin\theta\, U_1(\omega,\theta)\, d\theta\, d\omega\, d\phi\,, \quad \text{with} \tag{4.8}$$

$$U_1 = \frac{e^2}{4\pi^3\varepsilon_o c} \frac{\beta^2 \sin^2\theta \cos^2\theta (\varepsilon-1)^2 \left(1-\beta^2\sqrt{\varepsilon-\sin^2\theta}\right)^2}{(1-\beta^2\cos^2\theta)^2 \left(1+\beta\sqrt{\varepsilon-\sin^2\theta}\right)^2 \left(\varepsilon\cos\theta-\sqrt{\varepsilon-\sin^2\theta}\right)^2} \tag{4.9}$$

$U_1(\omega,\theta)$ is the spectral energy distribution, ω the angular frequency and θ the polar angle of the radiation. A remarkable fact is, that it is independent of the frequency. Letting $\varepsilon \to \infty$ for metallic screens, this simplifies U_1 and yields:

$$U_1 = \frac{e^2}{4\pi^3\varepsilon_0 c} \frac{\beta^2 \sin^2\theta}{(1-\beta^2\cos^2\theta)^2} \tag{4.10}$$

Equation 4.10 is the Ginzburg-Frank formula, commonly used to describe transition radiation for optical beam diagnostics. For the derivation of 4.10 see [LL85]. The intensity maximum of the angular distribution can be found by the differentiation of equation 4.10 with respect to θ:

$$\frac{dU_1}{d\theta} = \frac{\beta^4 c \sin 2\theta}{(1-\beta^2\cos^2\theta)^2} \left(1-\beta^2-\beta^2\sin^2\theta\right) \tag{4.11}$$

Equation 4.11 has to vanish for the maximum energy radiated. This yields an angle of

$$\theta_{max} = \frac{1}{\beta\gamma}. \tag{4.12}$$

Due to the radial polarisation of the electric field of the electron bunch, there is no radiation emitted at $\theta = 0$ (see figure 4.2(a)).

The total spectral energy emitted by a single particle can be derived by integrating equation 4.10 over the solid angle $d\Omega = \sin\theta d\theta d\phi$:

$$\begin{aligned} \frac{dU}{d\omega} &= \int \sin\theta U_1(\theta)\, d\theta\, d\phi \\ &= \frac{e^2\beta^2}{2\pi^2\varepsilon_0 c} \int_0^\pi d\theta \frac{\sin^3\theta}{(1-\beta^2\cos^2\theta)^2} \\ &= -\frac{e^2\beta^2}{2\pi^2\varepsilon_0 c} \left(4 + \frac{1+\beta^2}{\beta} \log\frac{(1-\beta)^2}{(1+\beta)^2}\right) \end{aligned} \tag{4.13}$$

As long as the assumption of an infinitely large screen is valid, the equation is independent of the frequency of the radiation. The radiation energy in the optical regime per electron is thus evaluated by integrating over the optical range

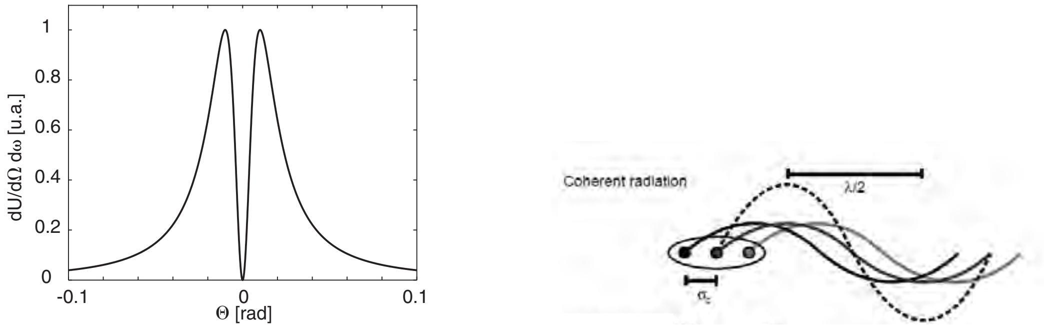

(a) Angular distribution of the optical transition radiation emitted by a single particle

(b) Phase relation and resulting amplitude for the coherent emission process where the wavelength λ is larger than the bunchlength σ_z.

Figure 4.2.: Emission of transition radiation

of frequencies. For lower frequencies, coherence effects have to be taken into account (see section 4.2):

$$U = \int_0^{opt} \frac{dU}{d\omega}\, d\omega \tag{4.14}$$

If one now advances to a bunch of N electrons, the total radiated energy is

$$U_{OTR} = N \cdot U \tag{4.15}$$

The total radiated energy has to take the coherent part of the emitted spectrum into account as well. A natural limit to the emission frequency is the plasma frequency ω_{plasma} of the metal, as for that frequency the dielectric constant approaches unity and the metal does not reflect the electric field anymore. It depends on the square root of the free electron density, and is for metals in the order of $5 \cdot 10^{15}$ Hz.

4.2. Coherent transition radiation

Equation 4.10 describes the spectral energy density per unit solid angle in the optical regime for a sufficiently large screen. If the transition radiation wavelength exceeds the bunch length, the electrons will radiate coherently (see 4.2(b)). The radiated power depends quadratically on the number of involved electrons. For a bunch of $N = 10^9$ electrons, it is clear that considering the spectral energy, the optical part of the spectrum can be neglected compared to the coherent transition radiation.

Diffraction effects

The Ginzburg-Frank formula is obtained by solving the Maxwell equations for a relativistic charge approaching an infinitely large metallic screen. However, two different effects have to be considered when applying this solution to the environment of a linear accelerator. The far-field approximation of the Ginzburg-Frank formula is only valid, if the observation point is far enough away from the CTR screen. Numerical computations yield a condition for the far-field of

$$d \gg \gamma^2 \lambda, \tag{4.16}$$

where d is the distance to the screen.

Furthermore, the finite screen size in the accelerator plays a role as to when the Ginzburg-Frank formula can be used. In our case, the diameter of the CTR screen was 57 mm. Again through numerical calculation, a condition can be derived

$$\gamma\lambda \leq a, \tag{4.17}$$

where a is the radius of the screen. An analytical formula can be derived taking into account the finite screen size, but in the far-field [BG00]. For the case of optical wavelengths, the above conditions are fulfilled. But in the case of wavelengths in the millimeter regime, they are not easily valid anymore.

Consider a metallic circular screen of radius a. Applying Kirchhoff's diffraction theory, the point (ξ, η) of the target contributes to the electric field strength in a point $P = (x, y = 0)$ on a view screen at a distance d (see figure 4.3) the following amount:

$$d\widetilde{E}_x = \widetilde{E}_r(\rho) \cos\phi \cdot \frac{e^{ikR}}{R} \cdot \rho \, d\phi \, d\rho \tag{4.18}$$

where ϕ is the inclination angle and

$$\xi = \rho\cos\phi, \quad \eta = \rho\sin\phi \quad \text{and} \quad E_x(\rho) = E_r(\rho)\cos\phi. \tag{4.19}$$

So the total electric field strength at the point P is:

$$\tilde{E}_x(P) \propto -\frac{i}{\lambda} \underbrace{\iint}_{\text{OTR target}} \tilde{E}_r \cdot \cos\phi \cdot e^{\frac{ikR}{R}} dS \tag{4.20}$$

From figure 4.3, one can derive the following expression for the distance between (ξ, η) and P:

$$R = \sqrt{d^2 + (x-\xi)^2 + \eta^2} \approx d + \frac{x^2 + \rho^2}{2d} - \frac{x\rho\cos\phi}{d} \tag{4.21}$$

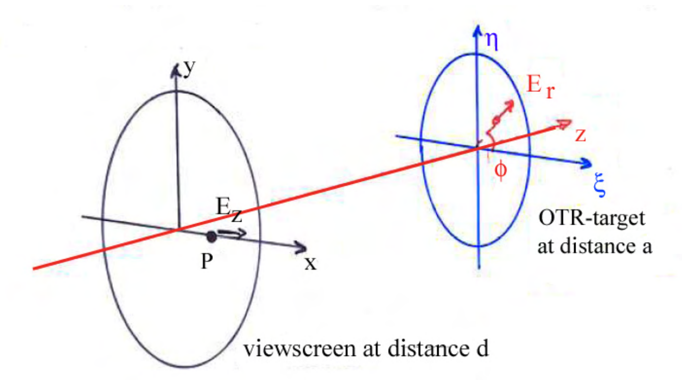

Figure 4.3.: Scheme of the OTR-Screen

Using the Fraunhofer expansion for the far field, equation 4.21 can be approximated by

$$R \approx d - \frac{x\rho\cos\phi}{d}. \tag{4.22}$$

Inserting this into equation 4.20 yields

$$\tilde{E}_x(P) \propto \frac{k^2}{\gamma} \cdot \frac{e^{ikd}}{d} \cdot \int_0^a \underbrace{\left[\int_0^{2\pi} e^{ik\theta\rho\cos\phi} \cos\phi d\phi\right]}_{-2\pi i J_1(k\theta\rho)} K_1\left(\frac{k}{\lambda}\rho\right) \rho\, d\rho.$$

The intensity is thus

$$I_1(\theta) \propto \frac{k^4}{\gamma^2} \left| \int_0^a J_1(k\theta\rho) \cdot K_1(\frac{k}{\gamma}\rho)\rho\, d\rho \right|^2, \tag{4.23}$$

which is only valid in the far field approximation.
For the near field, one uses the Fresnel approximation and directly inserts equation 4.21 into equation 4.20. This yields for the intensity in the near field approximation

$$I_2(\theta) \propto \frac{k^4}{\gamma^2} \cdot \left| \int_0^a J_1(k\theta\rho) \cdot K_1(\frac{k}{\gamma}\rho)\rho \cdot e^{ik\frac{\rho^2}{2d}}\, d\rho \right|^2. \tag{4.24}$$

Assuming a γ of around 200, an OTR-screen diameter of 57 mm, a wavelength of the CTR radiation of 3 mm and a distance of the view screen of 200 mm yields for the far field criteria:

$$a \geq \gamma\lambda = 0.6\,\text{m} \quad \text{and} \quad d \gg \gamma^2\lambda = 120\,\text{m} \tag{4.25}$$

So they are both clearly not fulfilled. Figure 4.2 shows the numerically computed angular distribution of 100 GHz CTR radiation in comparison with the Ginzburg-Frank formula for the case of the measurement setup at the SLS. It is obvious that diffraction effects have to be taken into account when simulating the CTR radiation profile at the ZnTe crystal.

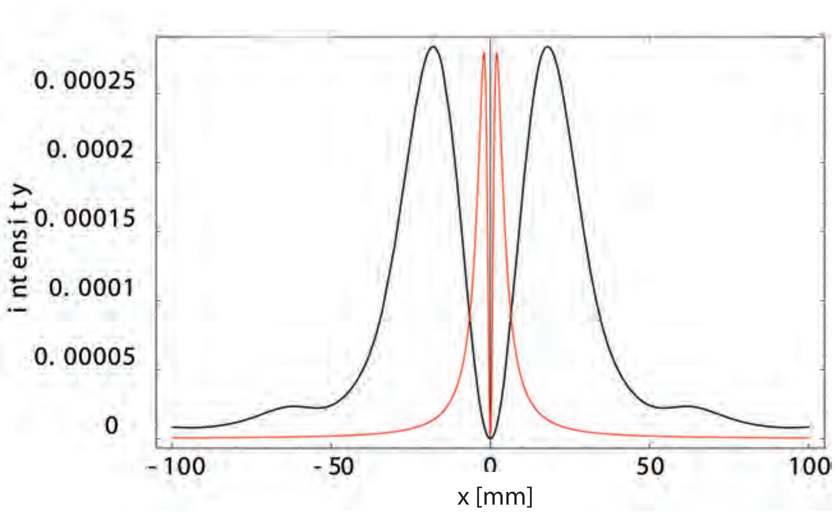

Figure 4.4.: Simulated CTR radiation distribution at the crystal for f=100 GHz using the Ginzburg-Frank formula (grey) and using the near field approximation (black)

5. Experimental setup

The integration of an optical experiment into an accelerator environment imposes constraints onto the experimental setup. As it is not possible to access the linac bunker during operation, many parts (mirrors, quarter-wave plate, fibrecouplers etc.) have to be remotely controllable from the outside. For the same reason the laser system cannot be put inside the linac bunker close to the interaction point between laser pulse and CTR, so the laser pulses have to be transported into the experimental area via an optical transfer line. In this chapter, the necessary adjustments of the experiment to meet the constraints of an accelerator environment, the SLS linac itself and the generation of the electro-optic signal, which was described in general terms in chapter 2, will be discussed.

The Swiss Light Source (SLS) is a 2.4 GeV third generation synchrotron facility, built in 1998/1999. The accelerator consists of three main parts, namely the linac used as pre-accelerator to 100 MeV, the booster to accelerate the particles to 2.4 GeV and the storage ring with its insertion devices to generate the synchrotron light used by the beamlines. The booster and storage ring have a nearly similar circumference of 288 m. Both booster and synchrotron run at a frequency of 500 MHz, but the two travelling wave acceleration structures of the linac run at 3 GHz.

5.1. The SLS linac

The present EOS measurements have been conducted at the SLS linac, which is a 100 MeV travelling wave accelerator, based on a concept developed by DESY. A schematic view is shown in figure 5.1. The linac uses a triode gun followed by a 500 MHz prebuncher, a 4-cell 500 MHz buncher and a 16-cell 3 GHz buncher which compresses the bunches to the short lengths needed for for the 3 GHz accelerating structures. A set of focusing quadrupoles is situated between and after the two accelerating structures. The beam passes the experimental station ALIDI-SM5[1] where the EOS experiment is mounted and is injected into the booster ring using a dipole magnet. The main parameters of the SLS Linac are summarised in table 5.1. The task of the linac system is to achieve a maxi-

[1] The name of the station in the SLS control system

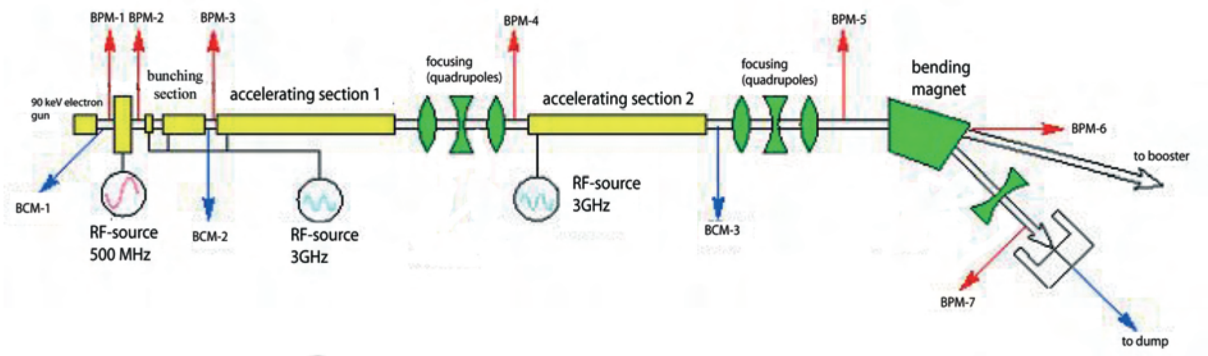

Figure 5.1.: Schematic of the SLS linac

final energy	100 MeV
travelling wave acceleration structures	2·5.2 m
RF frequency	3 GHz
pulse length:	
single bunch mode	1 ns
multi bunch mode	700 ns
charge per bunch	0.5 . . . 1 nC
normalised emmitance	<50 π mm mrad
travelling wave bunchers	2 at 3 GHz
subharmonic prebuncher	1 at 500 MHz
electron gun voltage	90 kV
cycle rate	3.125 Hz

Table 5.1.: SLS Linac parameters

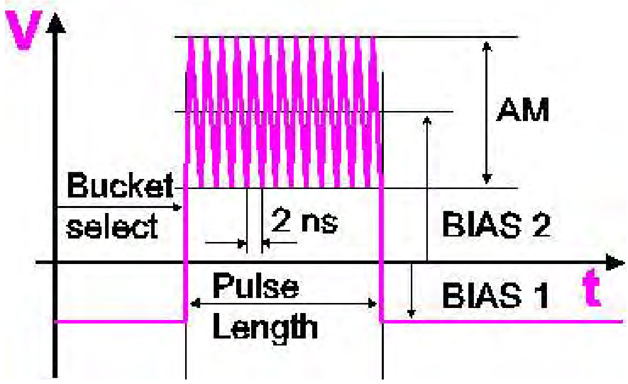

Figure 5.2.: Schematic of the applied voltage at the gun grid

mum beam transmission into the booster and the synchrotron while keeping the emittance as low as possible.

5.1.1. The gun

The electron source is a 90 kV triode gun. The so-called dispenser cathode is a porous tungsten matrix, impregnated with different oxides like BaO, CaO and Al_2O_3. The electrons are emitted from the thermionic cathode and accelerated by the anode voltage. The time structure and the charge of the beam are controlled by the voltage of the grid, which is a superposition of a DC bias voltage with a radiofrequency voltage. A schematic is shown in figure 5.2.

A 500 MHz oscillation is applied for 200-900 ns duration (=pulse length) to generate a train of 100-450 bunches for filling the corresponding RF buckets of the booster. Since the booster operates at 500 MHz, the distance between bunches is 2 ns. In single-bunch mode, a single burst of about 1 ns duration is applied to generate one strong bunch for a single booster bucket. These modulations are repeated at 3.125 Hz which is the macropulse repetition rate (this is explained in more detail in section 6.3). A negative dc offset (BIAS1) prohibits electron extraction from the cathode between pulses, a rectangular pulse (BIAS2) enables the emission, and the superimposed amplitude modulation generates the 500 MHz modulation structure of the electron bunch.

5.1.2. The bunching system

After the cathode, the bunches enter the subharmonic prebuncher, operating at a frequency of 500 MHz. Its purpose is to increase the modulation depth of the electron beam leaving the gun and thus to collect the particles in bunches. Particles arriving too early are decelerated, particles arriving too late are accelerated (see figure 5.3(a)). The beam is not yet relativistic, so a velocity

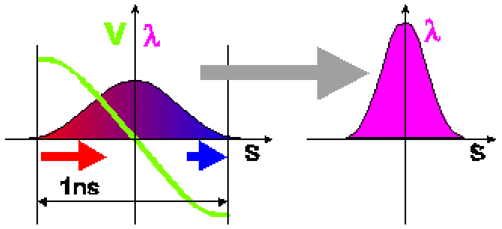

(a) Principle of the 500 MHz subharmonic pre-buncher

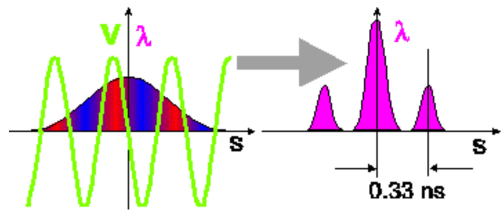

(b) Principle of the 3 GHz pre-buncher

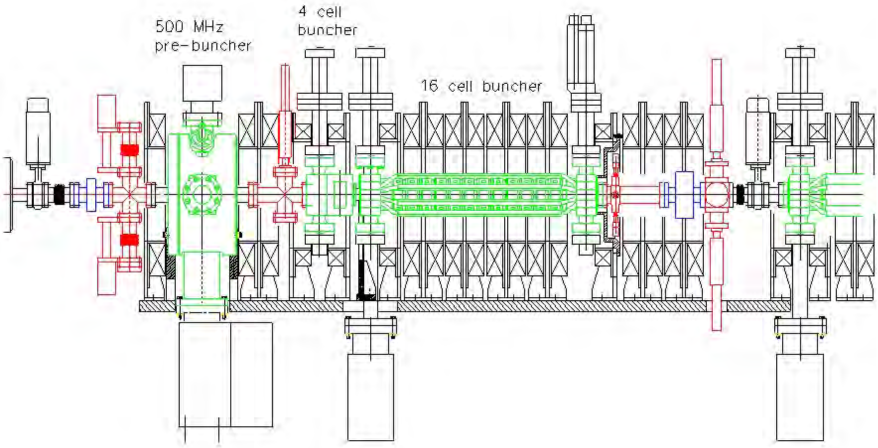

(c) Schematic of the SLS Linac bunching system

Figure 5.3.: Overview over the bunching mechanisms at the SLS linac (from [Pau04])

dispersion is introduced. That means that the electrons in the bunch acquire a position dependent velocity. If the chirp has the correct sign (eg. fast particles at the tail of the bunch, slow particles at the head) the tail particles catch up, the leading particles slow down and thus the bunch is compressed after a certain drift space.

The acceleration frequency of the cavities is 3 GHz. This frequency is too high to be applied to the gun grid. This is why the gun and the first pre-buncher operate at the subharmonic frequency of 500 MHz. The second pre-buncher operates at 3 GHz like the accelerating sections. Its task is to create a 3 GHz modulation in order to make the beam acceptable for the 3 GHz travelling wave structures of the main linac. The 3 GHz prebuncher "chops" the 1 ns bunch from the subharmonic buncher into 3 smaller bunches separated by 0.33 ns (see figure 5.3(b))

The final 16-cell buncher also operates at 3 GHz and again increases the modulation depth from the prebuncher, and so further compresses the bunches coming from the 3 GHz prebuncher. At the same time it also accelerates the beam to an energy of approximately 4 MeV in order to "freeze" the time structure of the bunch due to its now highly relativistic motion. Although the final buncher is working both as buncher and as accelerating section, it is optimised for optimum bunching and minimum energy spread and not for the highest acceleration field. The actual acceleration is accomplished in two 3 GHz traveling wave structures, the first accelerating the beam to an energy of 50 MeV, the second to its final energy of 100 MeV without changing the time structure of the beam.

5.1.3. Linac timing

For the EOS experiment, a new mode had to be implemented in the SLS timing system. The initial planning of the experiment was to operate it as a parasitic measurement, while the linac is used to fill the storage ring. The normal operating mode of the SLS is called "top-up". This new way of refilling the storage ring provides an almost constant average beam current. In top-up mode, the beam is not dumped when a filling is needed, but the charge of each bucket is periodically replenished.

As the central frequency of the booster and storage ring is 500 MHz, a shift of 2 ns has to be applied after each bunch injection into the booster in order to inject into the next bucket. A top-up happens about every 5 minutes.

Top-up mode is incompatible with EOS measurements, as they require a transition radiation screen in the linac, as will be shown in section 5.2.3. The EOS measurements were therefore conducted during SLS shutdown when the linac was available, but not needed for filling the storage ring. The modifications, which had to be made to the linac timing system which will be discussed in section 6.3.

5.2. Measurement setup

Coherent transition radiation is coupled out of the beam pipe of the 100 MeV linac at the experimental station ALIDI-SM 5. The 15 fs TiSa-laser beam is coupled into the linac bunker using a 15 m transfer line. The experimental setup consists of 3 main parts:

5.2.1. Setup outside the linac

The laser is mounted on an optical table in the technical gallery of the SLS. The entire SLS hall is temperature stabilised to 23°C±2° C. This is very beneficial to a stable operation of the femtolaser system. The laser system itself is mounted on a "breadboard" which rests of 4 vibration dampers on a large optical table. This reduces the mechanical vibrations substantially (see section 5.3).

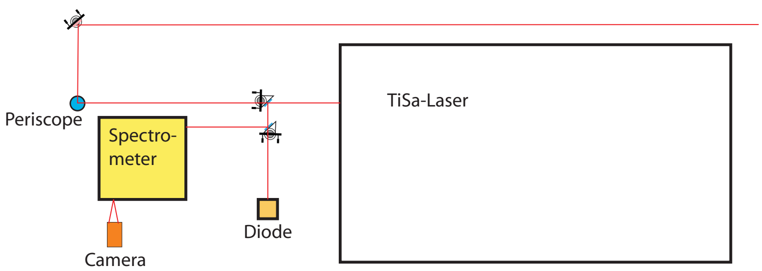

Figure 5.4.: Setup of the laser system outside the SLS linac bunker

Figure 5.4 shows the setup outside the linac bunker. A part of the TiSa beam is coupled into a 12 GHz photodiode for the synchronisation unit and another part of the beam is coupled into a spectrometer for diagnostic purposes. The spectrometer enables a realtime monitoring of the mode lock condition of the laser. When mode-lock is achieved, the bandwidth of the laser is 65 nm and, compared to a narrow line observed in cw operation.

A HeNe laser or a pulsed frequency doubled Nd:YAG laser can be coupled into the beam transfer line using flip mirrors. The HeNe laser is used to align the optics in the linac bunker, the Nd:YAG laser to determine the correct pulse of the balanced detector output (see section 7.2.1).

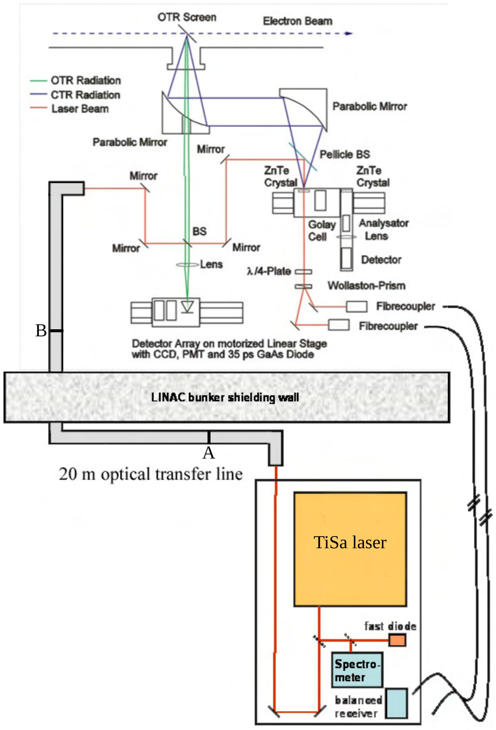

Figure 5.5.: Schematic of the optical laser beam transfer line

5.2.2. Beam transfer

The laser beam transfer into the bunker is accomplished by a series of tubes with fixed adjustable mirrors mounted at each bend of the system. To keep the beam diameter small at the experimental area inside the linac tunnel, two lenses with a focal length of 4 m each are introduced at positions A and B (see figure 5.5). The beam spot at the laser output coupler is then imaged to a spot close to the crystal. Without the focusing, the laser spot size would grow to 40 mm. The dispersion in the lenses lengthens the femtosecond laser pulses to about 120 fs FHWM. This is still acceptable for a measurement of the SLS linac electron bunches. Measurements using the CTR radiation and a Martin-Pupplet Interferometer suggest a pulse length of 4 ps (FWHM) [Sue04].

The beam transfer line was very stable, neither on short-term nor long-term motion of the laser spot position inside the linac was observed.

5.2.3. Setup inside the linac bunker

The electron bunch transits a transition radiation (TR) screen in the experimental station ALIDI-SM5. A schematic representation of the setup is given in figure 5.6. The TR screen consists of a 380 μm thick silicon waver onto which

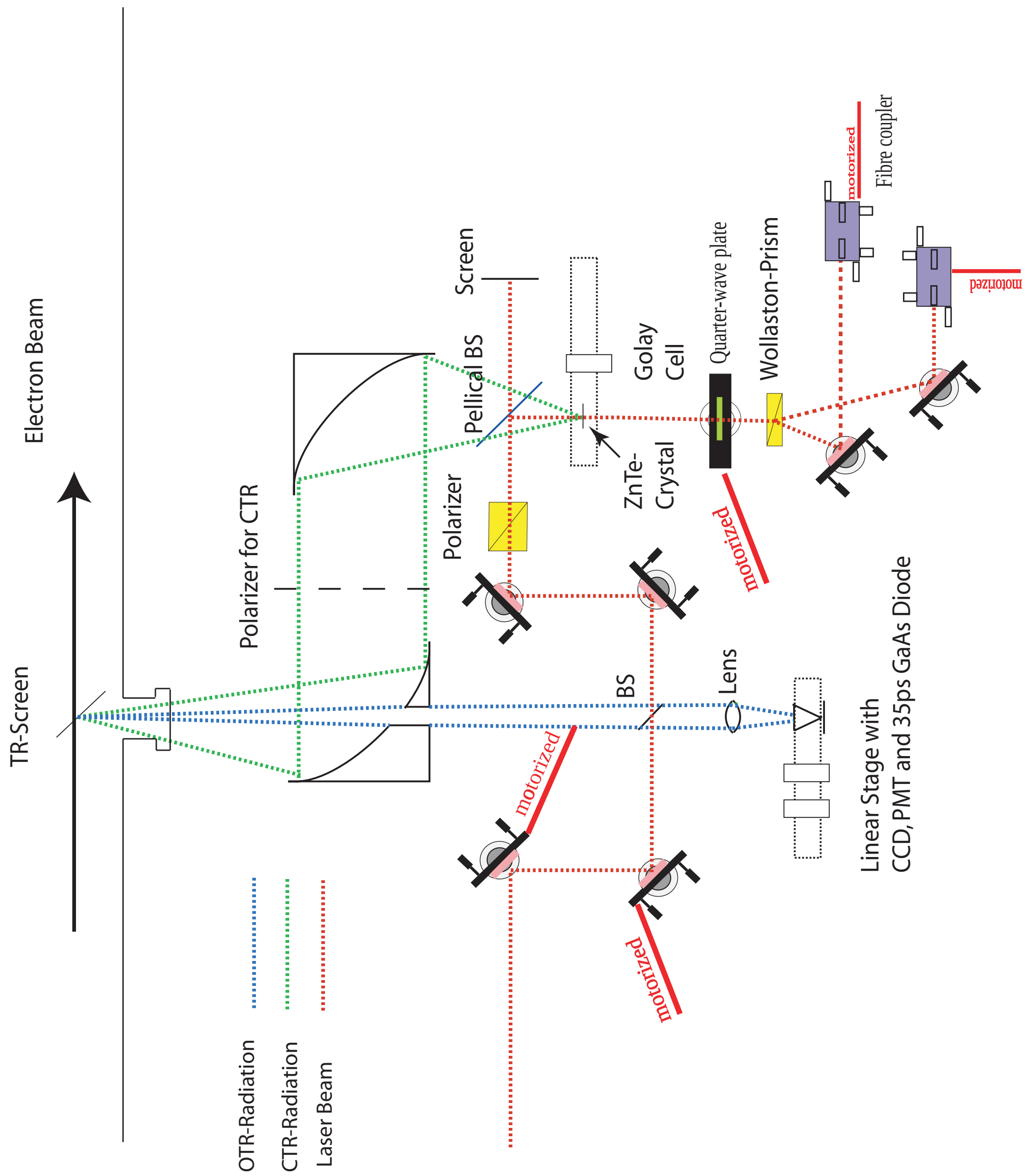

Figure 5.6.: The experimental setup inside the linac bunker

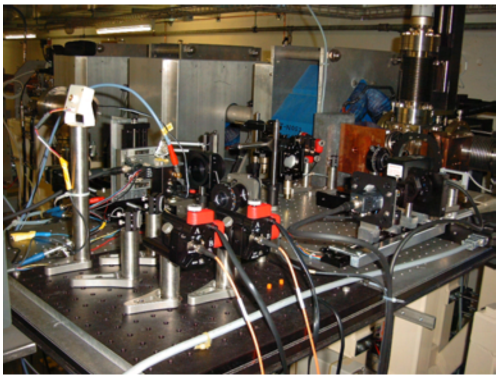

(a) Overview

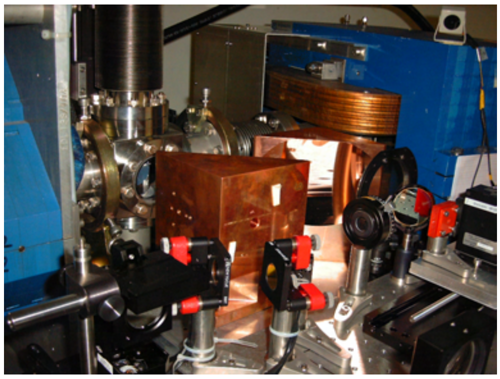

(b) OTR screen, copper paraboloid mirrors and ZnTe crystal (in red holder)

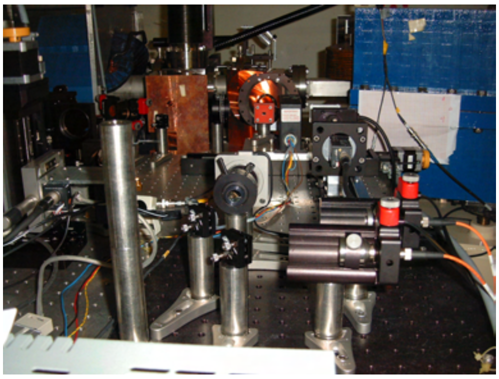

(c) Overview (beampipe in rear, electrons coming from left)

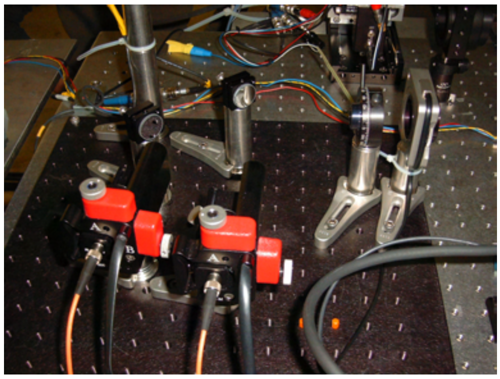

(d) Quarter-wave plate, Wollaston prism and fibre couplers

Figure 5.7.: Images of the experimental setup inside the linac bunker.

a 1 μm thin aluminium coating is evaporated. It is mounted under an angle of 45° with respect to the electron beam direction in order to reflect the transition radiation out of the vacuum pipe.

The optical part of this radiation (OTR[2]) has only a small divergence of $\pm\frac{1}{\gamma} \approx \pm 10$ mrad with respect to the 90° direction of optical reflection at the inclined TR screen (see section 4). For the coherent part of the emitted spectrum (CTR[3]), the divergence is considerably larger due to diffraction effects. As the wavelength of the CTR is around 1 mm and the target diameter is a=57 mm(limited by the vacuum pipe), the crystal is in the near field, so the Ginzburg-Frank equation cannot be applied (see section 4.2).

The CTR radiation is focused onto the ZnTe crystal using two parabolic copper mirrors with a focal length of 250 mm. A hole with a diameter of 12 mm lets the optical radiation pass straight through. The OTR then passes a beam splitter and is focused by a lens with a focal length of 300 mm onto a photomultiplier. The photomultiplier is mounted on two remotely controlled motorised sleds together with an avalanche diode, a PIN-diode with a bandwidth of 12 GHz and a CCD-camera. This allows to move the desired detector into the correct position and to adjust the height. Part of the femtolaser radiation is also guided onto the photomultiplier using a thin glass beam splitter. The photomultiplier is important to adjust the temporal overlap of the TiSa pulse and the OTR to nanosecond precision (see section 7.2)

Two remotely controlled picomotor driven mirrors are used to adjust the laser beam position. The laser beam passes a Glan-Thomson polariser to compensate for polarisation changes during beam transfer. The laser beam is reflected onto the ZnTe crystal by a pellicle beam splitter. The ZnTe crystal is mounted on a motorised sled, together with a Golay cell. The Golay cell enables a good determination of the CTR focus and of its integrated intensity. Behind the non-linear crystal is a quarter wave plate and a Wollaston prism, which separates the two orthogonal polarisation components. These are then guided into two motorised fibre couplers and transferred outside the linac bunker. The balanced diode detector is located outside the linac area to minimise effects due to electromagnetic noise inside the linac bunker.

5.3. Vibrational stabilisation

Vibration measurements were carried out by Peter Hottinger (PSI) using a spectrum analyzer with acceleration sensors (ICP 393 B31) together with seismic

[2]Optical Transition Radiation
[3]Coherent Transition Radiation

Meas. Nr.	vertical axis		horizontal axis		
	frequency [Hz]	amplitude [nm]	frequency [Hz]	amplitude [nm]	duration [min]
sensor at middle of optical table					
A	16.5	6.57	16.5	47.36	5
B	16.5	10.46	16.5	44.55	60
sensor at corner of optical table					
C	16.5	14.67	16.5	93.54	12
D	16.5	15.8	16.5	91.56	270
sensor on breadboard					
E	12.44	49.62	6.8	65.44	5
F	12.44	66.80	6.81	84.44	780
G	8.00	91.38	7.12	87.73	10
H	8.25	93.49	7.19	169.60	750

Table 5.2.: Peaks with maximal amplitude of vibration measurements

sensors on the Y- (SN 9746) and X-axis (SN 7894) with a resolution of 10V/g. The aim was to determine the amplitude of the ground motion at the SLS both during normal working hours (e.g. with crane movement) and during quieter times. Both the middle and the sides of the big optical table, which is coupled directly without damping onto the concrete floor, and the "breadbord" on which the laser is mounted were chosen for measurements (see 5.3). With this setup, it was possible to check the efficiency of the vibration dampers installed under the breadboard. Both short-term (5 min) and long-term (overnight) measurements were conducted.

Table 5.2 shows, that the maximum displacement on the optical table occurs at 16.5 Hz with an amplitude of around 10 nm in the vertical coordinate and between 40 and 90 nm in the horizontal coordinate. On the laser table, resonances are found at 7 Hz, which were expected due to the mechanical resonance of the passive vibration dampers. But the peaks around 16.5 Hz (see figure 5.3) are already damped by a factor of two compared to the measurements on the optical table. The long term measurements with durations of 60 min up to 720 min show no significant increase in the maximal amplitudes. Even though the reduction of the peaks at 16 Hz has to be traded off with a large increase of the amplitude at 7 Hz, the vibrational dampers of the breadboard are still very advantageous, because low-frequency oscillations are strongly suppressed by an integrator in the synchronisation circuit (see section 6.7.2).

Measurements G and H were conducted while the crane of the SLS was in operation. Comparing this with measurements E and F, where the crane was not in operation, one can see that besides a general increase in the noise floor

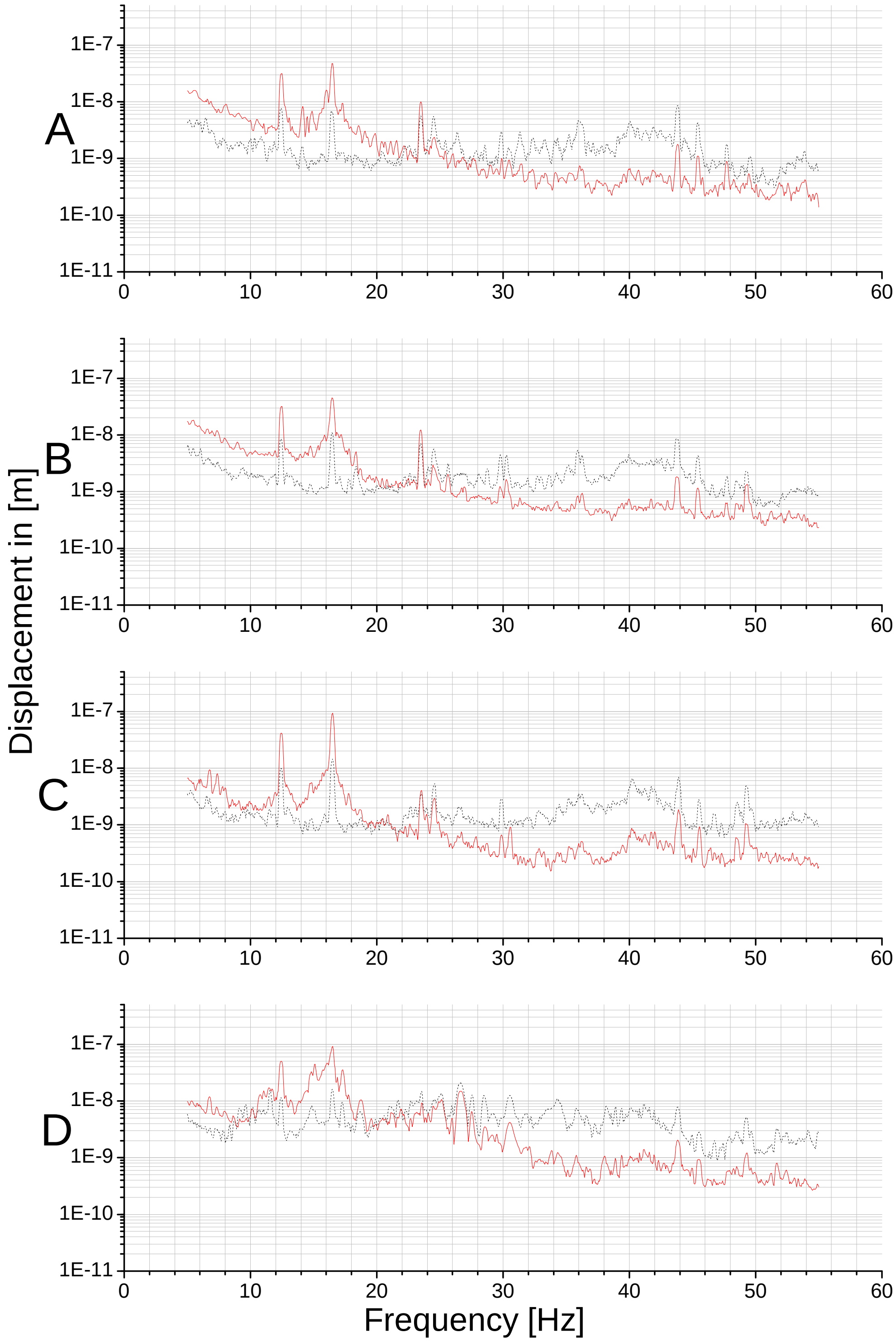

Figure 5.8.: Measurements of the vibrational spectra. Sensors were placed in the middle of the optical table (A and B) and on a corner (C and D). (grey: amplitude in horizontal direction; black: amplitude in vertical direction)

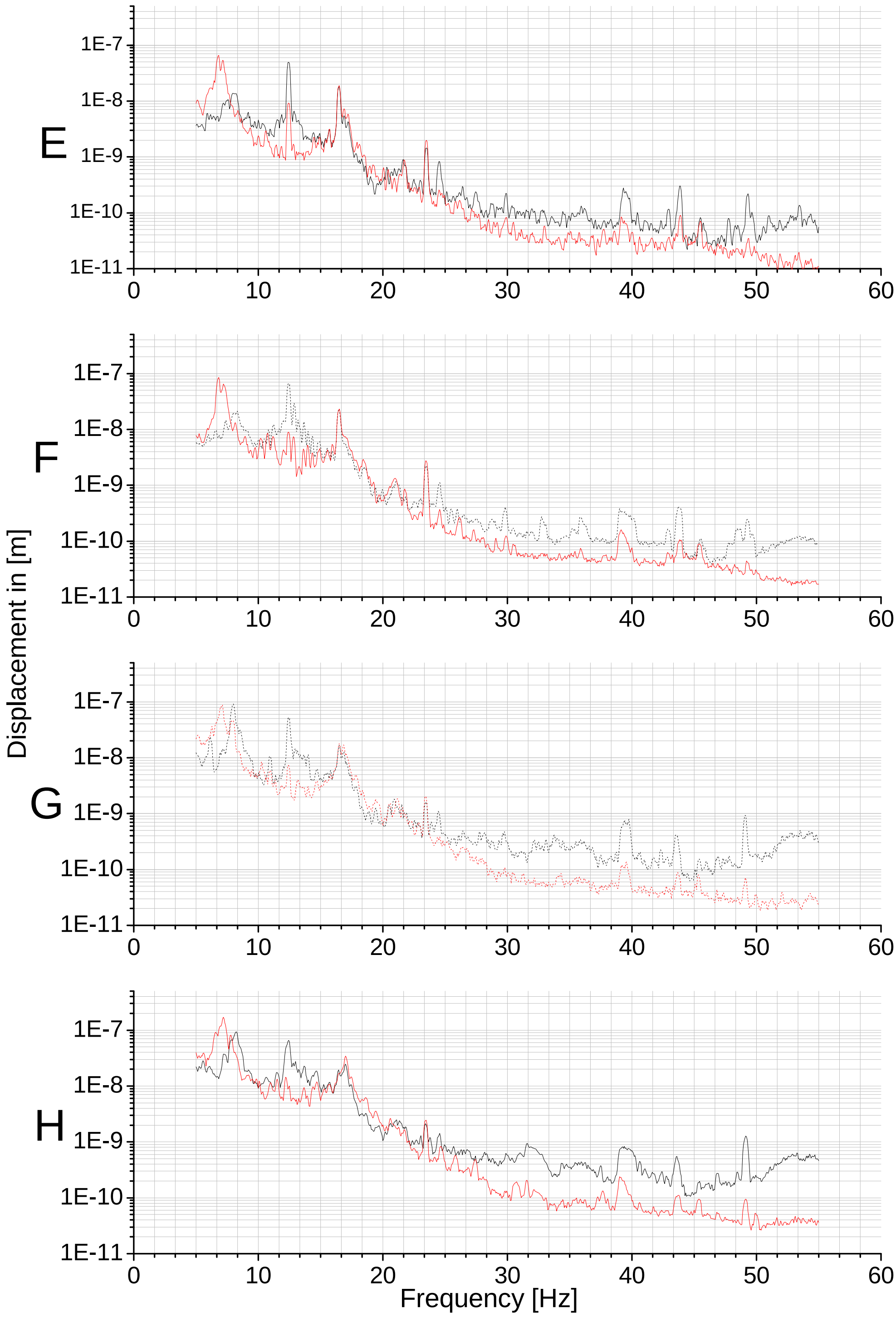

Figure 5.9.: Measurements of the vibrational spectra. Sensors were placed on the damped breadboard of the laser. (grey: amplitude in horizontal direction; black: amplitude in vertical direction)

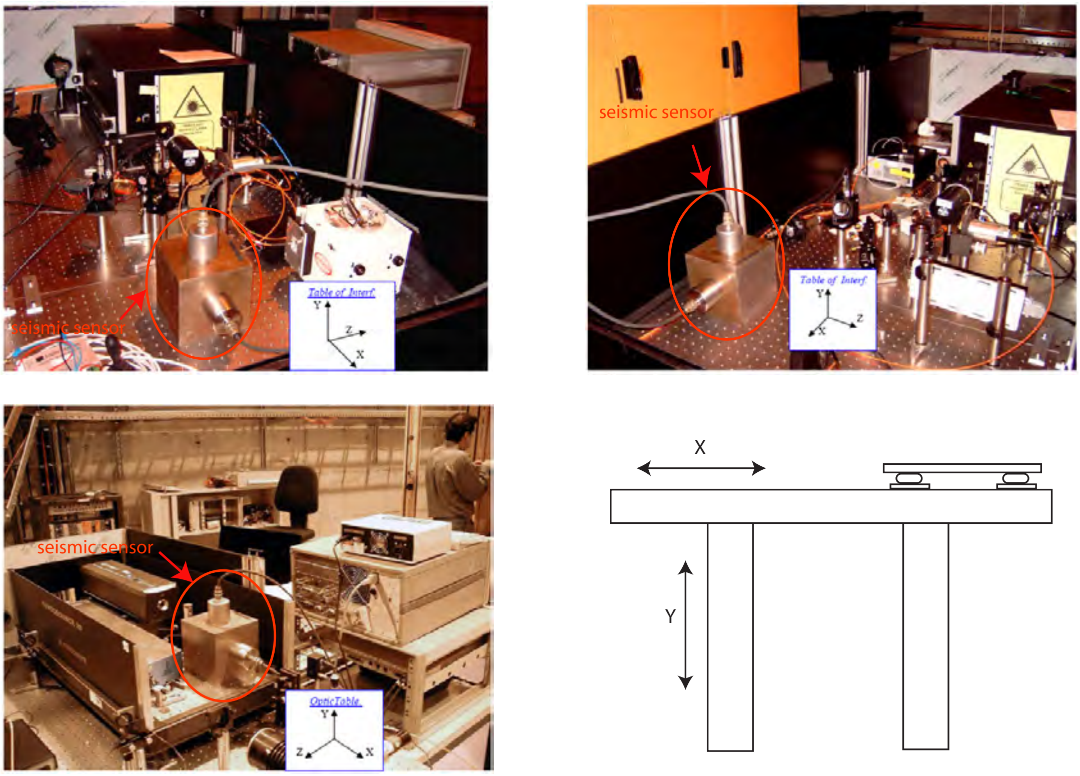

Figure 5.10.: Position of the seismic sensor: top left: center of optical table, top right: corner of optical table, bottom left: on laser breadboard

one significant peak arises around 8 Hz in the displacement of the Y-direction.

The overall noise floor is an order of magnitude smaller on the laser "breadboard" than on the undamped optical table. This noise reduction was one of the measures employed to reach the best possible level of synchronisation.

5.4. Principle of the detection scheme

5.4.1. Upper estimation of the field strength at the crystal

The electron energy at the OTR screen is $E = 100$ MeV. Assume as an example an electron bunch with a leading gaussian peak with $\sigma_t = 1.5\,\mathrm{ps}$ and a charge of $0.5\,\mathrm{nC}$. The transition radiation energy emitted into the backward hemisphere by a single electron crossing the OTR screen is

$$W = \frac{e^2}{2\pi^2 \varepsilon_0 c} \ln \gamma \tag{5.1}$$

where γ is the Lorentz factor. To obtain the coherent radiation emitted by a bunch of N electrons, one has to convolute the charge distribution of the bunch

$$\rho(t) = \frac{N}{\sqrt{2\pi}\sigma} \exp\left(-\frac{t^2}{2\sigma_t^2}\right) \tag{5.2}$$

with the spectral distribution:

$$\frac{dW_N}{d\omega} = W \left| \int_{-\infty}^{+\infty} \rho(t) \exp(i\omega t)\, dt \right|^2 = N^2 W \exp(-\sigma_t^2 \omega^2) \tag{5.3}$$

The frequency range accepted by the setup is about 50 to 800 GHz. Integration of equation 5.3 yields as an upper limit of the CTR pulse energy as diffraction effects are not taken into account

$$W_{CTR} \approx 40\,\mu\mathrm{J}. \tag{5.4}$$

The CTR is focused by two parabolic mirrors with a focal length of $f = 200\,\mathrm{mm}$ onto the ZnTe crystal. The spot size at the crystal (see section 7.1) has a mean radius of $r \approx 3\,\mathrm{mm}$. Then the intensity of the $\delta t = 3.45$ ps (FWHM) long CTR pulse on the crystal would be in the ideal case

$$I_{CTR} \approx \frac{W_{CTR}}{\pi r^2 \delta t} \approx 4 \cdot 10^{11}\, \frac{\mathrm{W}}{\mathrm{m}^2}. \tag{5.5}$$

However, a number of losses have to be considered:

1. The radiation is emitted through a quartz window which shows good transmission of about 0.9 in the interesting region of the spectrum of up to several 100 GHz.

2. The CTR is polarised using a wire grid. The expected loss is approximately 50%.

3. The CTR is projected onto the crystal using a 1:1 image. However the parabolic mirrors are not perfect and the image is not exact. The losses in the optical system can be estimated to 50%.

The index of refraction of ZnTe in the THz regime is $n = 3.1$. For an intensity

$$I_o = 0.25 \cdot I_{CTR} = w \cdot c = \frac{1}{2}\varepsilon_0 E^2 \tag{5.6}$$

and a perpendicular angle of incidence, the intensity transmitted into the crystal is

$$\frac{I_{tr}}{I_0} = 1 - \left(\frac{n-1}{n+1}\right)^2 = \frac{4n}{(n+1)^2} \tag{5.7}$$

This yields an electric field strength inside the crystal taking into account the losses due to the dielectric constant of ZnTe:

$$E_{ZnTe} = \sqrt{\frac{2I_{tr}}{\varepsilon_0 nc}} = 4 \cdot 10^5 \, \frac{\mathrm{V}}{\mathrm{m}} \tag{5.8}$$

Using this field strength and equation 2.34 with the appropriate values for ZnTe ($r_{41} = 4 \cdot 10^{-12}\,\mathrm{m/V}$, $n_{optical} = 2.8$) and a crystal thickness of 1 mm, one can calculate the maximum phase shift to:

$$\Delta\phi_{max} = 0.28\,\mathrm{rad} = 16° \tag{5.9}$$

5.4.2. Detection using a quarter-wave plate and a Wollastone prism

- E_{CTR}=0
  ZnTe is an isotropic crystal for vanishing external electric fields, due to its symmetry. That means the polarisation of a probe pulse remains unchanged, no matter what the direction or angle of incidence is. The quarter wave plate coverts the linear polarisation of the probe pulse into a circular polarisation. The Wollaston prism splits the circularly polarised pulse into two linearly polarised pulses with orthogonal polarisation which are coupled into two fibre couplers. The intensity of both pulses is identical and the difference signal of the balanced detector vanishes.

- $E_{CTR} \neq 0$ parallel to the (-1,1,0) axis
  The ZnTe exhibits birefringence with an external electric field present. As $\alpha = 0$ in this case, the main axis of the index ellipse has an angle of 45° relative to the X axis (see section 2.2.2). The field vector of the horizontally polarised probe laser pulse has to be projected onto the long, respectively short half axis of the index ellipse. The two components receive different phase shifts. Behind the ZnTe crystal the laser beam has a slight elliptical polarisation. Behind quarter-wave plate and Wollaston prism, the two now separated orthogonally polarised beams have different intensities. Therefore, the balanced detector shows a signal (see figure 5.11).

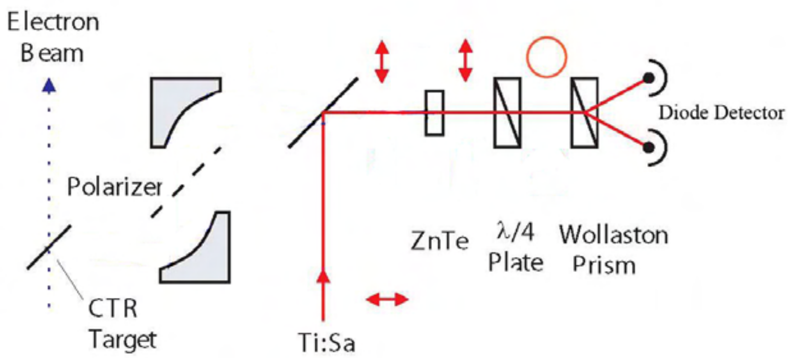

(a) without CTR radiation

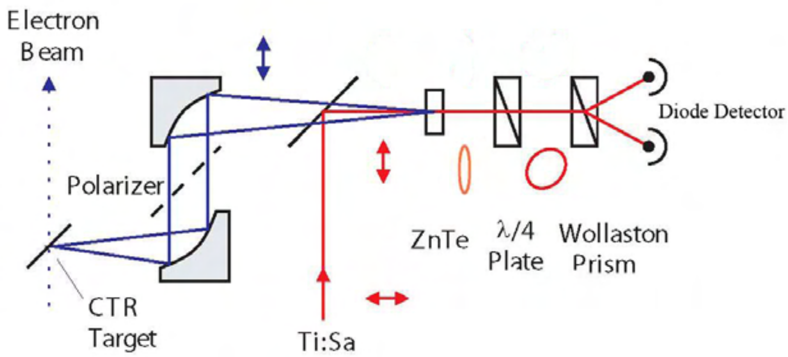

(b) CTR radiation present

Figure 5.11.: Simplified view of the signal detection using a quarter-wave plate, Wollaston prism and a balanced diode detector. The laser and CTR radiation are polarised horizontally.

6. Synchronisation

Key to a successful bunch length measurement using EOS is a precise synchronisation between the femtosecond laser pulses and the RF of the accelerating modules of the linac and thus a precise knowledge of the arrival time of the electron bunch at the experimental area. The RF of an electron accelerator ranges from 300 MHz to about 10 GHz. A repetition rate of a laser in that range is not possible, because it scales inversely with the overall optical length of the cavity. To achieve a repetition rate of 1.3 GHz (the RF used for the TTF2 accelerating modules), a cavity length of only 11.5 cm would be required. The integration of the TiSa crystal alone requires more space. Thus the laser is operated at a subharmonic of the linac RF, typically around 80 to 100 MHz.

The resolution of the EOS experiment is limited on the one hand by the duration of the pulse of the femtosecond laser, and on the other hand by the synchronisation accuracy. In this chapter, the scheme used at the SLS-Linac will be described which has a measured synchronisation accuracy of below 40 fs (rms). Yet the ultimate limit of the resolution of the EOS experiment is given by the response function of the ZnTe crystal. The thinner the crystal is, the better the temporal resolution gets. For the 1 mm crystal used during the measurements at the SLS linac, simulations yield a temporal resolution (FWHM) of:

$$\delta t = 2.5\,\mathrm{ps} \tag{6.1}$$

6.1. General remarks

In this section, some general aspects of control systems will be summarised, along with a discussion of the most important stability parameters. The treatment follows partly books by C.L. Phillips [PH00] and J. Lunze [J.L96]. A simple controller consists of a plant, which is the device one wishes to regulate, a sensor who measures the plant output signal and a compensator who modifies the properties of the sensor signal to enable the control of the system (e.g. amplifiers and integrators). Some sensors already compare the measured signal to an additional reference. This type of sensor is used in the TiSa synchronisation scheme. The principal setup is shown in figure 6.1. The idea of closed-loop controlling is to generate an error signal, by comparing the output to a reference value and feeding this back to the input. If this is done in the form of negative

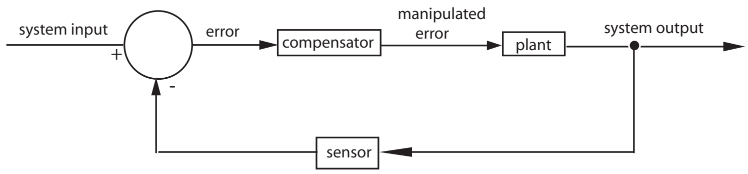

Figure 6.1.: Schematic of a single-loop control system

feedback (e.g. positive deviation is subtracted from the input and vice versa), it is possible to keep the output signal at the desired reference.

When modeling controllers it is important to distinguish between the open-loop state (e.g. when the system has no feedback) and closed-loop (when feedback is active). In an open-loop system, the output signal $c(t)$ only depends on the input signal $r(t)$ and thus on external forces, whereas in the closed-loop system, the filtered and amplified error signal is fed back into the system.

6.1.1. Description of linear systems using differential equations

The differential equation of electronic circuits in time domain follows directly from Kirchhoff's law. Linear systems are described by a set of ordinary differential equations. The dynamic properties of the system are invariant in time, so the result is a differential equation with constant coefficients.
The equation in general has the following form:

$$\begin{aligned} a_n \tfrac{d^n c}{dt^n} + a_{n-1} \tfrac{d^{n-1} c}{dt^{n-1}} + \ldots + a_1 \tfrac{dc}{dt} + a_0 c(t) = \\ b_q \tfrac{d^q r}{dt^q} + b_{q-1} \tfrac{d^{q-1} r}{dt^{q-1}} + \ldots + b_1 \tfrac{dr}{dt} + b_0 r(t). \end{aligned} \tag{6.2}$$

Equation 6.2 is a linear ordinary n-th order differential equation, which describes the dynamic correlation between the input signal $r(t)$ and the output signal of the plant $c(t)$, where a_i and b_i are real coefficients, which can be evaluated from the parameters of the system. For a given input function $r(t), t > 0$ an explicit solution $c(t), t \geq 0$ exists and can be calculated, if the initial conditions $c_{01}, c_{02}, \ldots, c_{0n-1}$ are known.

For a linear system, the superposition principle holds: For a linear combination of input signals

$$u(t) = kr_1(t) + lr_2(t), \tag{6.3}$$

the output signal $c(t)$ can be written as

$$c(t) = kc_1(t) + lc_2(t), \tag{6.4}$$

where $c_1(t)$ is the solution of equation 6.2 with $r = r_1(t)$ and $c_2(t)$ the solution with $r = r_2(t)$.
We consider here a control system, which can be described by a differential equation of the type 6.2. However, it is much more convenient to use the so called state-space form. A state of a system at a time t_0 is defined as the complete information at t_0 that uniquely determines the response of the system for all $t \geq t_0$.

Assume state variables x_n $(n \geq 1)$ defined, such that

$$x_{n+1}(t) = \dot{x}_n(t). \tag{6.5}$$

Taking as an example the model of an harmonic oscillator used to describe the resonance characteristic of the piezo controlled mirror in section 6.4.1

$$\frac{d^2c(t)}{dt^2} = -\frac{B}{m}\frac{dc(t)}{dt} - \frac{K}{m}c(t) + \frac{r(t)}{m}, \tag{6.6}$$

describing the position $c(t)$ as a function of the force $r(t)$ which is the input parameter in this case. Inserting 6.5 with $x_1(t) = c(t)$ and $x_2(t) = \dot{x}_1(t) = \dot{c}_1(t)$, yields

$$\frac{d^2c(t)}{dt^2} = \frac{dx_2(t)}{dt} = \dot{x}_2(t) = -\frac{B}{m}x_2(t) - \frac{K}{m}x_1(t) + \frac{1}{m}r(t). \tag{6.7}$$

Rearranging the above equations into a matrix form gives

$$\begin{aligned} \begin{pmatrix} \dot{x}_1 \\ \dot{x}_2 \end{pmatrix} &= \begin{bmatrix} 0 & 1 \\ -\frac{K}{m} & -\frac{B}{m} \end{bmatrix} \cdot \begin{bmatrix} x_1(t) \\ x_2(t) \end{bmatrix} + \begin{bmatrix} 0 \\ -\frac{1}{m} \end{bmatrix} \cdot r(t) && (6.8) \\ c(t) &= \begin{bmatrix} 1 & 0 \end{bmatrix} \cdot \begin{bmatrix} x_1(t) \\ x_2(t) \end{bmatrix} && (6.9) \end{aligned}$$

For the general differential equation (see e.g. [J.L96], [PH00]), the above equations can be generalised to

$$\begin{aligned} \dot{\boldsymbol{x}} &= \boldsymbol{A}\boldsymbol{x}(t) + \boldsymbol{B}\boldsymbol{r}(t), \quad \boldsymbol{x}(0) = \boldsymbol{x}_0 && (6.10) \\ \boldsymbol{c}(t) &= \boldsymbol{C}\boldsymbol{x}(t) + \boldsymbol{D}\boldsymbol{u}(t) \end{aligned}$$

One refers to equations 6.11 as the state-variable equations of a system. The first equation is called state equation, the second one output equation. The state equation is a first-order matrix differential equation whose solutions are the states $\boldsymbol{x}(t)$ of the system. Knowing $\boldsymbol{x}(t)$ and the input vector $\boldsymbol{r}(t)$, the output equation yields the output $\boldsymbol{c}(t)$. Usually the matrix $\boldsymbol{D}$ is zero, unless there is a direct connection between input and output. The description is complete, if the initial state $\boldsymbol{x}_0$ of the system is known.

$\boldsymbol{x}$: state vector of an n-th order system
$\boldsymbol{r}$: q dimensional vector composed of the system input functions
$\boldsymbol{c}$: p dimensional vector composed of the defined outputs
$\boldsymbol{A}$: (n, n) system matrix
$\boldsymbol{B}$: (n, r) input matrix
$\boldsymbol{C}$: (p, n) output matrix
$\boldsymbol{D}$: (p, r) matrix to represent direct coupling between input and output

Table 6.1.: Parameters of state and output equation

6.1.2. State space in frequency domain

For practical purposes, a better form to describe a control system is by going from state-space in time domain to state-space in frequency domain. Mathematically this means, that differential equations are formed into algebraical equations which are easier to solve. As it is always possible to expand any input signal $r(t)$ into harmonic components by using either the Laplace or the Fourier transformation, the above argumentation is also valid for any type of input signal.

Laplace transformation

The Laplace transformation offers the possibility to simplify the solution of the differential equation of the type of equation 6.2. The Laplace transform uses the complex complex angular frequency

$$s = \sigma + i\omega,$$

to change from time domain into frequency domain with the following transformation

$$F(s) = L\{f(t)\} = \int_0^\infty f(t) \cdot e^{-st}\, dt = \int_0^\infty f(t) \cdot e^{-\sigma t} \cdot e^{-i\omega t}\, dt \qquad (6.11)$$

The differentiation of a function with respect to time corresponds to a multiplication with s, while integration corresponds to a multiplication with $\frac{1}{s}$.
The Laplace transformation applied to the differential equation 6.2 yields with the initial conditions $c(t_0) = r(t_0) = 0$

$$\begin{aligned} &a_n \cdot s^n \cdot C(s) + a_{n-1} \cdot s^{n-1} \cdot C(s) + \ldots + a_1 \cdot s^1 \cdot C(s) + a_0 \cdot C(s) = \\ &b_m \cdot s^m \cdot R(s) + b_{m-1} \cdot s^{m-1} \cdot R(s) + \ldots + b_1 \cdot s^1 \cdot R(s) + b_0 \cdot R(s) \end{aligned} \qquad (6.12)$$

The system can be characterised by the "transfer function":

$$G(s) = \frac{C(s)}{R(s)} = \frac{b_m \cdot s^m + b_{m-1} \cdot s^{m-1} + \ldots + b_1 \cdot s_1 + b_0}{a_n \cdot s^n + a_{n-1} \cdot s^{n-1} + \ldots + a_1 \cdot s_1 + a_0} = \frac{P(s)}{Q(s)} \qquad (6.13)$$

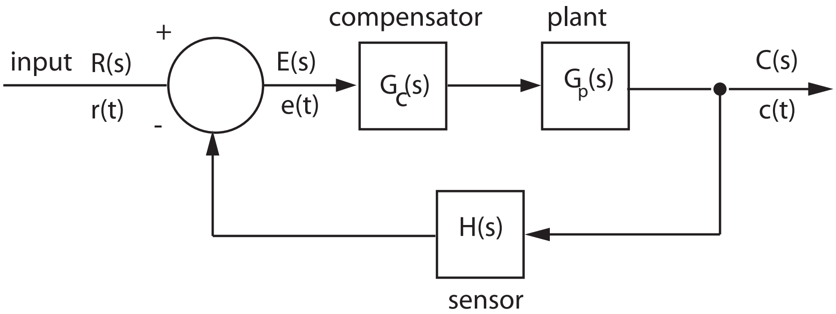

Figure 6.2.: Schematic of a single loop feedback system

So the transfer function will generally be the quotient of two polynomials. The transfer function $G(s)$ is a complex function

$$G(s) = \Re\{G(s)\} + i\Im\{G(s)\}, \tag{6.14}$$

which can be described by amplitude and phase

$$G(s) = |G(s)| \cdot e^{i\phi(s)}, \tag{6.15}$$

where

$$|G(s)| = \sqrt{(\Re\{G(s)\})^2 + (\Im\{G(s)\})^2} \tag{6.16}$$

$$\phi(s) = \arctan\left(\frac{\Im\{G(s)\}}{\Re\{G(s)\}}\right) \tag{6.17}$$

Besides using the Laplace transforms of input and output signal, one can calculate the transfer function from the state space equations 6.11 (see e.g. [J.L96]). This yields for a single-input single-output system

$$G(s) = \boldsymbol{C}(s\boldsymbol{I} - \boldsymbol{A})^{-1}\boldsymbol{B} + D, \tag{6.18}$$

where $\boldsymbol{I}$ is the unity matrix. The transfer function plays a key role in the analysis of the stability of a control system.

6.1.3. Closed-loop systems

A single-loop feedback system is depicted in figure 6.2. The plant is the physical system to be controlled. The compensator is a controller added to the loop to modify the transfer function of the complete system such that improved regulation characteristics are achieved. The output signal $C(s)$ is measured by the sensor and compared to the input $R(s)$ and the resulting error signal $E(s)$ is fed back to the plant.

The transfer function of a closed-loop system can be evaluated by using Mason's gain formula (see e.g. [PH00]).

In the case of a single loop system whose schematic is depicted in figure 6.2, the transfer function of the closed loop system is:

$$T(s) = \frac{G(s)}{1 + G(s) \cdot H(s)} \tag{6.19}$$

6.2. Stability

A linear system is called bounded-input bounded-output stable, if for every bounded input, the output remains bounded for all times. Assume a control system as shown in figure 6.2 with the transfer function 6.19. As both $G(s)$ and $H(s)$ are rational functions of s, the transfer function can be written as a fraction of polynomials $P(s)$ and $Q(s)$:

$$T(s) = \frac{P(s)}{Q(s)} \tag{6.20}$$

It is important to determine the poles of the transfer function, i.e. the zeros of the polynomial in the denominator. The *characteristic equation* is defined as the factorised polynomial $Q(s)$

$$Q(s) = a_n(s - p_1)(s - p_2)\dots(s - p_n) = 0, \tag{6.21}$$

where a_n is a constant and the p_i are the roots of the characteristic equation and thus equal to the poles of the transfer function. The input $R(s)$ may contain poles already, so one can express the output $C(s)$ in such a way, that the poles caused by the input function are collected in a separate term

$$\begin{aligned} C(s) &= T(s)R(s) = \frac{P(s)}{a_n \prod_{i=1}^{n}(s - p_i)} R(s) && (6.22) \\ &= \frac{k_1}{s - p_1} + \frac{k_2}{s - p_2} + \dots + \frac{k_n}{s - p_n} + C_r(s). && (6.23) \end{aligned}$$

$C_r(s)$ contains the terms, in the partial-fraction expansion, which originate in the poles of $R(s)$. Thus $C_r(s)$ is called the forced response of the system. Assuming that all roots p_i are different, the inverse Laplace transform of equation 6.23 yields

$$c(t) = k_1 e^{p_1 t} + k_2 e^{p_2 t} + \dots + k_n e^{p_n t} + c_r(t) = c_n(r) + c_r(t) \tag{6.24}$$

The terms of $c_n(t)$ can be called natural responses, as they originate from the transfer function and are thus characteristic for the system and not depending on the input. If the input $r(t)$ is bounded, there will be no poles originating from the input function, thus $C_r(s) = 0$. Therefore the system can become unbounded, if one or more of the natural response terms $k_i e^{p_i t}$ becomes unbounded. One of the terms $k_i e^{p_i t}$ will diverge for $t \to \infty$, if the real part of the root p_i is positive. Hence the system remains stable for any input, if all roots of the characteristic equation lie in the left half of the complex s-plane.

If the closed loop transfer function of a system is known, the *Root-Locus Analysis* is a very powerful tool to derive the system stability. The root locus analysis of a system is a plot of the movement of the poles of the closed-loop transfer function when some parameter of the system is varied, usually the loop gain. The analysis for the synchronisation will be shown in figure 6.12(a). Depicted are the poles of the transfer function in the complex plane. The path of the roots is shown as the loop gain is increased. As soon as one of the roots crossed the imaginary axis, the system becomes unbounded.

Additional information about the stability of the loop is obtained from the frequency response of the transfer function. Although the root-locus analysis does not provide a detailed knowledge about the robustness of the system, it is very important to know how the system reacts to disturbances. A convenient way to describe the frequency response of a system is by using the Bode diagram. A Bode diagram consists of two plots. Writing the transfer function in the form

$$G(i\omega) = |G(i\omega)| \cdot e^{i\phi}, \tag{6.25}$$

then

$$20 \log |G(i\omega)| \tag{6.26}$$

is the loop gain in dB. In the first plot the gain is depicted vs. frequency and in the second phase vs. frequency.

The stability criteria derived for the root-locus analysis can equivalently be found for the Bode plot. One defines the *gain margin* as the factor by which the open-loop gain of a stable system can be enhanced before the limit of stability is reached. The higher the gain margin is, the better is the robustness of the system against variation of a regulation parameter. The second stability parameter is the *phase margin*. It is defined as the phase difference to -180° when the gain crosses the 0 dB line. A large phase margin reduces the overshoot of the regulator when a step function is applied. If one manages to obtain a high open-loop gain (equivalent to a high bandwidth of the closed loop), the steady-state error is reduced (see equation 6.34). Generally it is advisable to have a large phase margin and a sufficient gain margin, so the system is robust against uncertainties in the model describing the transfer function or external disturbances.

6.2.1. Steady-state error

The synchronisation PLL (phase locked loop) is designed to operate with the error signal as the only input. At the instant when the loop is closed, the circuit will respond with a step function, namely a jump from the phase difference at $t = 0$, to zero phase difference. This signal can be written as

$$\boldsymbol{r}(t) = (\boldsymbol{R_1} - \boldsymbol{R_0})\boldsymbol{u}(t), \tag{6.27}$$

where $u(t)$ is the unit step. The amplitude of the step is proportional to the phase difference between laser and reference at $t = 0$. Consider the system depicted in figure 6.2. In our case, the transfer function of the sensor is simply a proportional gain H (see section 6.4.3). So it is possible to combine the transfer functions of sensor and compensator to form a unity gain feedback system. Using the transfer function for a single loop feedback system (equation 6.19), one finds the following expression for the output:

$$C(s) = \frac{H \cdot G_c(s)G_p(s)}{1 + H \cdot G_c(s)G_p(s)} R(s) \tag{6.28}$$

In order to define the system type, one can express $H \cdot G_c(s)G_p(s)$ as

$$H_k \cdot G_c(s)G_p(s) = \frac{F(s)}{s^N Q_1(s)}, \tag{6.29}$$

where N is the number of free integrators in the function $G_c(s)G_p(s)$. (Remembering that as the transfer function of an intergrator is proportional to $1/s$.) The system error is the difference between system input and output

$$\text{system error} = e(t) = r(t) - c(t), \tag{6.30}$$

so the *steady-state system error* e_{ss} is the steady-state value of $e(t)$. By using a theorem of the Laplace transform [PH00], one finds

$$e_{ss} = \lim_{s \to 0} sE(s). \tag{6.31}$$

For a system as shown in figure 6.2, one finds by using Mason's gain formula

$$E(s) = \frac{R(s)}{1 + H_k G_p(s) G_c(s)} \tag{6.32}$$

and

$$e_{ss} = \lim_{s \to 0} \frac{sR(s)}{1 + H_k G_p(s) G_c(s)}. \tag{6.33}$$

For a unit step function $R(s) = 1/s$, this yields

$$e_{ss} = \lim_{s\to 0} \frac{1}{1 + H_k G_c(s) G_p(s)} = \frac{1}{1 + \lim_{s\to 0} H_k G_c(s) G_p(s)} = \frac{1}{1 + K_{err}}. \quad (6.34)$$

K_{err} is called the *position error constant* and given by the limit of the open-loop transfer function of the system for $s \to 0$

$$K_{err} = \lim_{s\to 0} H_k G_c(s) G_p(s). \quad (6.35)$$

If the system has one or more free integrators, K_{err} becomes infinite and thus the steady-state error is zero. But for a system with no free integrators, there is a finite steady-state error given by equation 6.34.

In our case the amplitude of the step can be expressed by the phase difference at the time when the loop is closed. So the steady-state phase difference is

$$\phi_{err} = \frac{2\pi \left(f_{7th}^{ref} - f_{43rd}^{laser} \right)\Big|_{t=0}}{(1 + H_k G_c(s) G_p(s))\big|_{s=0}}. \quad (6.36)$$

However, as the Bode plots of the open-loop transfer function yield an open-loop gain of the circuit of $1.57 \cdot 10^3$ (see 6.11(b)), the steady-state error is negligibly small.

6.3. Time structure of the SLS linac

The time structure of the SLS proved to be a considerable challenge, as the master frequency is f_{linac} = 500 MHz which does not have any direct subharmonics around the repetition frequency of f_L = 81.25 MHz of the TiSa laser. The repetition rate can be changed by around ±500 kHz using a picomotor-driven mirror inside the cavity. One has to find a reference frequency which is an integer multiple of both the linac RF of 500 MHz and the laser repetition frequency of 81 MHz. The solution was to choose one with a small fractional relation

$$f_{common} = 3.5\ \text{GHz} = f_{linac} \cdot 7 = f_{laser} \cdot 43. \quad (6.37)$$

This means that every 7^{th} laser pulse coincides with every 43^{rd} cycle of the linac RF. For the EOS experiment it has to be made sure, that the linac gun is triggered only on every 7 laser pulse. The solution here was to synchronise the gun trigger to the TiSa laser.

6.4. Principal setup

The principal setup of the synchronisation scheme is shown in figure 6.3. A phase-locked-loop is used to synchronise the laser repetition rate to the master RF of the linac. The aim is to generate an error signal for the control of the piezo-electric mirror of the laser cavity, by using an RF mixer which generates the sum and the difference of two applied frequencies. The difference frequency is selected by an appropriate low-pass filter. This generates a dc-signal which is zero if both input frequencies are equal. The simplified schematic is shown in figure 6.4. In this section, the main components will be described and their transfer functions will be calculated.

6.4.1. The plant

The plant in the synchronisation is the laser itself. The piezo-controlled mirror detunes the repetition rate by 7.5 Hz per volt of applied voltage. At the 43^{rd} harmonic of the 81 MHz repetition frequency, the detuning is 322.5 Hz per volt (at the reference frequency of 3.5 GHz). The piezo crystal acts as an integrator for the phase difference between laser and RF in the PLL. This can be understood as follows. Assume a constant piezo voltage leading to a frequency difference of 1 Hz between 43^{rd} harmonic of the laser repetition frequency and the 7^{th} harmonic of the linac RF. Then in one second, a phase difference of 360° is accumulated. The phase difference increases linearly with time, so the response of the plant to a constant signal is a linear increase of the output signal which is typical for an integrator.

The transfer function of the plant is therefore

$$G_{piezo}(s) = \frac{k_{piezo}}{s} = \frac{32.25 \cdot 10^3 \cdot 360}{100 \cdot s} = \frac{1.164 \cdot 10^6}{s} \cdot \frac{\text{deg}}{\text{sec} \cdot \text{V}}, \tag{6.38}$$

where k_{piezo} is the plant gain.

Any piezo crystal shows mechanical resonances. These are typically at some 100 kHz. As the piezo is glued directly to a comparably heavy mirror and is fixed in a mirror mount, the resonance frequency diminishes to $f_{res} = 5.5$ kHz. The transfer function can be modelled by a dampened harmonic oscillator. As coarse estimate, we assume a quality factor between 10 and 100, which yields a damping coefficient of $\gamma = (0.1 \ldots 0.01) \cdot \omega_{res}$. The result for the transfer function of the resonance is:

$$G_{res}(s) = \frac{\omega_{res}^2}{s^2 + \gamma\omega_{res} \cdot s + \omega_{res}^2} \tag{6.39}$$

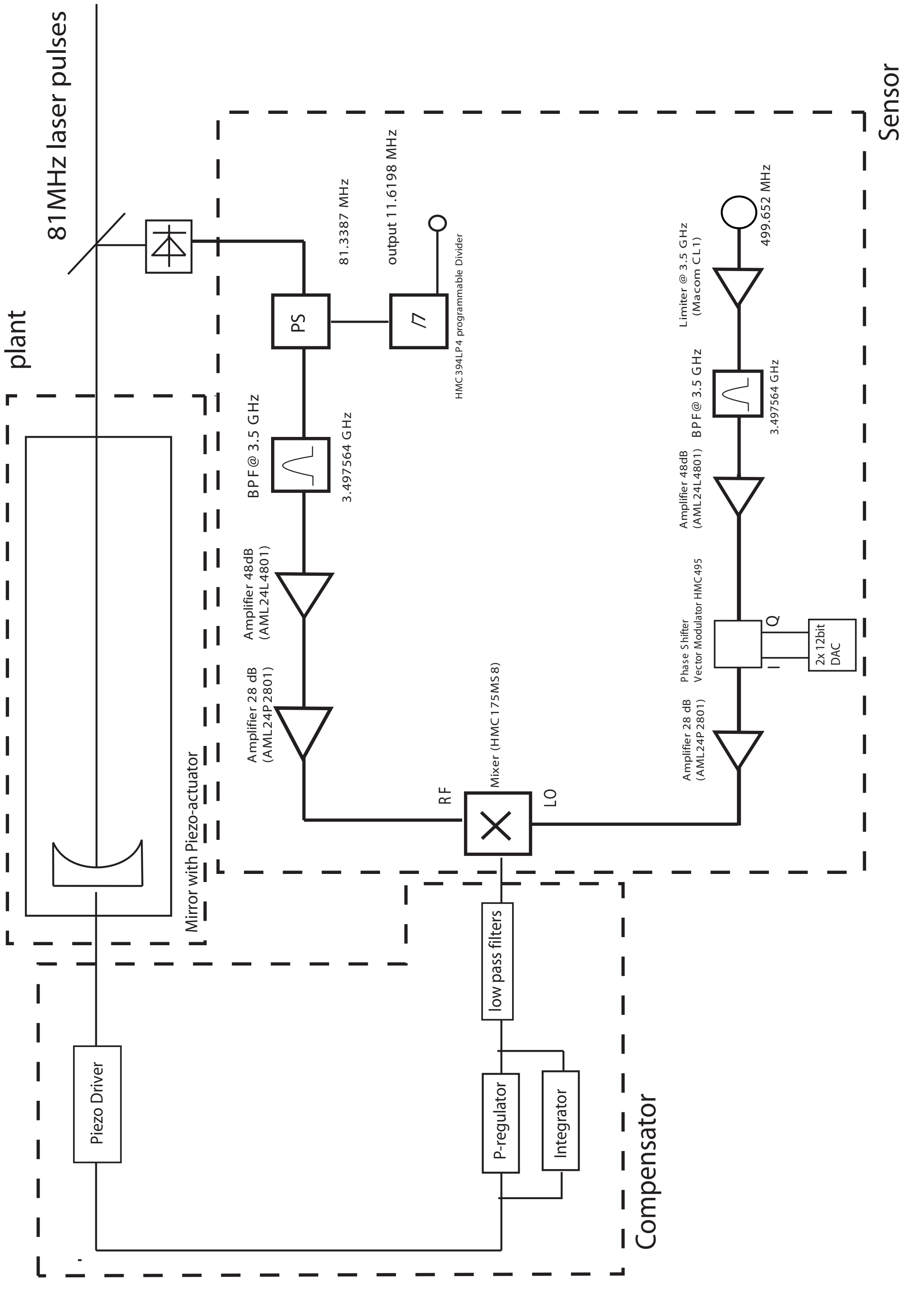

Figure 6.3.: General layout of the synchronisation controller

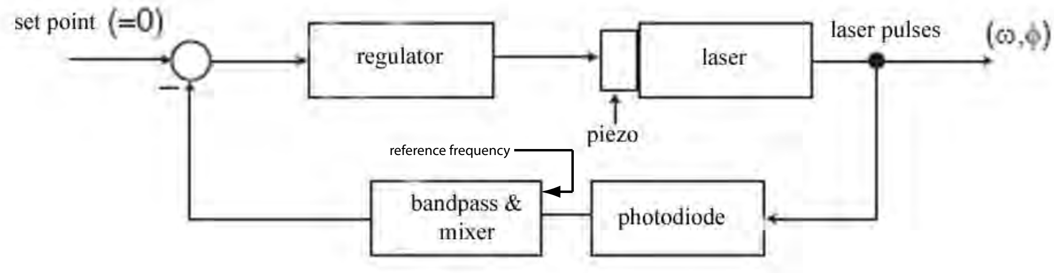

Figure 6.4.: Coarse schematic of the laser synchronisation

So the complete transfer function of the plant is:

$$G_{piezo}(s) = \frac{k_{piezo}}{s} = \frac{32.25 \cdot 10^3 \cdot 360}{100 \cdot s} = \frac{1.164 \cdot 10^6}{s} \cdot \frac{\text{deg}}{\text{sec} \cdot \text{V}} \tag{6.40}$$

6.4.2. The compensator

In order to get an error signal with a set-point of zero, one has to use an integrator. The integrator amplifies lower frequencies more than higher ones and continues to do so until the input becomes zero. A high gain at low frequencies is advantageous, as for example ground motion occurs at very low frequencies of up to some 10 Hz. The natural limit to the integrator gain is the operational amplifier used. Usually their open loop maximum gain is technically limited at around 120 dB.

To improve the suppression of perturbations in the laser repetition rate, the error signal is amplified with an adjustable proportional gain of $k_p = 0.5, 1, 2, 3, 4, 5$. To minimise distortions, the gain and time constant are selected in our design via a digital switch. That way, only a digital signal is transmitted from the switch, located at the front panel of the unit, to the PI-regulator board which is shielded by a small box inside the synchronisation unit. Thus analogue noise is avoided. The integrator gains are $k_i = 13740, 6230, 2832, 1374, 623, 283, 137$. The schematic of the PI controller is shown in appendix B.

The regulator has as a parallel proportional and integral part and a second-order low-pass filter with a cutoff frequency of $\omega_{lp} = 82.8\,\frac{1}{\text{sec}}$ and a piezo driver with a fixed gain of 20 in series. The transfer function for the PI-regulator is:

$$G_{PI}(s) = k_p + \frac{k_i}{s} = \frac{k_p \cdot s + k_i}{s} \tag{6.41}$$

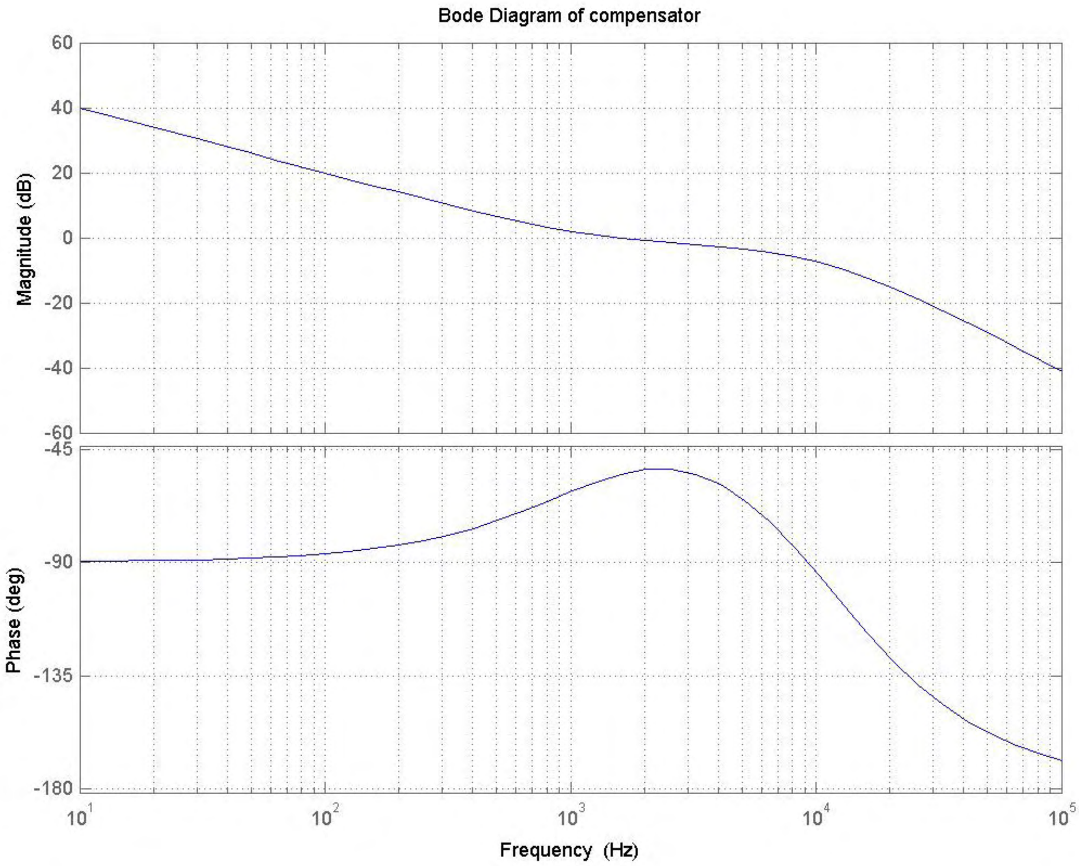

Figure 6.5.: Bode plot of the PI regulator and the second-order low-pass filter

The second-order passive low-pass filter, has the following transfer function:

$$G_{lp}(s) = \frac{1}{(1 + \omega_{lp} \cdot s)^2} \tag{6.42}$$

Thus the transfer function of the compensator is:

$$G_c(s) = 20 \cdot G_{lp}(s) \cdot G_{PI}(s) = \frac{20 \cdot (k_p \cdot s + k_i)}{s \cdot (1 + \omega_{lp} \cdot s)^2} \tag{6.43}$$

A Bode plot of the transfer function is shown in figure 6.5.

6.4.3. The sensor

The task of the sensor is to generate an error signal by comparing the frequency and phase of the laser repetition rate to a reference, which is the central SLS RF of 500 MHz. A schematic is shown in figure 6.3.

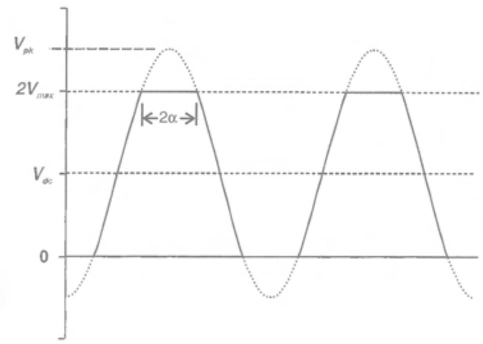

Figure 6.6.: Input and output signal of a limiter amplifier from [Cri99]

Treatment of the master RF signal

This section treats the bottom branch of the sensor depicted in figure 6.3. The prime goal has to be to generate a phase-stable 7th harmonic of the 500 MHz linac RF. This is achieved by using a voltage driven limiter amplifier (MACOM CL1). The input and output signal of a limiter are shown in figure 6.6. The amplifier can follow the input signal up to an amplitude V_{max}, given by an external limiting voltage applied to the amplifier. The larger the clipping angle α is, the more the output signal resembles a square wave.

These types of amplifiers are commonly used to remove amplitude perturbations. The limiting process causes the generation of odd harmonics of the signal frequency. The lower the limiting level is, the higher is the output power in the odd harmonics. The signal consists now of the input frequency at 500 MHz and its odd harmonics.

There are some drawbacks of creating odd harmonics by a an overdriven amplifier. Firstly the phase noise of the master signal is amplified by the same factor as the frequency is multiplied. This cannot be measured by the noise on the error signal but contributes to the total jitter budget. Secondly this method is not very effective in terms of signal level. With an input level of around 3 dbm at 500 MHz, the output behind the limiter is around -55 dbm at 3.5 GHz. Therefore, the signal has to be amplified by at least 60 dB, and using such a large gain reduces the signal quality through AM-PM (amplitude modulation to phase modulation) conversion. The magnitude of AM-PM conversion depends on the type of amplifier and it is not yet clear how much the amplifiers used in the system contribute to the jitter of $\sigma t = 40fs$. The alternative is to use a PLL and generate the signal by locking a VCO (Voltage Controlled Oscillator). This scheme is more complicated and the effort to reach the stability of an overdriven amplifier using a good master oscillator is considerable.

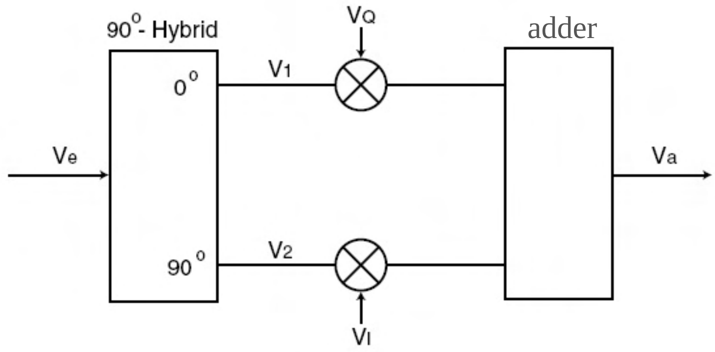

Figure 6.7.: Principle of a vector modulator

As shown in figure 6.3, the signal then passes a bandpass filter with a bandwidth of 1% relative to the center frequency of 3.5 GHz. Due to the small bandwidth, all other harmonics are attenuated by at least 80 dB.

The signal is then transferred to a vector modulator, which is used to generate an externally controllable phase shift.

The vector modulator

The basic layout of a vector modulator is shown in figure 6.7. The RF signal is split by a 90° hybrid, which introduces a fixed 90° phase shift onto one channel. Through the IF ports of the two mixers (commonly referred to as I and Q ports), an external signal is multiplied with the RF input signal. Then both channels are added using a power combiner. Let the input signal be:

$$|\tilde{V}_e| \quad \text{with} \quad \tilde{V}_e = A \cdot e^{i\omega t} \tag{6.44}$$

It will be split up into:

$$V_1 = \frac{1}{\sqrt{2}}\tilde{V}_e \quad \text{and} \quad V_2 = \frac{i}{\sqrt{2}}\tilde{V}_e \tag{6.45}$$

One applying to the I and Q ports a dc signal of V_I respectively V_Q. These voltages will cause the mixers to change the transmission ratio of the according RF. The level is given by the ratio of $\frac{V_{I,Q}}{V_{ref}}$. V_{ref} depends on the actual vector modulator used and is usually in the order of 1 V. The RF voltages are then summed in the adder:

$$V_{out} = \frac{\tilde{V}_e}{\sqrt{2}}(\frac{V_I}{V_{ref}} + i\frac{V_Q}{V_{ref}}) \tag{6.46}$$

So the output signal is shifted against the input signal by

$$\phi = \arctan\left(\frac{V_Q}{V_I}\right). \tag{6.47}$$

One can therefore shift the phase of the output relative to the input signal by applying suitable voltages to the I and Q port. This gives the possibility to shift the phase of the laser relative to the linac RF. Generally, only a phase shift of 360° is possible. However the phase advances needed for the EOS experiment are larger than 360°. Assume that a phase advance of a certain value is programmed into the vector modulator. This causes the error signal to increase from zero to a constant value, which in turn moves the piezo and thus changes the repetition frequency of the laser. Hence the phase difference between laser and linac RF will start to change as the piezo acts as a phase shift integrator. Thus it is possible to shift the phase by more than 360°, as long the magnitude of each shift does not exceed 180° and the system has a chance to adapt to the change. The settling time to a step function is around 3 ms for a 2% range. (see figure 6.12(b))

A possibility to test the quality of the device is to apply a well known modulation (e.g. a circle in the complex plane) and compare amplitude and phase of output and input signal. For an ideal device, the output RF should show the exact pattern applied to I and Q. To demonstrate this, a sinusoidal signal with f_I=1 kHz is applied to I and a sinusoidal signal with f_Q=1 kHz and $\Delta\phi = 90°$ is applied to Q. The amplitude of the sinusoidal signal is in this case chosen to enable maximum transmission.

A constant reference frequency of 3.5 GHz is supplied to the input of the device. A network analyser measures the amplitude and phase of the modulated RF signal relative to the reference. The scanning rate is set to 1 kHz, so one should see a perfect circle, where the radius represents the relative level of the output RF signal to the reference. The result is shown in 6.8. The missing part of the circle is due to a slightly smaller repetition rate than 1 kHz. The radius of the circle is

$$r = \sqrt{\Re\left(\frac{V_{out}}{V_e}\right)^2 + \Im\left(\frac{V_{out}}{V_e}\right)^2}. \tag{6.48}$$

Evaluation of the data of figure 6.8 yields:

$$r = 0.4362 \pm 0.00177 \tag{6.49}$$

The radius is normalised to the amplitude of the reference input signal. Thus the device shows an insertion loss of around 7db, where some of the loss occurs in the connecting cables (approx. 2db). The amplitude stability is excellent,

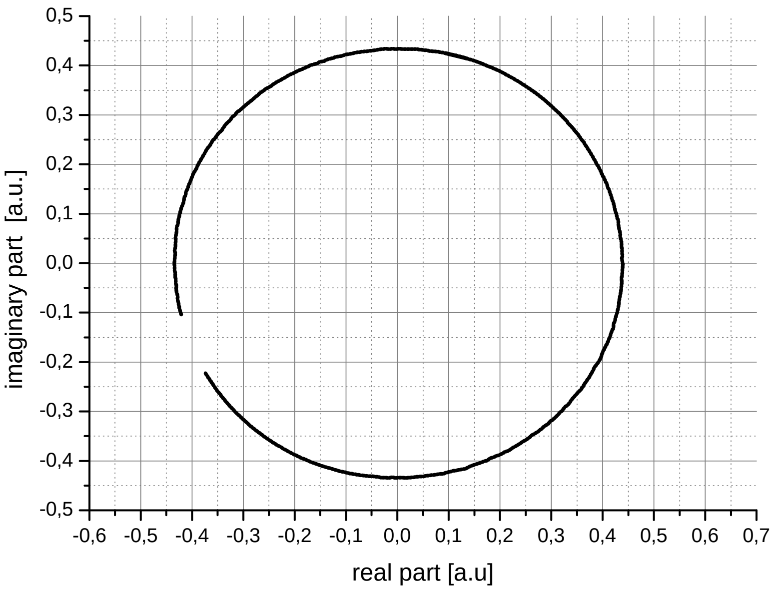

Figure 6.8.: Real and imaginary parts of the measured output signal of the vector modulator relative to the input signal (3.5 GHz sine wave).

of the order of $5 \cdot 10^{-3}$. The linearity of the device is extremely important for the EOS measurements. If the amplitude of the 3.5 GHz signal changes during the course of a measurement, the calibration voltage (voltage per degree phase shift) changes and with that the conversion factor of phase-to-freqeuncy of the mixer changes (see section 6.4.3). This has a negative effect on the stability of the synchronisation circuit.

Stability issues

One important prerequisite to achieve a high accuracy of the circuit is the stability of the voltages applied to the vector modulator. Any ripple here has immediate effect on the 3.5 GHz RF signal, as amplitude and phase are modified by the vector modulator. The voltages are generated by two digital-analog-converters (DAC's) from a CAMAC crate with a MATLAB program. The resolution and output voltage stability of the DAC outputs was sufficient to be able to scan with a phase shift of 0.1° per step. In the experiment planned at DESY, one has to achieve a stepwidth of 0.02°. This sets a high demand in terms of voltage stability. Therefore, in the advanced version planned for the synchronisation at DESY, the generation of the voltages will be done inside the synchronisation unit using fibre optics to supply the digital signals from a VME crate to the DAC to minimise potential pick up of noise in the cables.

Treatment of the laser pulses

Part of the laser beam is directed onto a fast photo diode with a bandwidth of 12 GHz via a beam splitter. This signal is fed into the synchronisation unit. A power splitter divides the signal into one part used to generate the timing signal for the linac trigger and another to generate the 3.5 GHz reference frequency, using a bandpass (1% bandwidth) which selects the 43^{rd} harmonic of the laser repetition rate. The small bandwidth of the bandpass is very important, to attenuate the 42^{nd} and 44^{th} harmonic as much as possible. An 8^{th} order bandpass was chosen with a rolloff of 100 dB per decade. The output at 3.5 GHz has a very low level (around -55 dbm) and is amplified by 65 dB and fed to the RF port of the mixer.

The timing trigger signal

The modifications to the gun trigger of the SLS Linac required the generation of a phase stable signal with $f_{gun} = f_{Laser}/7 = 11.65$ MHz. The gun trigger is generated synchronous to the 11.65 MHz, hence the gun is only triggered when a laser pulse is present at a predefined position relative to the linac RF.

The 81 MHz "needle" pulses of the photodiode are converted to a 81 MHz sinusoidal wave by a low-pass filter. This is necessary, as otherwise the programmable divider receives too much power on its input. The laser fundamental is amplified by 16 dB and fed to a programmable divider (set to divide-by-7). Another driving stage supplies the necessary gain to make the signal acceptable to the TTL type SLS trigger generator.

The mixer

A mixer may be considered a three-port component. There are two input ports, the received signal (RF) and the local oscillator (LO) port. The output is the intermediate frequency (IF) port. The mixer delivers two signals, the sum frequency and the difference frequency of the two inputs. In practice, only one of these is selected via a high-pass or a low-pass as the desired signal.In our case, a double balanced mixer is used, which will be described in the following.
One approach to a double balanced mixer is the ring mixer (see figure 6.4.3). The circuit consists of a ring of four diodes, labelled D1 through D4 and two transformers T1 and T2. The secondary windings of these transformers are connected to the nodes of the diode ring, labelled A through D.

The operation of the mixer can be described by treating the diodes as ideal LO-driven switches. That means the diodes are opened using the signal level of the LO input. The possible output level is the LO-level minus the level the

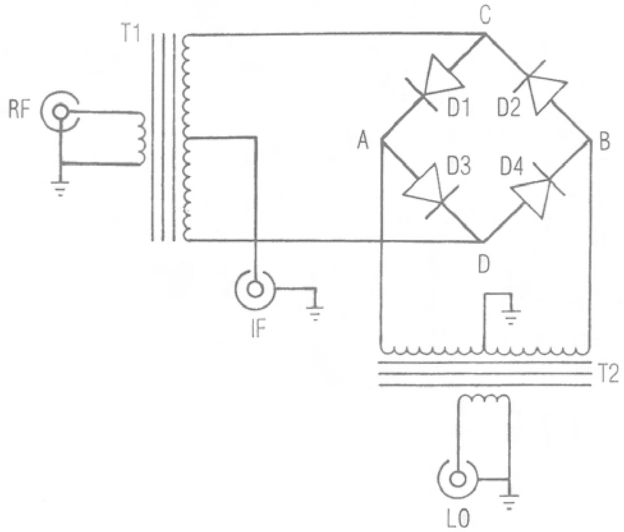

Figure 6.9.: Schematic view of a double balanced mixer from [Maa88], where RF = $f_{TiSa} \cdot 43$ and LO = $f_{linac} \cdot 7$

signal looses in the mixer, called insertion loss.

Let the polarity of the LO voltage be such that the right side of the secondary winding of T2 is positive, so diodes D1 and D2 are turned on and D3 and D4 are turned off. During this half of the LO cycle, D1 and D2 short-circuit T2, so that node C is connected to ground via the center tap of T2. The upper half of T1 is thus connected to through these diodes to the IF port, and the RF port is momentarily connected to the IF port. When the LO voltage reverses, D3 and D4 are turned on and D1 and D2 are turned off. Then the lower half of T1 is connected to the IF, so the RF is again connected to the IF but with reversed polarity. The mixer therefore acts as a polarity reversing switch, connecting the RF port to the IF but reversing its polarity every half LO cycle.

In our case a double balanced high LO mixer, requiring an LO-level of +15 dbm compared to the common level of 7 dbm to operate from Hittite was used (HMC 175MS8). A high LO mixer has the benefit of a higher output level. To eliminate any spurious outputs, a low-pass filter with a cutoff frequency of 30 MHz was installed.

Transfer function of the sensor

The mixer is in our case a phase-difference-to-voltage converter. In the unlocked state, meaning that the laser repetition rate and the linac RF are not synchronous, the output is a sinusoidal signal such as shown in figure 6.10. The amplitude of

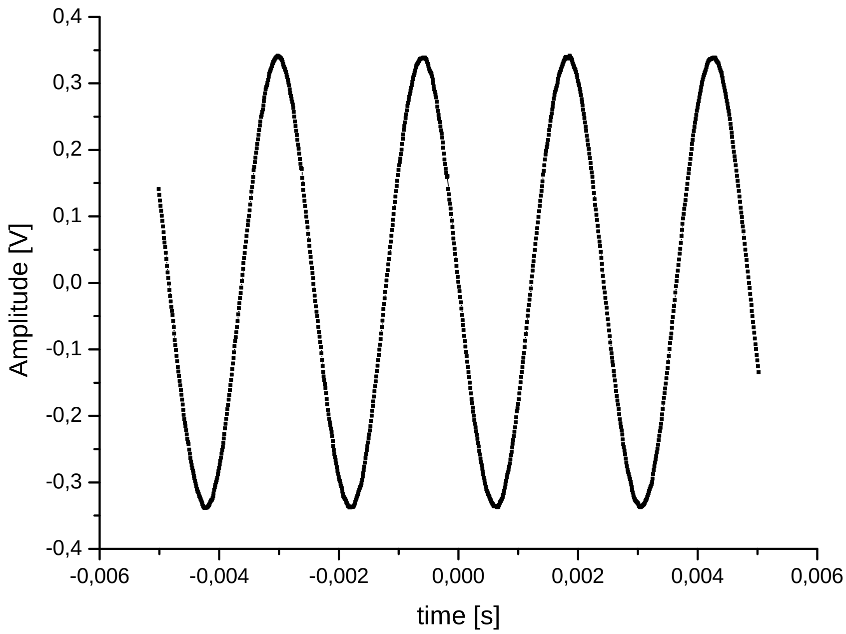

Figure 6.10.: Mixer output signal with no feedback to the piezo mirror applied

the sinusoidal wave can be measured to $V_{max} = 341$ mV which corresponds to an rms value of 241 mV. This amplitude is a characteristic of the regulation and does not change if the amplitude of both 3.5 GHz signals at the mixer inputs remain constant. In the locked state, the phase error will be jittering around zero, thus one can linearise the sinus in a narrow range around the zero crossing. A good approximation of the non-linearity of the sinus is to take the rms value of the amplitude for a phase advance of 45°. Hence the resolution of the mixer is given by

$$V_{res} = 5.81 \cdot \frac{\mathrm{mV}}{\mathrm{deg}}. \tag{6.50}$$

The mixer acts like a fixed-gain amplifier. So its transfer function is

$$G_s(s) = 5.81 \frac{\mathrm{mV}}{\mathrm{deg}}. \tag{6.51}$$

A Bode plot of the sensor and plant transfer function is shown in figure 6.11(a).

6.5. Transfer function of the complete system

The open-loop transfer function can now be evaluated by multiplying the transfer functions of the various subsystems:

$$
\begin{aligned}
G_c(s) &= 20 \cdot G_{lp}(s) \cdot G_{PI}(s) = \frac{20 \cdot (k_p \cdot s + k_i)}{s \cdot (1 + \omega_{lp} \cdot s)^2} \\
G_p(s) &= \frac{k_{piezo}}{s} = \frac{32.25 \cdot 10^3 \cdot 360}{100 \cdot s} = \frac{1.164 \cdot 10^6}{s} \cdot \frac{\mathrm{deg}}{\mathrm{sec} \cdot \mathrm{V}} \\
G_{res}(s) &= \frac{k_{piezo}\, \omega_{res}^2}{s^3 + \gamma\, \omega_{res} \cdot s^2 + \omega_{res}^2 \cdot s} \\
G_s(s) &= 5.81 \cdot 10^{-3}\, \frac{\mathrm{V}}{\mathrm{deg}}
\end{aligned}
$$

This yields :

$$
G_{ol}(s) = G_p(s) \cdot G_c(s) \cdot G_s \cdot G_{res}(s) = \frac{107.2 \cdot (k_{piezo}\, \omega_{res}^2 k_p \cdot s + k_{piezo}\, \omega_{res}^2 k_i)}{\omega_{lp}^2 s^6 + 2\omega_{lp}(2\omega_{lp}\gamma\omega_{res} + 1)s^5 + (\omega_{lp}^2\omega_{res}^2 + 2\omega_{lp}\gamma\omega_{res} + 1)s^4 + (2\omega_{lp}\omega_{res}^2 + \gamma\omega_{res})s^3} \tag{6.52}
$$

Figure 6.11(b) shows the effect of the integrator in the compensator at low frequencies (the gain increases significantly). It would be desirable to shift the point of unity gain to higher frequencies in order to also suppress perturbations occurring at higher frequencies. In the present system however, this is prevented by the eigenresonance at 5.5 kHz of the piezo controlled mirror in the laser resonator. This limits the point of unity gain to 1.57 kHz.

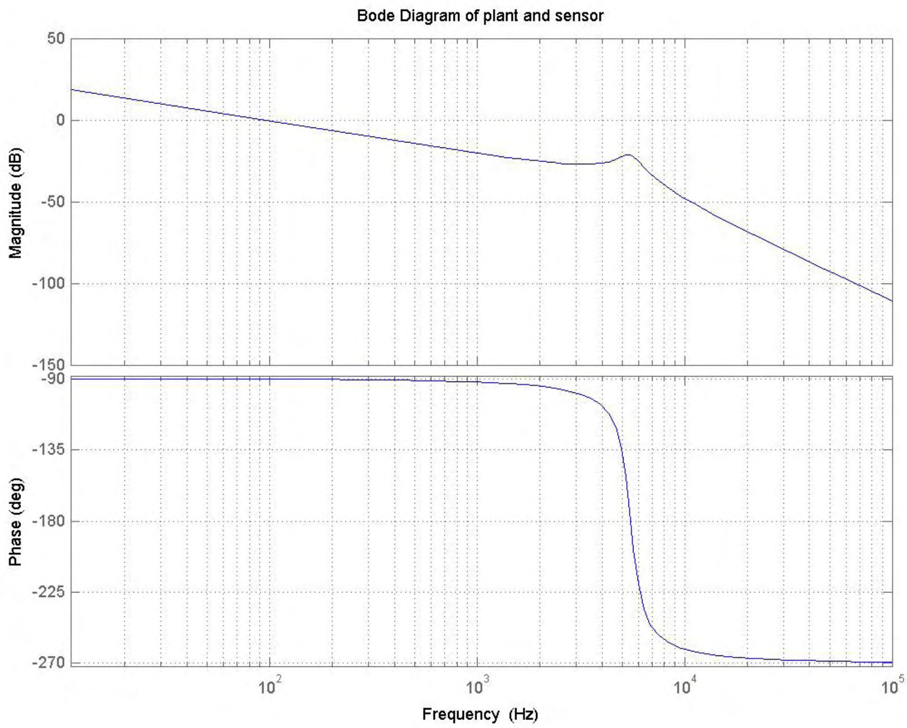

(a) Bode plot of the combined transfer functions of sensor and plant

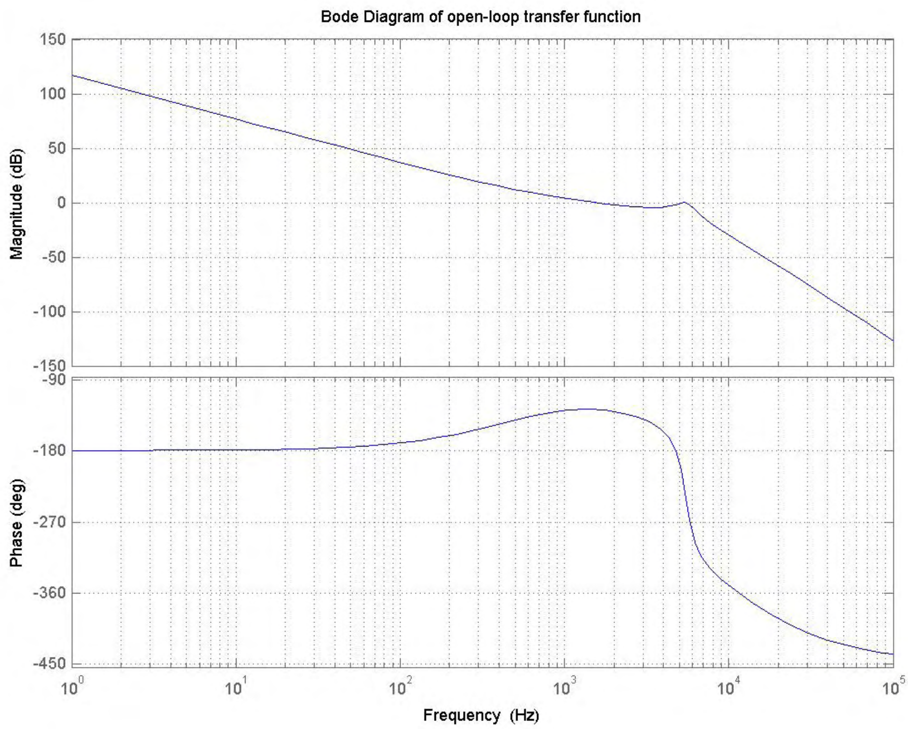

(b) Bode plot of the complete open-loop transfer function of the system

Figure 6.11.: Bode plots of different transfer functions of components of the controller

6.6. Long term stability

As with most electronics, the long term stability is mostly dominated by the temperature coefficients of the parts used. One most critical issues is the offset drift of the mixer. A double balanced mixer has an offset drift of around 2 mV/°C. That means if the temperature inside the synchronisation box changes by 1°C during a measurement, there will be a drift between laser repetition rate and linac RF of

$$\sigma t = 793 \frac{\mathrm{fs}}{\mathrm{deg}} \cdot \frac{1}{5.1} \frac{\mathrm{deg}}{\mathrm{mV}} \cdot 2\mathrm{mV} = 310\,\mathrm{fs}, \tag{6.53}$$

which is the time per degree of phase of the 3.5 GHz RF multiplied by the resolution of the mixer (see equation 6.50). Therefore a temperature stabilisation of the whole setup is required. This is accomplished by a temperature regulator in the supply box, keeping the temperature stable with $\Delta T < 0.1$°C. The added jitter to the long term jitter budget by the mixer will therefore be around 30 fs. The temperature coefficients of other components such as operational amplifiers are in the range of some ppm. So compared to the mixer offset-drift, they are of negligible influence.

6.7. Stability measurements

6.7.1. Simulation

In order to understand the limits of the synchronisation unit and to evaluate the maximal values for the gains of the compensator, a simulation using the Root-Locus analysis is required. MATLAB offers the possibility to simulate a single loop circuit with the *rltool* from the Control Tool Box. The roots of the characteristic equation (see section 6.2) are calculated and the varied parameter is the loop gain. That corresponds to a variation of the Piezo driver gain in our setup. The result is shown in figure 6.12(a). One can see a few stability relevant issues from the open loop bode plot on the right hand side. The gain and phase margins are given. The phase margin of 26° qualifies for a rather robust controller, but the gain margin of less than 2db shows that the regulator is at the edge of the stability regime. Any increase is loop gain makes the system unstable. This point of instability is the resonance of the piezo crystal at 5.5 kHz. This is also evident when looking at the response to a step function (see figure 6.12(b)). After a settling time of 3 ms, the controller has adapted to the step command within a 2% range, but with a rather large oscillation modulated onto the signal while adapting. Because the regulation has the maximum gain possible, these oscillations cannot be avoided.

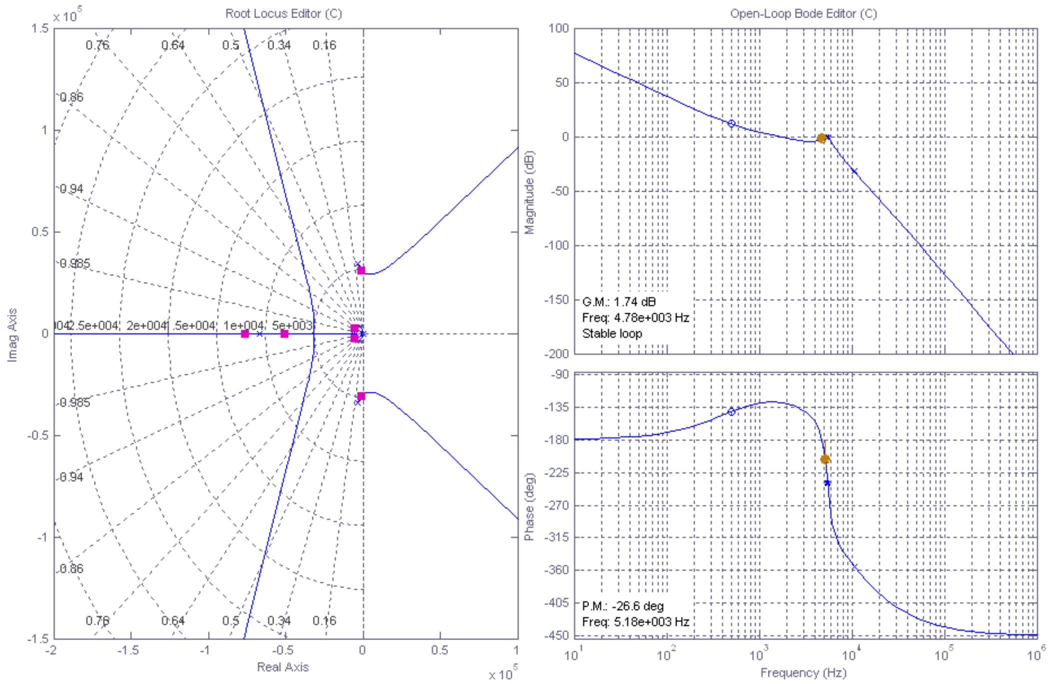

(a) Root locus and open-loop Bode plot

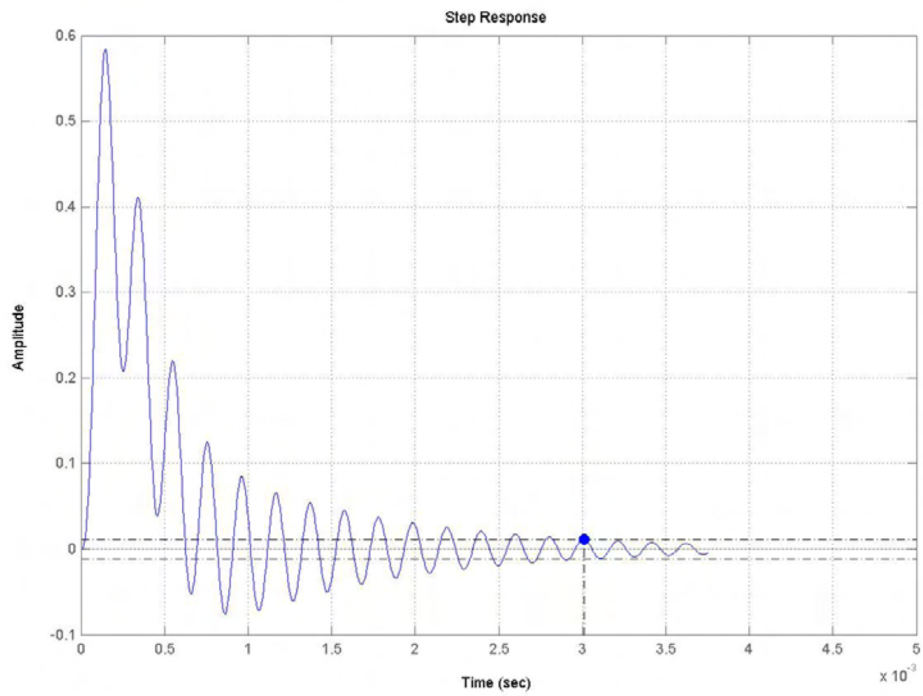

(b) Response of the system to a step input function

Figure 6.12.: Characteristics of the synchronisation scheme.

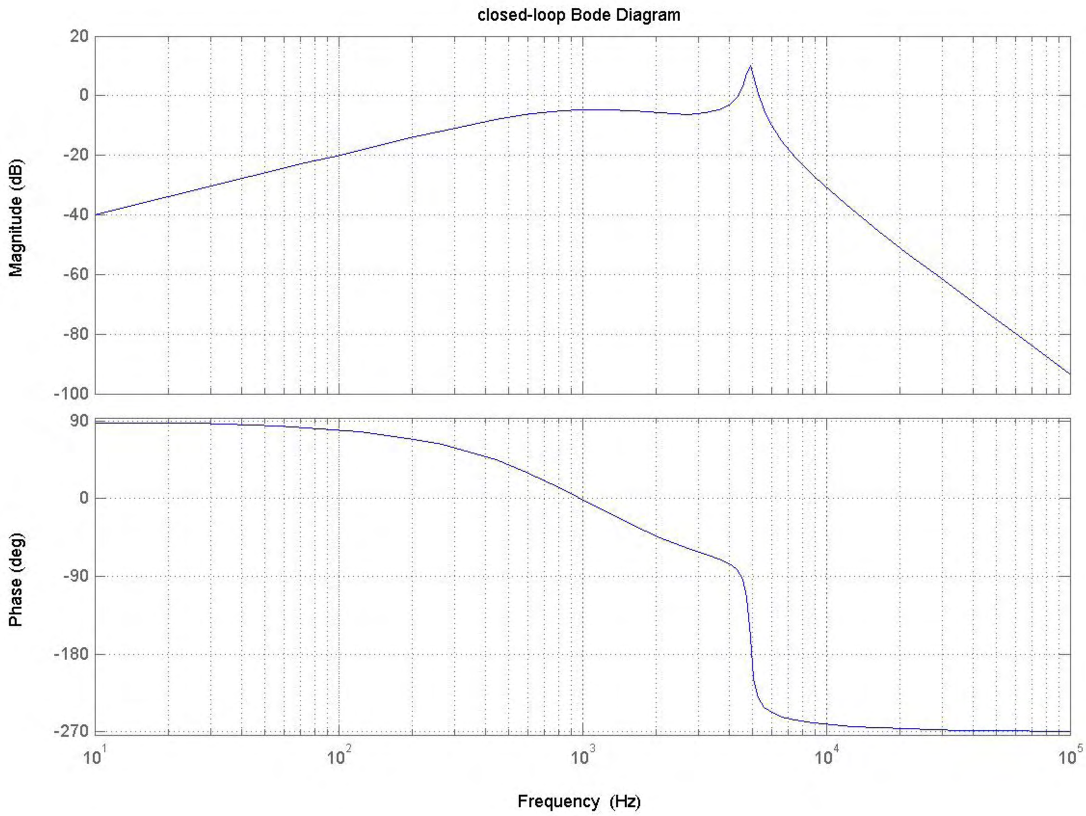

Figure 6.13.: Closed-loop Bode plot

6.7.2. Measurements at the SLS

The accuracy of the synchronisation of the laser repetition rate to the linac RF can be measured real-time by looking at the error signal at the mixer output without opening the loop (e.g. by a $1\,\mathrm{M}\Omega$ scope). The rms voltage jitter measured can be converted into a timing jitter. The degree-to-time conversion for a frequency of 3.5 GHz yields

$$1^\circ \hat{=} \frac{1}{360 \cdot 3.5 \cdot 10^9} = 793\,\mathrm{fs}. \tag{6.54}$$

The sensitivity of the mixer is given by equation 6.51, so one can derive

$$1\,\mathrm{fs} \hat{=} \frac{5.81\,\frac{\mathrm{mV}}{\mathrm{deg}}}{793} = 7.34\,\mu\mathrm{V} \tag{6.55}$$

As the expected stability is below the 100 fs level, a Stanford Research low-noise preamplifier with a gain of 100 and a low-pass filter at 100 kHz was used to boost the signal to evade the limiting noise floor of the oscilloscope of around 120 μ V. The low-pass eliminates any disturbance above the measuring bandwidth. Some typical measurements are shown in figure 6.14.

Measurements in time domain

Measurements in time domain with the oscilloscope provide the possibility to obtain information about the stability of the scheme, but without any knowledge about the spectral distribution of the noise. One can derive an rms error from the time domain graphs, which can be calculated for the examples in figure 6.14 to

$$V_1 = 286\,\mu\mathrm{V} \quad \text{and} \quad V_2 = 253\mu\mathrm{V}. \tag{6.56}$$

Using the conversion factor from equation 6.55 this yields a rms stability of the synchronisation for figure 6.14(a) of

$$\sigma t = \frac{V_1}{7.34\,\frac{\mu\mathrm{V}}{\mathrm{fs}}} = 39\,\mathrm{fs}. \tag{6.57}$$

In the case of figure 6.14(b) the result is

$$\sigma t = \frac{V_2}{7.34\,\frac{\mu\mathrm{V}}{\mathrm{fs}}} = 34.5\,\mathrm{fs}. \tag{6.58}$$

This analysis however only covers a short time, as the memory depth of the scope is limited and does not contain any information about the frequency dependency of the jitter. A better way to measure the accuracy is using a signal analyzer. This is a spectrum analyzer with a limited bandwidth (102.6 kHz) but a very high dynamic range and a low noise floor.

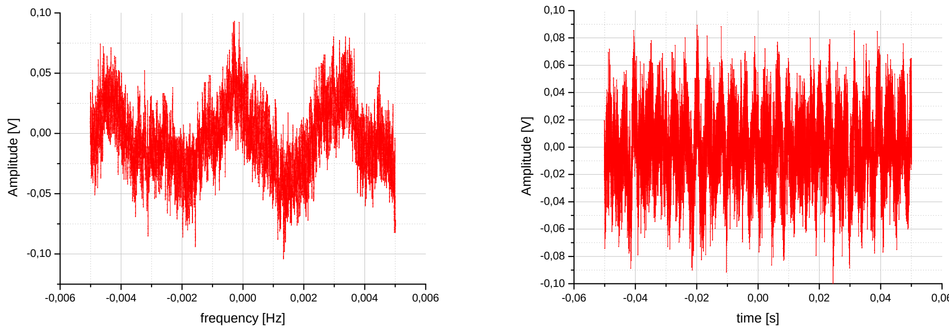

Figure 6.14.: Two examples of the error signal measured in time domain (amplification factor 100) where $1.34\,\mu\mathrm{V} \equiv 1\,\mathrm{fs}$

Measurements in frequency domain

Frequency resolved measurements of the error signal offer the possibility to obtain information about the noise sources. For the measurements, a Dynamic Signal Analyzer was used. The bandwidth of the analyzer is 106 kHz, but only measurements with 1600 points at a time are possible. As the changes are slow, it is possible to split the measured frequency interval to obtain a higher resolution. As the most interesting part of the spectrum is below 20 kHz, data were taken with 1600 points from 0.5 Hz to 100 Hz, 100 Hz to 1600 Hz, 1600 Hz to 25600 Hz and 25600 Hz to 106000 Hz. The plots are shown in figures 6.15 and 6.7.2. Depicted is the power spectral density, so the power in units of V^2 per Hz at a 50 Ω input. To obtain the total noise on the error signal, one has to integrate over the frequency and take the square root. For frequencies from 0.5 Hz up to 106.4 kHz, the result for this measurement is:

$$V_{noise} = 253.7\,\mu\mathrm{V} \quad \text{at a sensitivity of} \quad 7.34\,\frac{\mu\mathrm{V}}{\mathrm{fs}} \tag{6.59}$$

which yields an rms accuracy of

$$\sigma t = 34.6\,\mathrm{fs}. \tag{6.60}$$

This result agrees very well with the rms jitter derived from the time domain measurement of 6.14(b).

The measured accuracy is in this case between laser and RF and does not account for the phase noise of the RF signal. Other effects leading to a jitter between electron bunch arrival time at the experimental station and the laser pulse arrival time as e.g. gun jitter are not included either.

To show the influence of ground motion, a high precision measurement of the error signal in the frequency range of 0.5 Hz to 25 Hz has been conducted. The

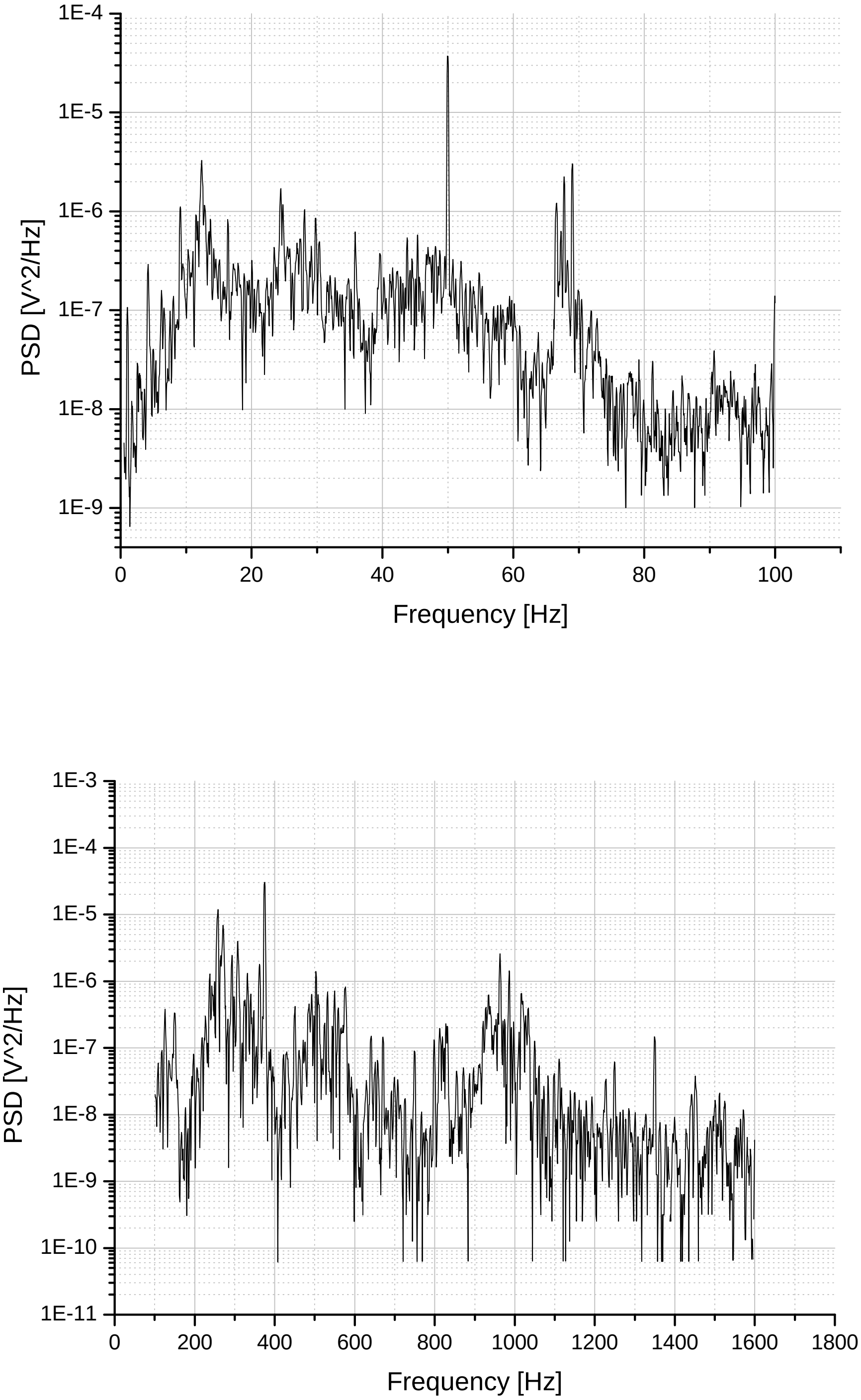

Figure 6.15.: Noise spectra of the closed loop error signal up to 1.6 kHz. Depicted is the power spectral density vs. frequency.

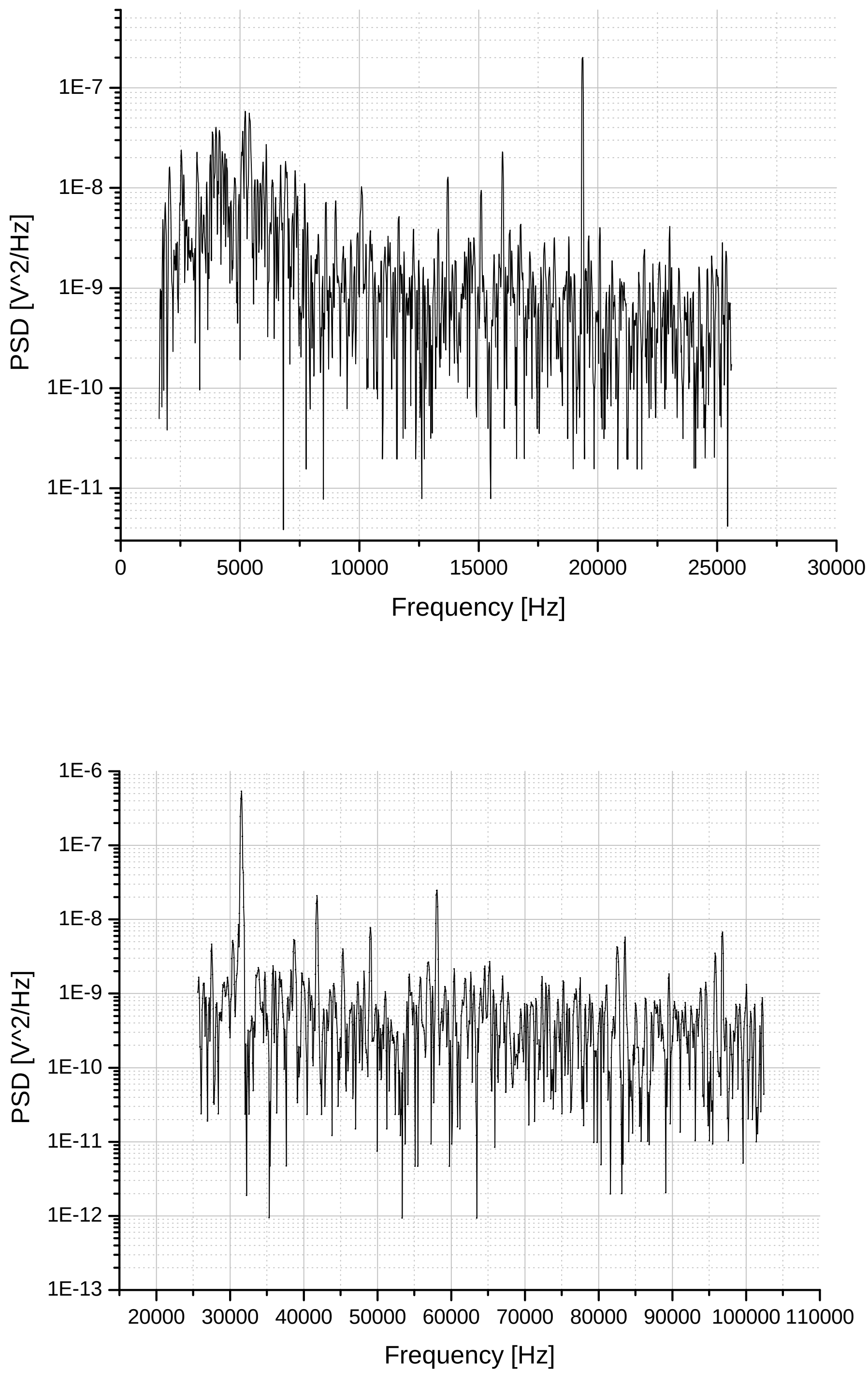

Figure 6.16.: Noise spectra of the closed loop error signal up to 106 kHz. Depicted is the power spectral density vs. frequency.

result is compared with the seismic measurements from section 5.3. The result is shown in figure 6.17. One can see very nicely that seismic spectrum is modulated onto the error signal (e.g. the peaks at 6.5 Hz and 16 Hz). The linear reduction of signal level at low frequencies is due to the use of the integrator which suppresses low frequencies best (see e.g. the closed-loop transfer function in figure 6.12(a)). The type of vibrational dampers and the integrator gain proved to be very well adapted to each other. The vibrational dampers show a mechanical resonance at about 6 Hz, which is significantly suppressed due to the high gain of the integrator at that frequency. The integrator gain drops below unity gain at 20 Hz where the attenuation of ground noise because of the dampers is significant.

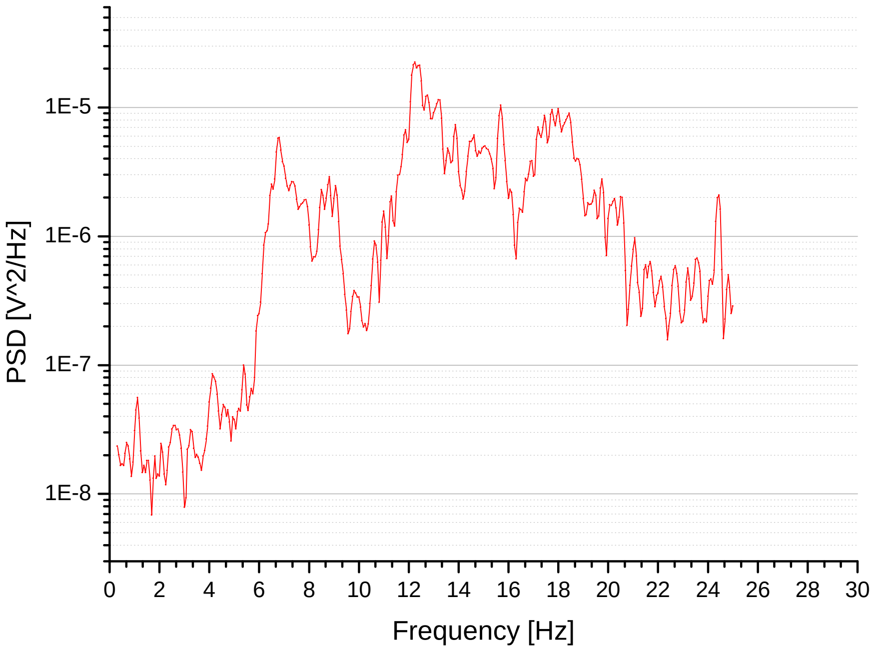

(a) Error signal spectrum up to 25 Hz

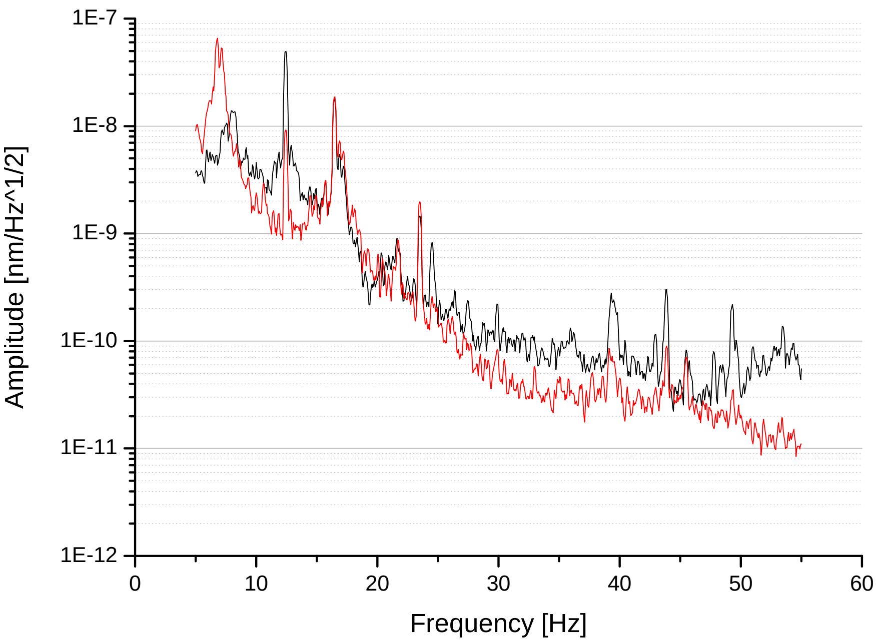

(b) Seismic spectrum

Figure 6.17.: Noise spectra of the closed loop error signal. Depicted are power spectral density vs. frequency.

6.8. Limits and improvements

As one can see from the open loop transfer function in figure 6.12(a), the proportional gain cannot be increased anymore. With a unity gain at 1.5 kHz, disturbances at higher frequencies are not suppressed at all. The main limit is the mechanical piezo resonance at 5.5 kHz. There are two possibilities to circumvent that problem. Firstly, one can employ a digital regulation with a steep digital notch filter at the resonance frequency and increase the loop gain to about 40 (see figure 6.18).

Secondly, one can modify the laser mirror mount inside the laser by a different attachment system of the mirror onto the piezo. If a very light mirror is attached to the piezo using a special wax, the total mass of the piezo system will be much lower than presently. The resonance frequency will move close to the natural eigenresonance of the peizo stack at some 100 kHz. With a resonance only at such a high frequency, it is possible to increase the open-loop gain by a factor of 40. Thus the point of unity gain increases and perturbations of higher frequencies can be suppressed.

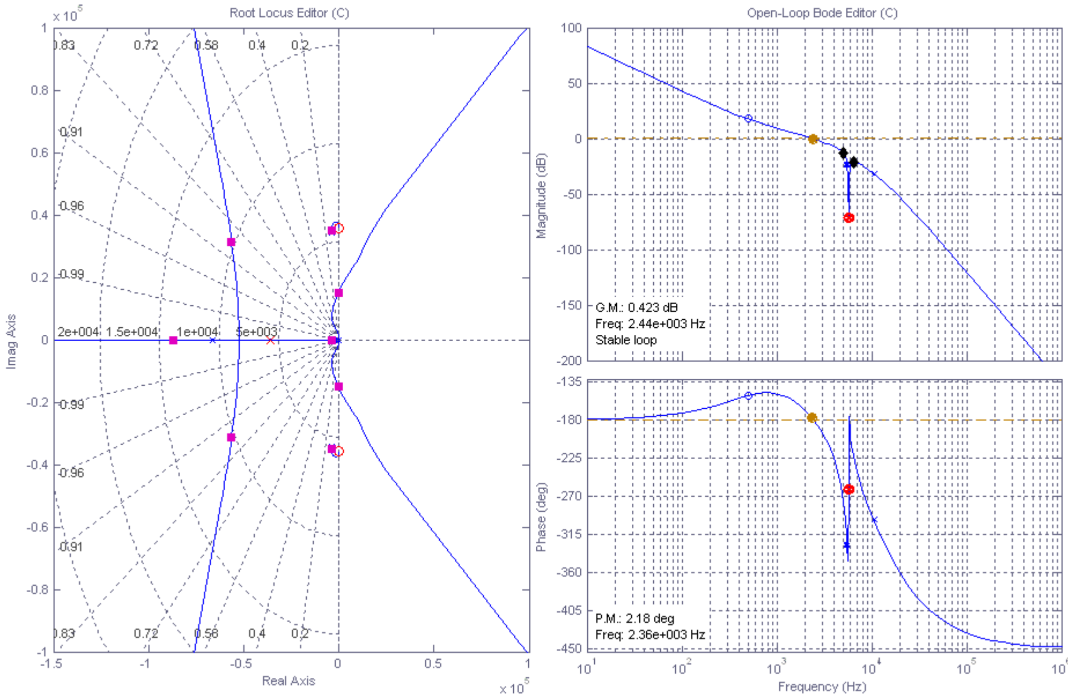

Figure 6.18.: Open loop Bode diagram of the regulation with a notch filter at the resonance frequency

7. Bunch length measurements

7.1. Simulation of the beam propagation from CTR screen to the ZnTe crystal

For coherent transition radiation (CTR) with a frequency of some hundred GHz, conventional ray optics cannot be used anymore to determine the focal point of the image. Instead, the program ZEMAX was used to calculate the transfer function of the paraboloid mirrors and the effects aperture of the vacuum chamber window. The program is based on near field propagation of the electric field amplitude and was used to obtain the size of the focal spot of the CTR at the ZnTe crystal and its frequency dependence. A schematic model of the optics is shown in figure 7.1.

ZEMAX calculates the propagation of the transition radiation emitted from an infinitely short electron bunch at the source (CTR screen) to the observation plane while taking into account the effects of the finite screen size, the aperture of the vacuum window and the diameter of the two parabolic mirrors. The window is made from fused quartz, which has a uniform transmission characteristic for radiation up to 500 GHz. It transmits around 90% of the radiation with a negligible frequency dependency. It could thus be left out of the simulation of the radiation propagation. According to calculations done by D. Sütterlin [Sue04], the influence of the 45° inclination angle between the diffraction radiation screen and the electron bunch is only significant at frequencies well below 100 GHz. These however are strongly suppressed in the EOS setup due to diffraction effects.

Because of the finite OTR screen diameter of 57 mm and near field diffraction,

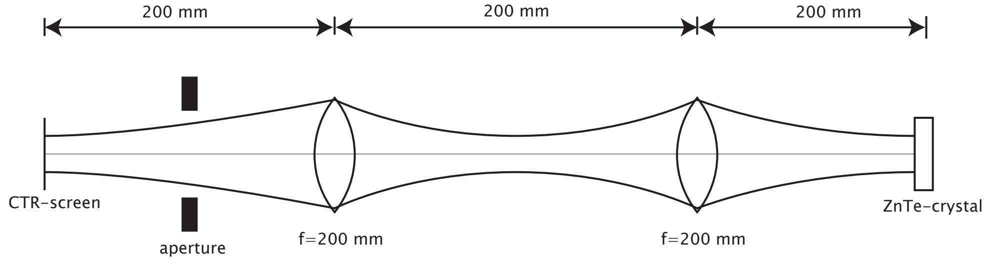

Figure 7.1.: Schematic of the beam transfer from CTR screen to ZnTe crystal

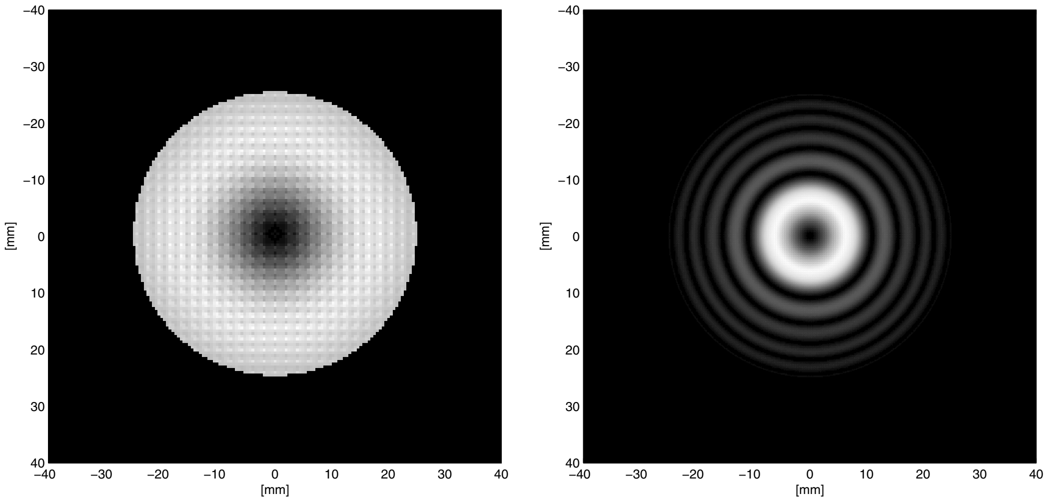

Figure 7.2.: Left: Transmission of 30 GHz CTR radiation through the aperture of the vacuum window; Right: Transmission of 500 GHz CTR radiation through the aperture of the vacuum window

the opening angle of the CTR depends strongly on the frequency and grows considerably towards lower frequencies. In this section, only the limiting effects due to the optics will be discussed. The aperture of the vacuum window will cut off frequencies below 30 GHz, see figure 7.2. The calculations were done for an electron beam of 0.1 mm transversal radius and a Lorentz factor of $\gamma = 200$.

7.1.1. CTR transfer function

The spot size of the focused CTR beam varies strongly with frequency. High frequencies can be focused better onto a small spot size than lower ones. Thus the size of the laser spot on the ZnTe crystal plays a significant role, because this determines the effective target size. Thus the laser spot acts as a high pass filter.

The TiSa laser operates in the TEM-00 mode, and therefore can be well described by a two-dimensional Gaussian distribution with a width of $\sigma = 2$ mm at the position of the ZnTe crystal. The spatial intensity distribution of the laser pulse and the CTR radiation ($f = 500$ GHz) on the ZnTe crystal is shown in figure 7.3(d). Even though the maximum of the laser spot coincides with the destructive interference pattern of the CTR radiation, there is still sufficient overlap at frequencies above 80 GHz to obtain a polarisation change of the laser beam due to the electro-optic effect of the ZnTe crystal. The overlap gets significantly smaller for lower frequencies, as shown in figure 7.3(b) for a frequency of 75 GHz.

The 2d Gaussian model of the laser spot is convoluted with the intensity distribution of the CTR radiation. Simulations for various frequencies yield the transfer function shown in figure 7.4. The errors are due to numerical uncertainties. The curve can be approximated by an exponential function with a frequency offset of the form

$$y(f) = 1 - \exp(-\frac{f - f_0}{k}) \quad \text{with} \quad k = 282.8 \text{ and } f_0 = 38\,\text{GHz}. \tag{7.1}$$

The CTR radiation passes through air between the vacuum window and the crystal. Water vapor in humid air has absorption lines at frequencies around 500 GHz. Even though the Fourier components of the CTR radiation emitted from the bunch are not very high at 500 GHz, the effect in nonetheless taken into account in the fitted CTR transfer function from figure 7.4. An exponential decay of the CTR radiation was assumed for frequencies above 1 THz, as the transmission of the quartz window used suppresses frequencies above 1 THz. The result is shown in figure 7.5.

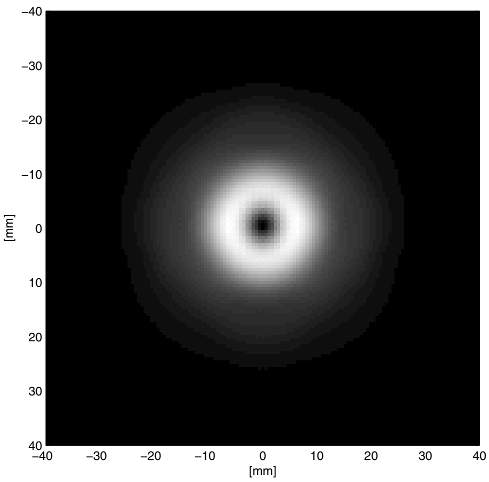

(a) 2d intensity plot of the CTR radiation on the crystal

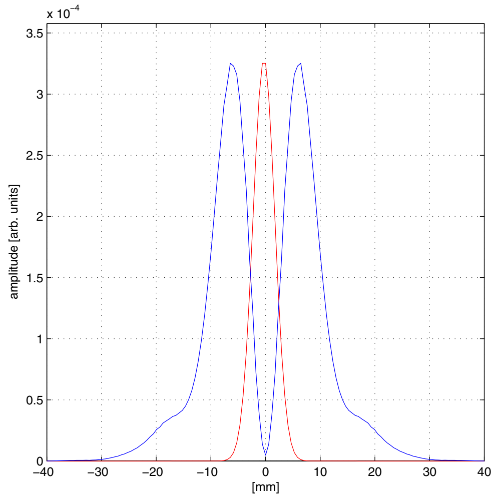

(b) Intensity plot of CTR radiation and laser spot on the x-axis of the crystal

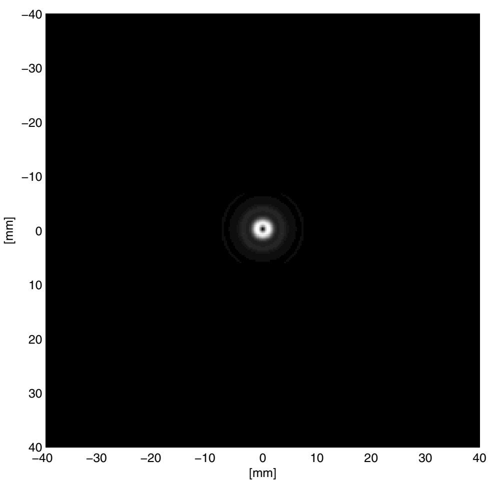

(c) 2d intensity plot of the CTR radiation on the crystal

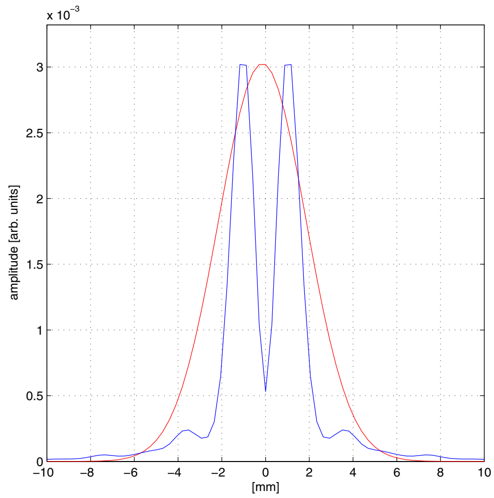

(d) Intensity plot of CTR radiation and laser spot on the x-axis of the crystal (scale adjusted)

Figure 7.3.: CTR intensity distribution at the crystal for frequencies of 75 GHz (a and b) and 500 GHz (c and d)

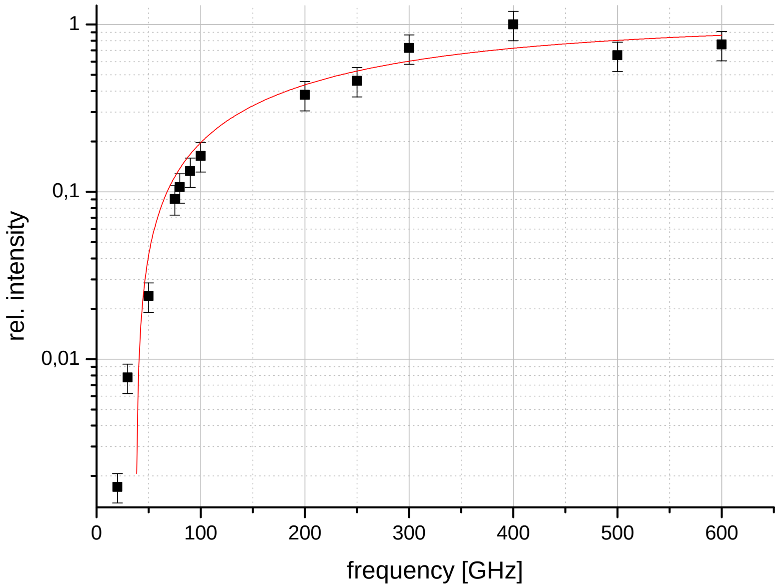

Figure 7.4.: Computed transfer function for the CTR radiation from the CTR screen to the ZnTe crystal convoluted with the 2d Gaussian model of the TiSa laser beam intensity at the crystal.

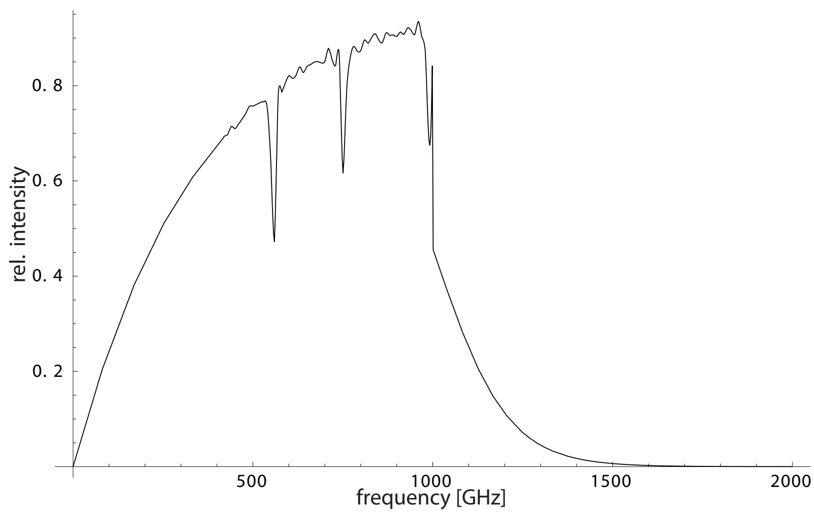

Figure 7.5.: Transfer function for CTR radiation from the CTR screen to the ZnTe crystal, convoluted with the laser beam profile at the crystal. The water resonances are also included.

7.2. Measurements

7.2.1. Coarse timing

Once the TiSa laser has been synchronised to the linac RF, every 7^{th} laser pulse is at the same position relative to the 500 MHz RF wave (see section 6.3). The signal of the photomultiplier (see figure 5.6), receiving part of the laser beam and the optical transition radiation, is observed with a high bandwidth scope. The optical components are aligned in such a way that the optical path lengths of the CTR radiation and of the laser pulse are identical. If laser pulse and CTR pulse are coincident on the photomultiplier, then they are coincident on the ZnTe crystal as well within the resolution of the photomultiplier of 0.5 ns. To find the electro-optic signal, the delay between CTR pulse and laser pulse was shifted with a step width of 1 ps until a change in the output signal of the balanced detector was observed. Once the electro-optic signal is found, a time window of ± 15 ps is scanned with a step width of 200 fs.

The Camac crate is equipped with two DACs to set the phase difference between linac RF and TiSa laser repetition rate in the vector modulator. A screen shot of a typical coincidence event with an electro-optical signal is shown in figure 7.7. The top trace shows the signal of the timing photomultiplier. OTR radiation and laser pulse overlap at the central large peak. The centre trace shows the balanced diode detector signal. The balanced detector should ideally only show a signal if an electro-optic effect in the ZnTe crystal occurs. The pellicle beamsplitter however, does not perfectly conserve the initial linear laser polarisation beam, but introduces a small circular component. Thus it is in our case not possible to balance the detector perfectly using the quarter wave plate, and the neighbouring TiSa pulses can be observed. The larger amplitude of the central pulse is caused by the electro-optic effect in the ZnTe crystal, as CTR radiation and laser pulse coincide. The bottom trace shows the linac trigger.

7.2.2. Adjustment of crystal and laser spot position

A Golay cell is mounted on a motor driven sled together with the ZnTe crystal. The Golay cell has a circular input window (diameter: 3 mm) and is sensitive to frequencies from 30 GHz up to some THz. Scans were conducted to find the optimal position of the CTR focus and thus for the centre of the ZnTe crystal. The result is shown in figure 7.6. The expected central minimum due to the diffraction effects was not observed. This can be understood taking into account the size of the window of the Golay cell and the high bandwidth of the cell which causes an average over a broad frequency range.

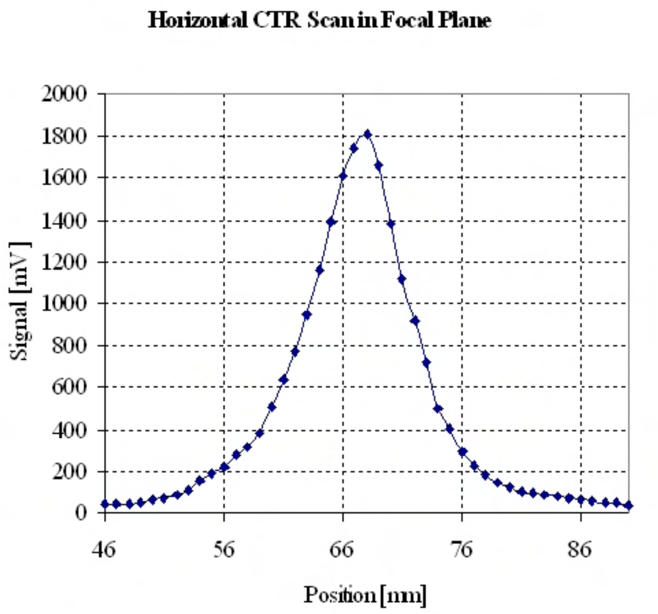

Figure 7.6.: Scan with Golay cell to find the optimal focal point of the CTR radiation [SSSJ03]

7.2.3. Data aquisition

The data acquisition was done using a high bandwidth digital oscilloscope, which offered the possibility to store the 4 traces of the oscilloscope into the internal memory of the scope, triggered by the linac trigger and later save these onto the local hard disk of the oscilloscope. The memory buffer was large enough to save several thousand triggered events.

Several measurement series were conducted at varying machine parameters to obtain different bunch lengths. The bunch length can be changed by altering the amplitude of the prebuncher and the phase the buncher (see section 5.1.2). The measurements shown were taken with the parameters shown in table 7.1.

Some results are shown in figure 7.8. The balanced detector signal is integrated over the width of the peak; 10 individual measurements at each time step are averaged.

One observes a peak of several picosecond width with undershoots at the front and rear end. The undershoots are caused by the suppression of low frequencies of the CTR signal, due diffraction effects (see section 7.1). The following methods were employed to reconstruct the bunch shape from this signal.

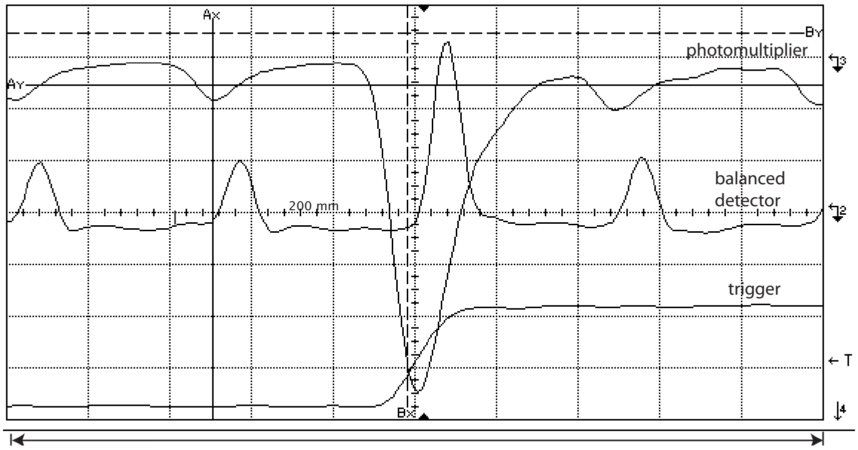

Figure 7.7.: Oscilloscope screenshot with electro-optic signal. Top trace: Signal of the timing photomultiplier with laser pulses; Center trace: Signal of the balanced diode detector; Bottom trace: Linac trigger

number of bunches in bunch train	1
bunch charge	0.6 nC
max. variation of prebuncher amplitude	6 kW
max. variation of subharmonic prebuncher phase	3 °
step width	200 fs
stepping window	32 ps
averages per phase step	10
laser polarisation	horizontal
CTR polarisation	horizontal
crystal thickness	1 mm

Table 7.1.: Linac parameter during EOS measurements

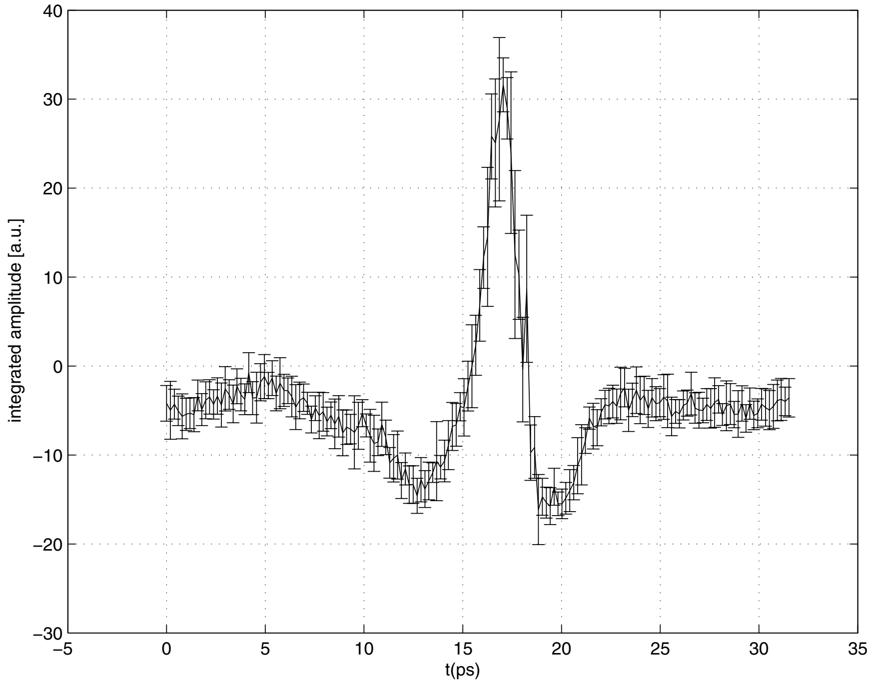

(a) Measurement A (prebuncher amplitude: 390 kW)

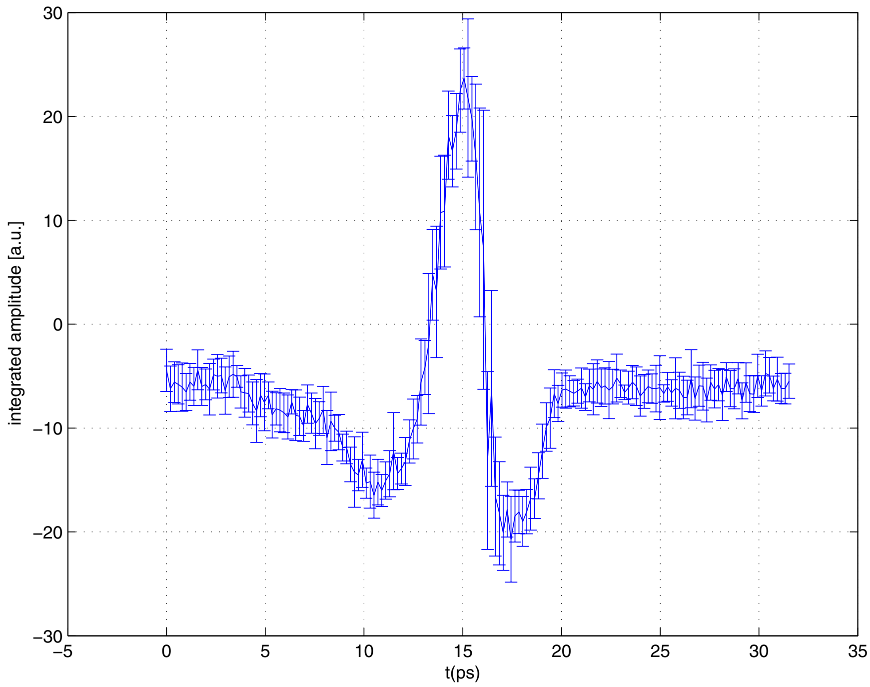

(b) Measurement B (prebuncher amplitude: 384 kW)

Figure 7.8.: Depicted is the integrated signal from the balanced receiver versus delay between TiSa laser pulse and electron bunch.

7.3. Determination of the longitudinal bunch profile

The data analysis proceeds as follows. Starting from a variety of bunch shapes in time domain, a Fourier analysis is done. Then the transfer function derived in section 7.1.1 is applied. The resulting frequency spectrum is transformed back into time domain and compared to the measured signal. Then the χ^2 of the function in minimised with the *NMinimise* routine from Mathematica.

The first approach would be using a single Gaussian peak with variable amplitude and sigma. This does not describe the measured signal very well, as the different amplitudes of the undershoots cannot be described using only a single Gaussian distribution.

Two Gaussian distribution model

Now, two Gaussian distributions with variable amplitude, centre position and sigma are assumed. The results of the fits for the two measurements from figure 7.8 are shown in figure 7.9 and 7.10, the fitparameters in table 7.2.

	meas. A	meas. B
A_1	797	530
σ_1 [ps]	1.11	1.34
t_1 [ps]	16.82	13.94
A_2	173	424
σ_2 [ps]	0.91	0.97
t_2 [ps]	14.65	15.33
$\Delta_{1-2}t[ps]$	2.17	1.39

Table 7.2.: Fit parameters for a superposition of two Gaussian distributions

The fit suggest as a pulse form an asymmetric Gaussian pulse. The fit with two Gaussian distributions suggests a pulse length (FWHM) of

$$\tau_A = 3.0\,\mathrm{ps} \quad \text{respectively} \quad \tau_B = 3.5\,\mathrm{ps}. \tag{7.2}$$

Considering the various uncertainties in the calculation of the transfer function for the CTR radiation, this is in good agreement with the expected bunch lengths of the SLS linac (FWHM) of $\tau_{SLS} = 3\,\mathrm{ps} \ldots 5\,\mathrm{ps}$. However another bunch shape leading to a smaller χ^2 will be described in the following section.

Three Gaussian distribution model

The fit is improved, when three Gaussian distributions with variable amplitude, sigma and center position are used. Plots similar to figure 7.9 and 7.10 are shown

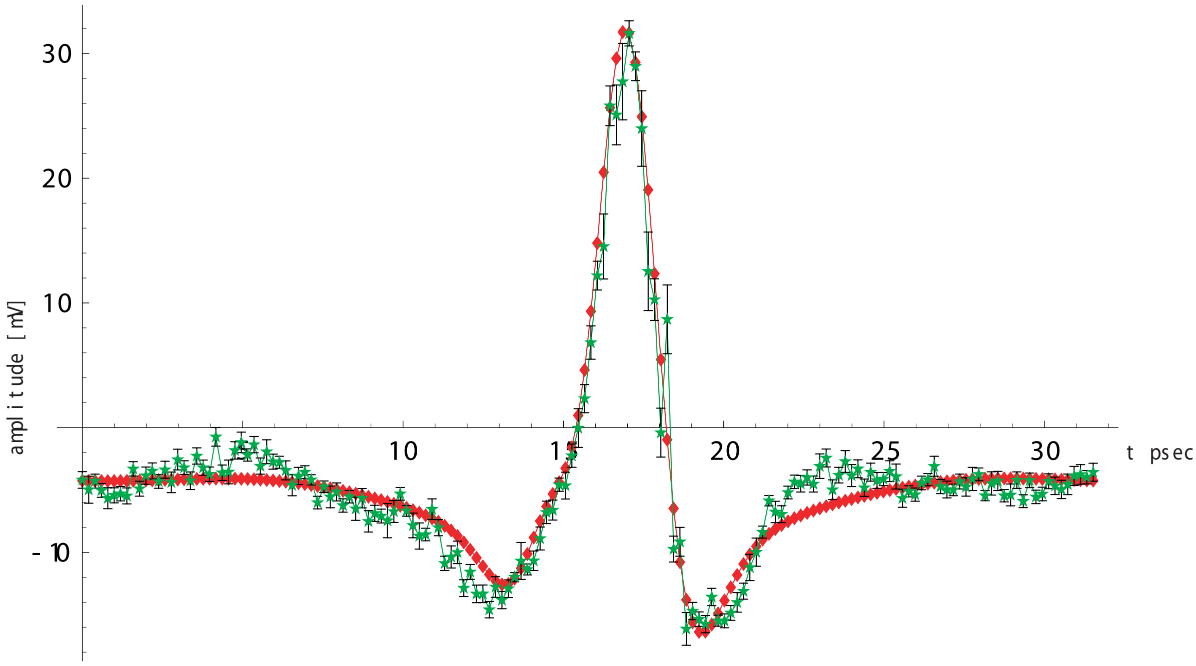

(a) Fit using 2 Gaussian distributions

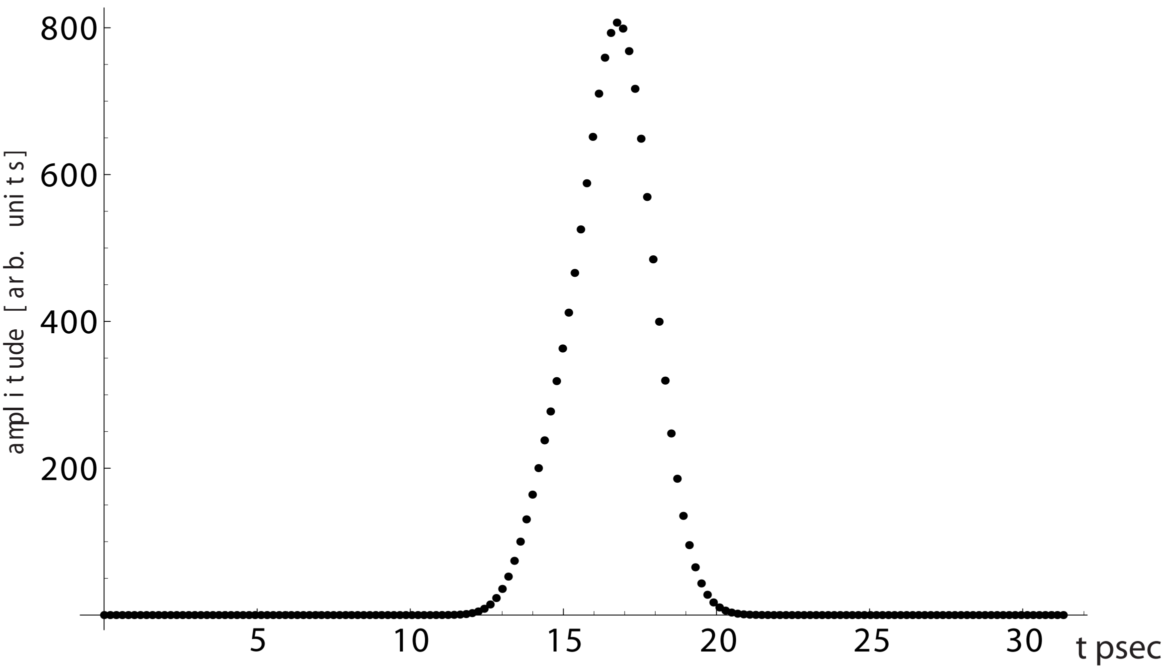

(b) Reconstructed pulse shape

Figure 7.9.: Fit results with 2 Gaussian model for measurement A

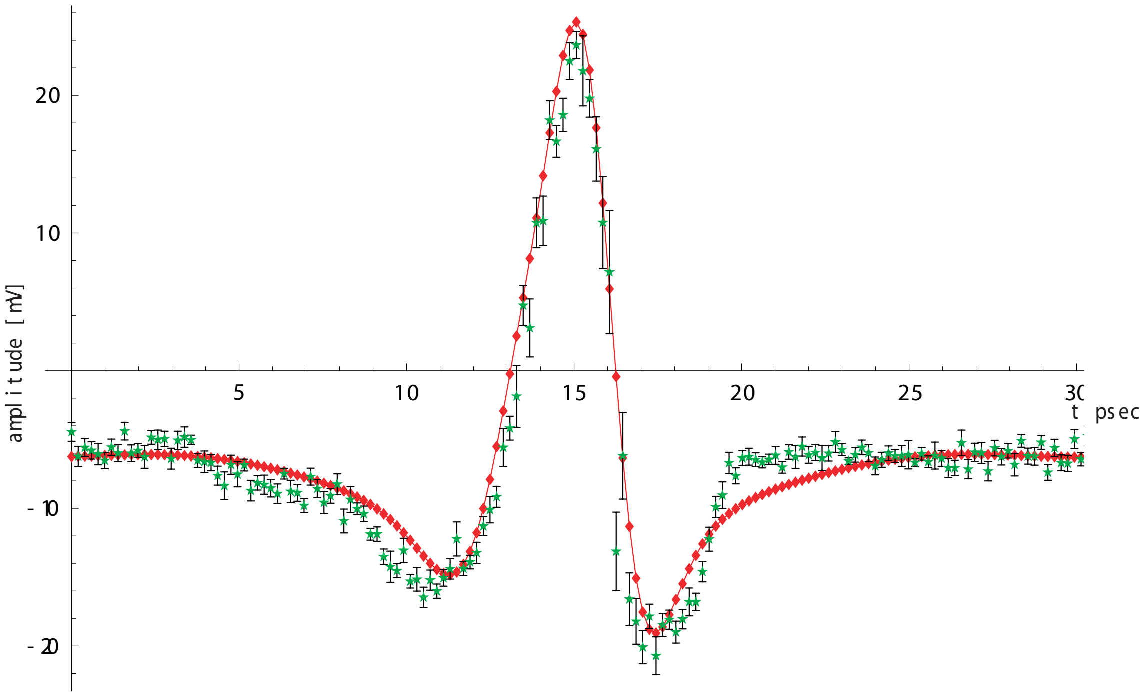

(a) Fit using 2 Gaussian distributions

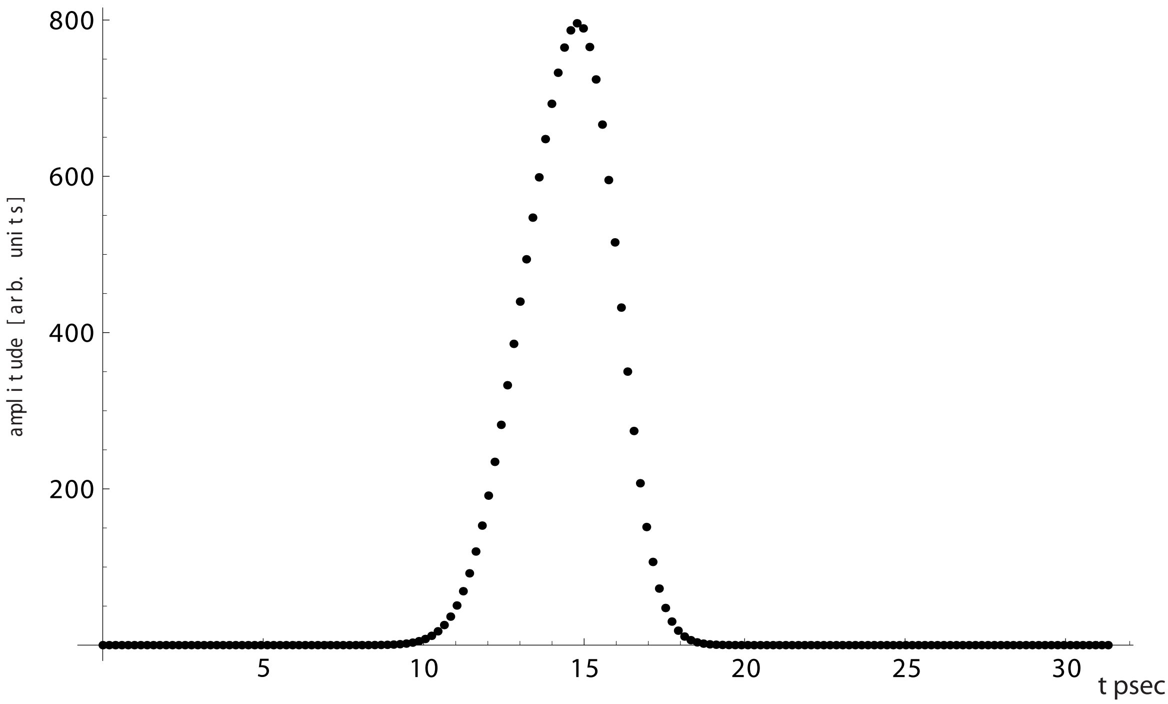

(b) Reconstructed pulse shape

Figure 7.10.: Fit results with 2 Gaussian model for measurement B

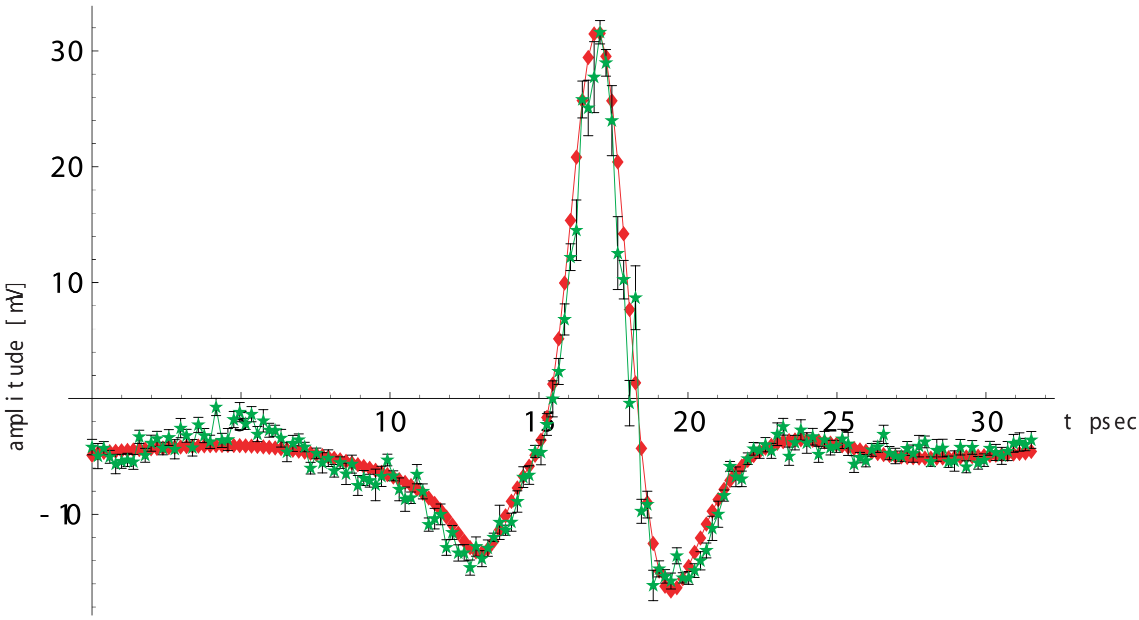

(a) Fit using 3 Gaussian distributions

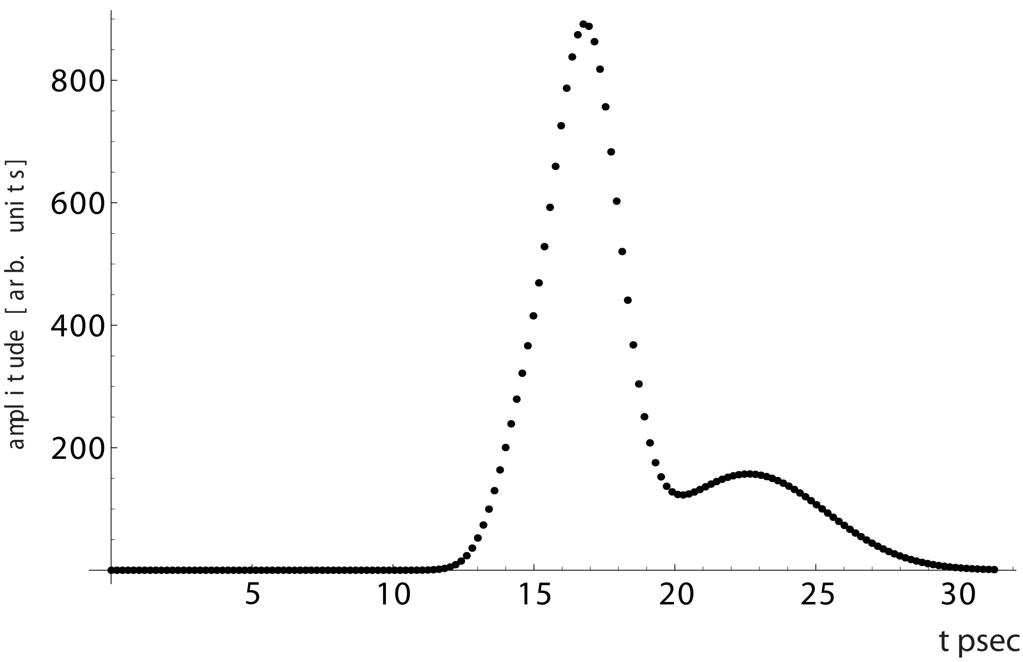

(b) Reconstructed pulse shape

Figure 7.11.: Fit results for 3 Gaussian model for measurement A

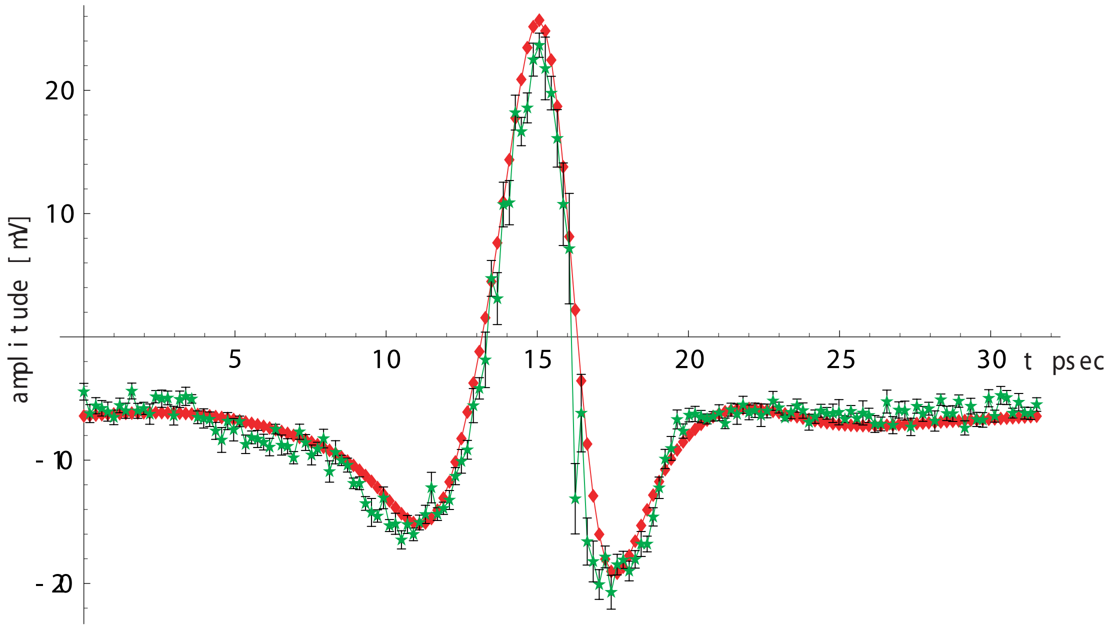

(a) Fit using 3 Gaussian distributions

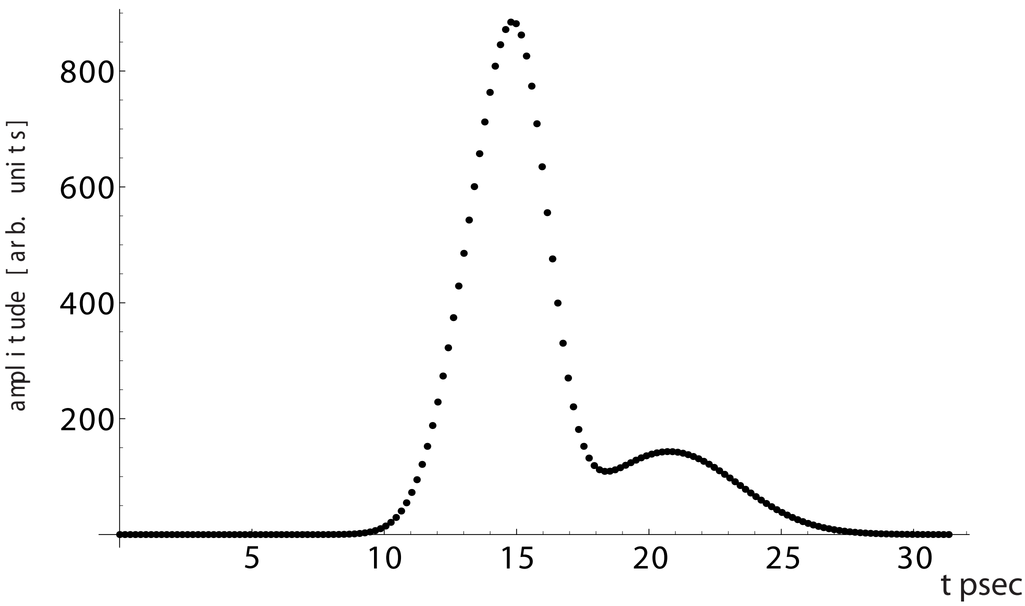

(b) Reconstructed pulse shape

Figure 7.12.: Fit results for 3 Gaussian model for measurement B

	meas. A	meas. B
A_1	868	535
σ_1 [ps]	1.19	1.45
t_1 [ps]	16.83	13.94
A_2	157	482
σ_2 [ps]	2.75	1.08
t_2 [ps]	14.65	15.33
A_3	173	145
σ_3 [ps]	2.26	1.34
t_3 [ps]	22.61	20.76
$\lvert\Delta_{1-2}t\rvert$ [ps]	2.18	1.39
$\lvert\Delta_{1-3}t\rvert$ [ps]	5.78	6.82

Table 7.3.: Fit parameters for 3 Gaussian distributions model

for the three Gaussian distributions in figure 7.11 and 7.12, the fit parameters in table 7.3.

This means that for measurement A 0.126 nC and for measurement B 0.078 nC of the bunch charge is accumulated in the tailing Gaussian, assuming a total charge of 0.6 nC per bunch. This method describes the measured time profiles very well, but the significance of the small tailing Gaussian is marginal. Figure 7.13 shows for measurement B the area of the tailing Gaussian, which is proportional to the charge, versus the χ^2 of the fit. One can see, that the 1 sigma confidence level is compatible to charge in the tailing Gaussian of between 0 nC (so no tailing Gaussian at all) and 0.140 nC. It is thus not possible to draw a definite conclusion for the shape of the bunch as the significance of the area of the second peak is small. The experience from SLS operation rather suggests a bunch shape more compatible with the 2 Gaussian analysis, but this experience was not derived from direct measurements but concluded indirectly.
Additional fits can be found in appendix A.

One possible explanation for the second peak in the beam profile might be a reflection of the CTR radiation at the ZnTe crystal surface or the the window of the vacuum chamber. The thickness of the fused silica window is 4.3 mm, so a reflection of the CTR radiation (index of refraction $n_{window} = 2.11$) should arrive

$$\Delta t_{window} = \frac{2.11 \cdot 2 \cdot 4.3 \cdot 10^{-3}\,\mathrm{m}}{3 \cdot 10^{8}\,\frac{\mathrm{m}}{\mathrm{s}}} = 60.5\,\mathrm{ps}, \tag{7.3}$$

after the actual signal. The same calculation yields for a reflection in the crystal (thickness of 1 mm, $n_{crystal} = 3$)

$$\Delta t_{crystal} = \frac{3 \cdot 2 \cdot 1 \cdot 10^{-3}\,\mathrm{m}}{3 \cdot 10^{8}\,\frac{\mathrm{m}}{\mathrm{s}}} = 20\,\mathrm{ps}. \tag{7.4}$$

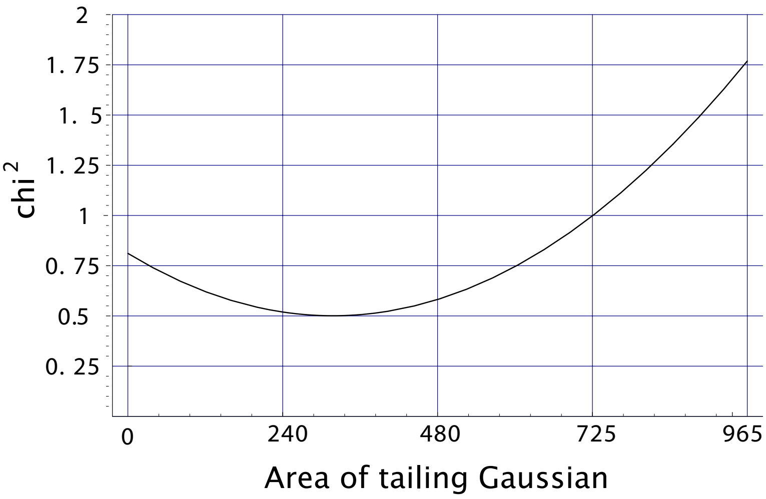

Figure 7.13.: Plot of the area versus χ^2 of the tailing Gaussian

Both effects produce secondary peaks outside the measured timespan and cannot contribute to the measured signal.
It is conceivable, that the laser emits a double pulses which are responsible for the second pulse in the measurement. This could be determined with an autocorrelator, which was not at our disposal during the measurements.

7.4. Temporal stability and resolution

Timing jitter

It is possible to give an estimate on the temporal resolution of this experiment including all jitters. The idea is to measure the amplitude jitter of the balanced detector output with an electro-optical signal present, when the phase between laser pulse and bunch is such, that the laser pulse is at the rising or falling edge of the CTR signal. The amplitude jitter is then dominated by the arrival time jitter of consecutive bunches in the linac. Such a measurement is shown in figure 7.14. The measurement was taken over 100 bunches, which at a repetition rate of the linac of 3.125 Hz amounts to a total time of 5 minutes.
Assuming a linear dependency between time and amplitude on the flank of the signal, it is possible to obtain a measurement for the timing jitter of the experiment including all effects from other sources of timing jitter (e.g. the gun). The measurement shown in figure 7.14 has an rms jitter of 8.9 units. This corresponds to a timing jitter of

$$\sigma_t = 330\,\text{fs (rms)} \tag{7.5}$$

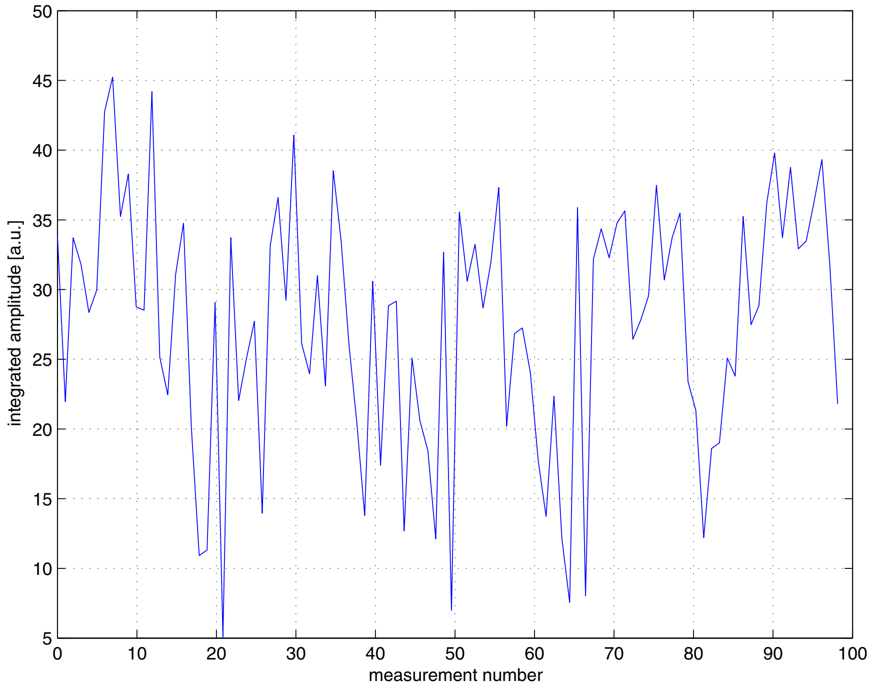

Figure 7.14.: Amplitude jitter of the measurement signal where the laser pulse is on the flank of the electro-optic signal

Measurement reproducibility

Figure 7.15 shows two measurements which were conducted directly after on another with positive and negative phase steps but otherwise identical parameters. Both measured curves are almost identical, which suggests that there was no significant drift during a period of 9 minutes (which is the time one measurement takes).

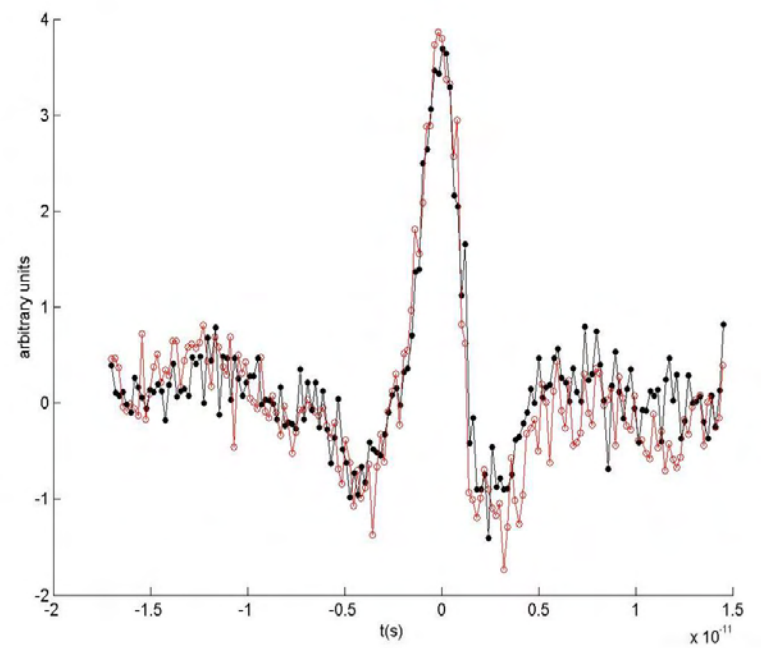

Figure 7.15.: Two measurements taken directly after one another with positive and negative phase steps respectively

8. Conclusion and outlook

The electro-optic technique offers the possibility of bunch length measurements of highly relativistic electron bunches in an accelerator with subpicosecond resolution. An experiment sampling the coherent transition radiation has been carried out at the 100 MeV linac of the Swiss Light Source. The temporal resolution of the experiment was better than 300 fs (rms). The results allow the reconstruction of the bunch shape using the computed transfer function of the CTR from the transition radiation screen to the ZnTe crystal. The bunch shape can be well described by using a superposition of two respectively three Gaussians. The bunch lengths measured are in good agreement with the predictions based on indirect measurements.

An optical beam transfer line was developed, allowing a stable transmission of the femtosecond laser pulses from the outside of the bunker into the linac.

One of the key elements for the successful measurement is the synchronisation unit. It allows the synchronisation of the 81 MHz repetition frequency of the 15 fs laser with the 500 MHz linac RF with a stability of less than 40 fs. This stability is close to the technical limit achievable with analogue controllers and the laser used. Further improvement of the synchronisation accuracy is possible by employing a digital control scheme and exchanging the piezo movable mirror inside the laser cavity. This is planned for the next generation of the synchronisation used for the electro-optic sampling experiment at TTF2.

The EOS experiment at TTF phase 2 will have the crystal mounted inside the vacuum pipe to increase the resolution. This furthermore has the advantage, the EOS experiment can be operated without a transition radiation screen that intercepts the electron beam. Hence bunch length measurement can be carried out in parallel to FEL operation.

One conclusion from the experience at the SLS is, that a crystal thickness of 1 mm is already limiting the spatial resolution of the electro optic sampling to 2.5 ps (FWHM). Thus is is essential to use a thinner ZnTe crystal to measure the significantly shorter bunches at TTF2. Another option might be to choose a different crystal material, e.g. GaP which has a higher intrinsic resonance frequency than ZnTe (10 THz compared to 5.3 THz) and thus allows the measurement of shorter bunches.

A. Additional measurements

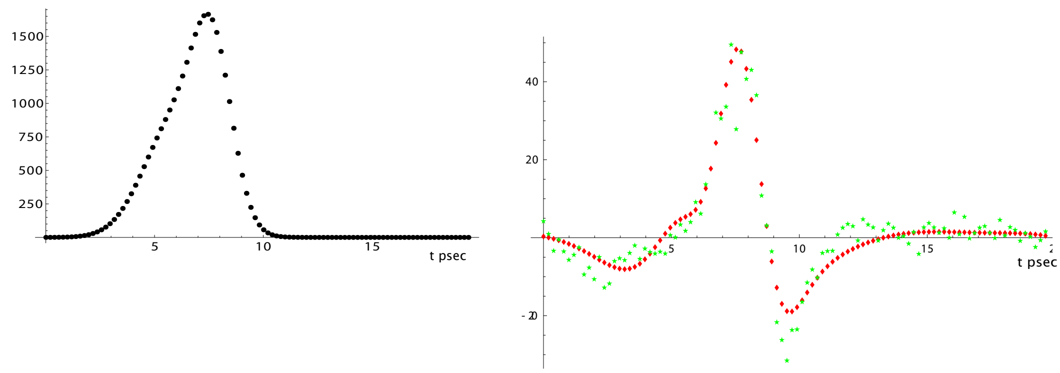

Figure A.1.: Left: reconstructed pulse shape using two Gaussians; right: measured data and resulting fit. Measurement taken without averaging.

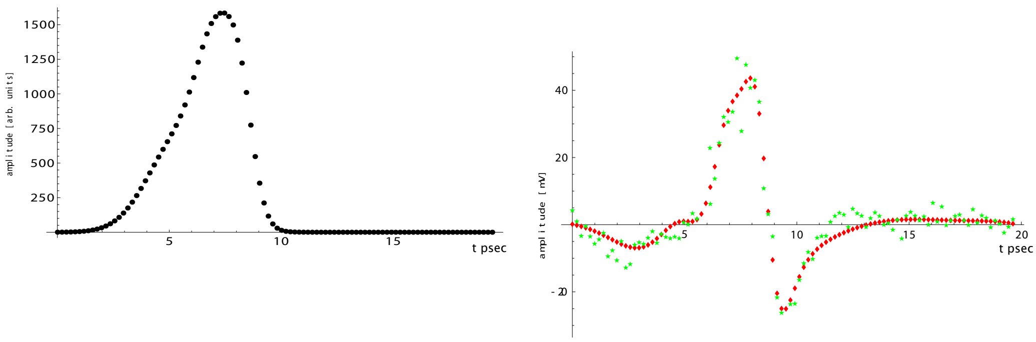

Figure A.2.: Left: reconstructed pulse shape using three Gaussians; right: measured data and resulting fit. Measurement taken without averaging.

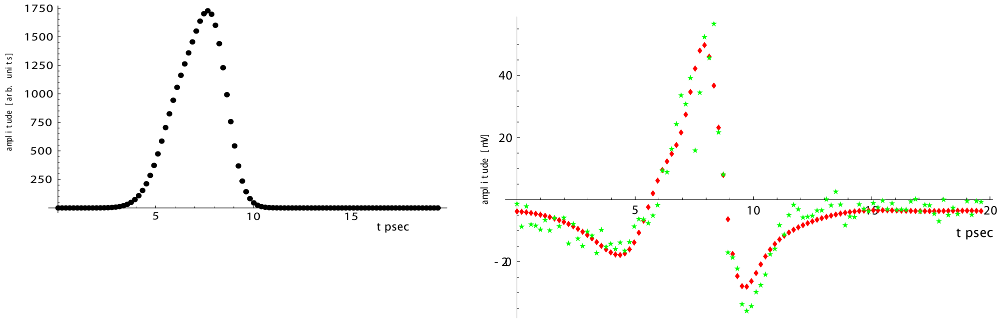

Figure A.3.: Left: reconstructed pulse shape using two Gaussians; right: measured data and resulting fit. Measurement taken without averaging.

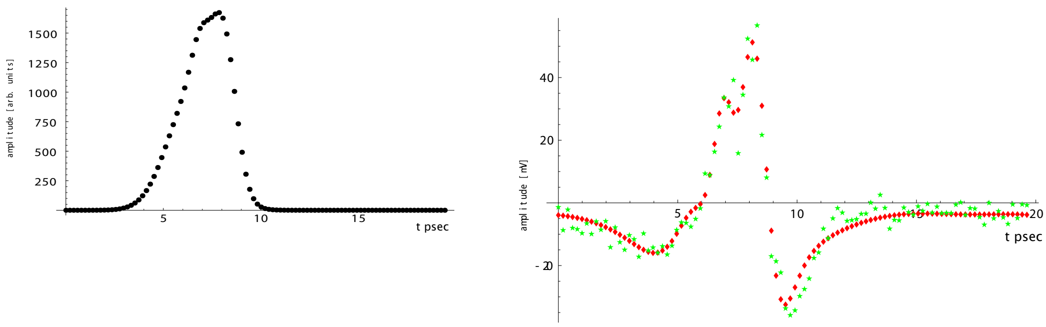

Figure A.4.: Left: reconstructed pulse shape using three Gaussians; right: measured data and resulting fit. Measurement taken without averaging.

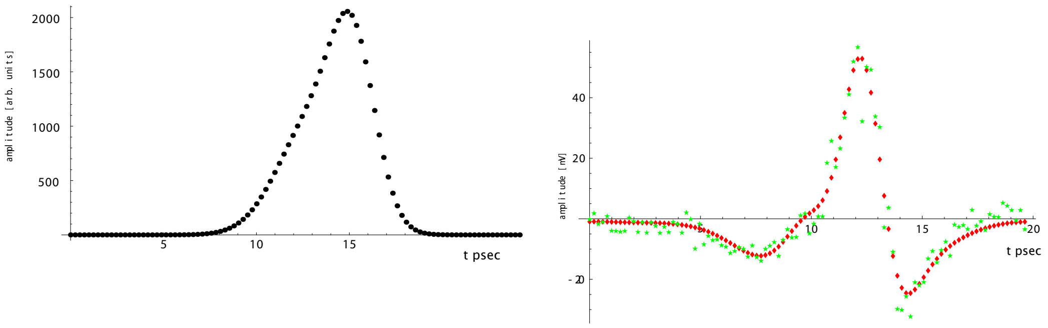

Figure A.5.: Left: reconstructed pulse shape using two Gaussians; right: measured data and resulting fit. Measurement taken without averaging.

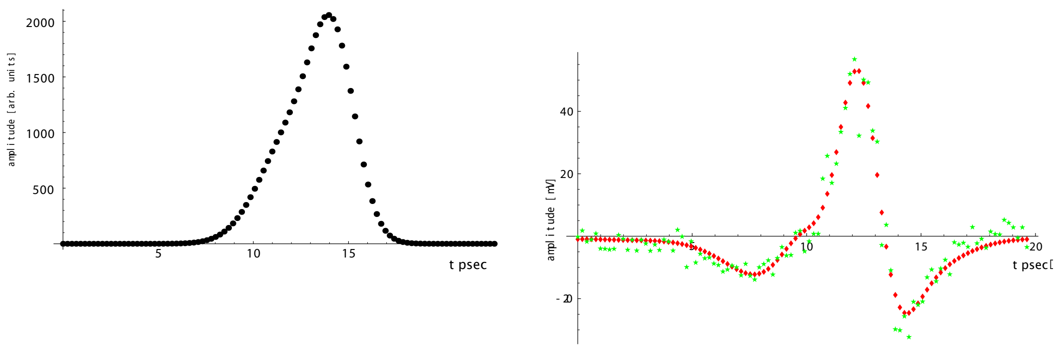

Figure A.6.: Left: reconstructed pulse shape using three Gaussians; right: measured data and resulting fit. Measurement taken without averaging.

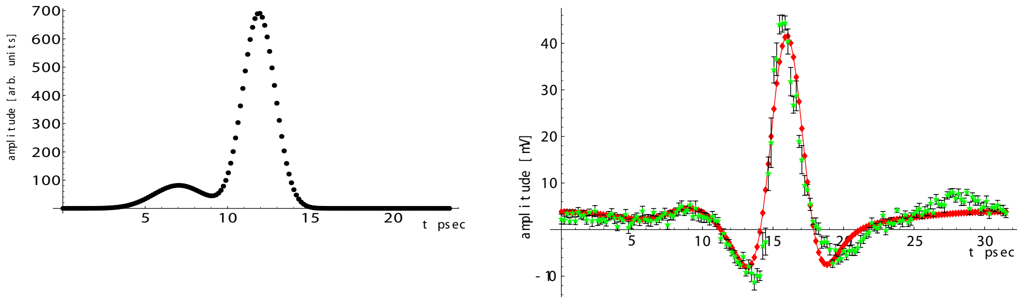

Figure A.7.: Left: reconstructed pulse shape using two Gaussians; right: measured data and resulting fit.

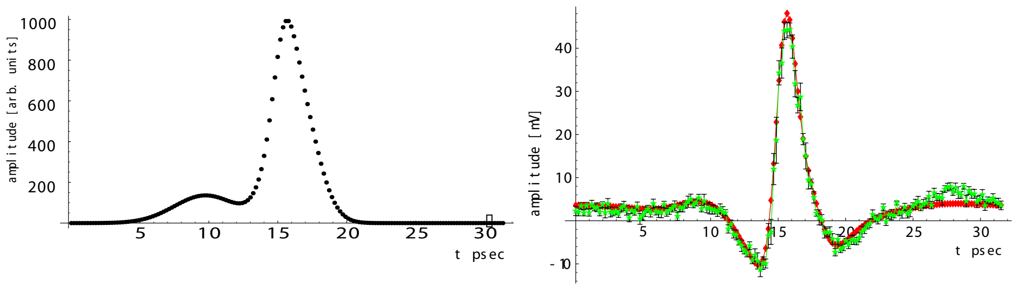

Figure A.8.: Left: reconstructed pulse shape using three Gaussians; right: measured data and resulting fit.

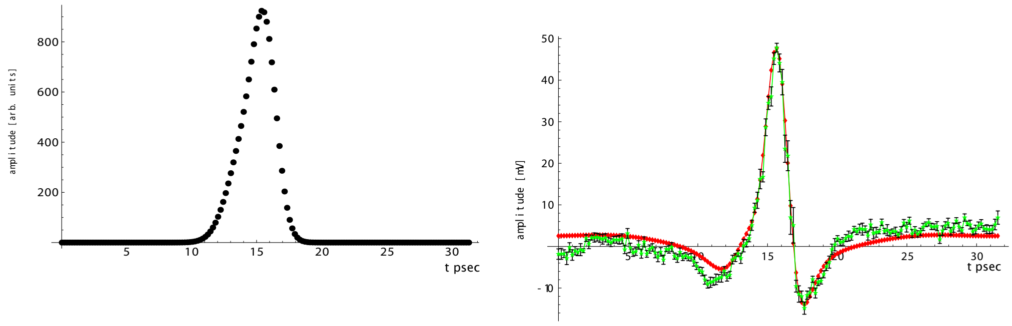

Figure A.9.: Left: reconstructed pulse shape using two Gaussians; right: measured data and resulting fit.

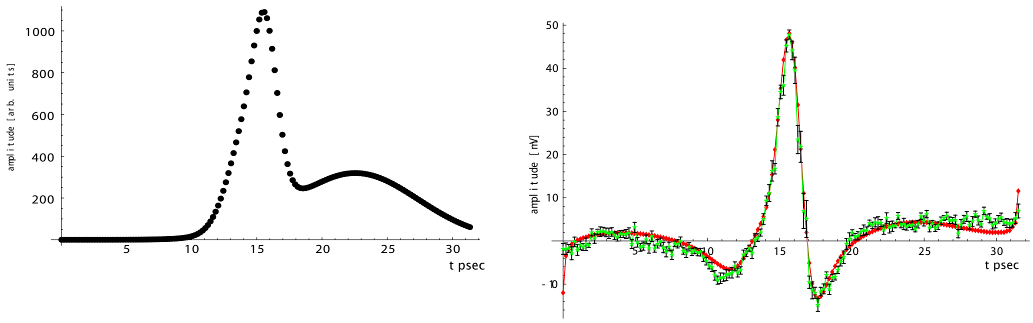

Figure A.10.: Left: reconstructed pulse shape using three Gaussians; right: measured data and resulting fit.

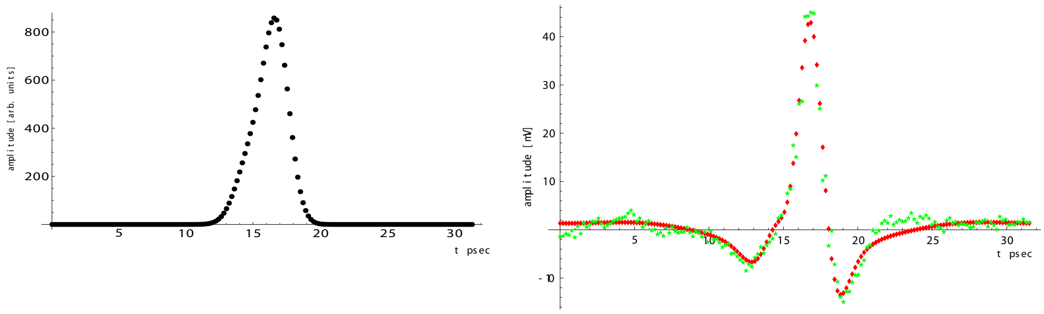

Figure A.11.: Left: reconstructed pulse shape using two Gaussians; right: measured data and resulting fit. Measurement taken without averaging.

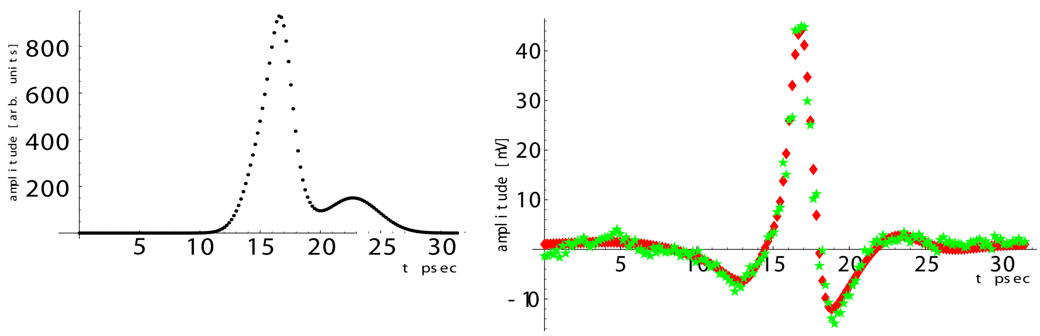

Figure A.12.: Left: reconstructed pulse shape using three Gaussians; right: measured data and resulting fit. Measurement taken without averaging.

B. Schematics of PI controller and vector modulator driver

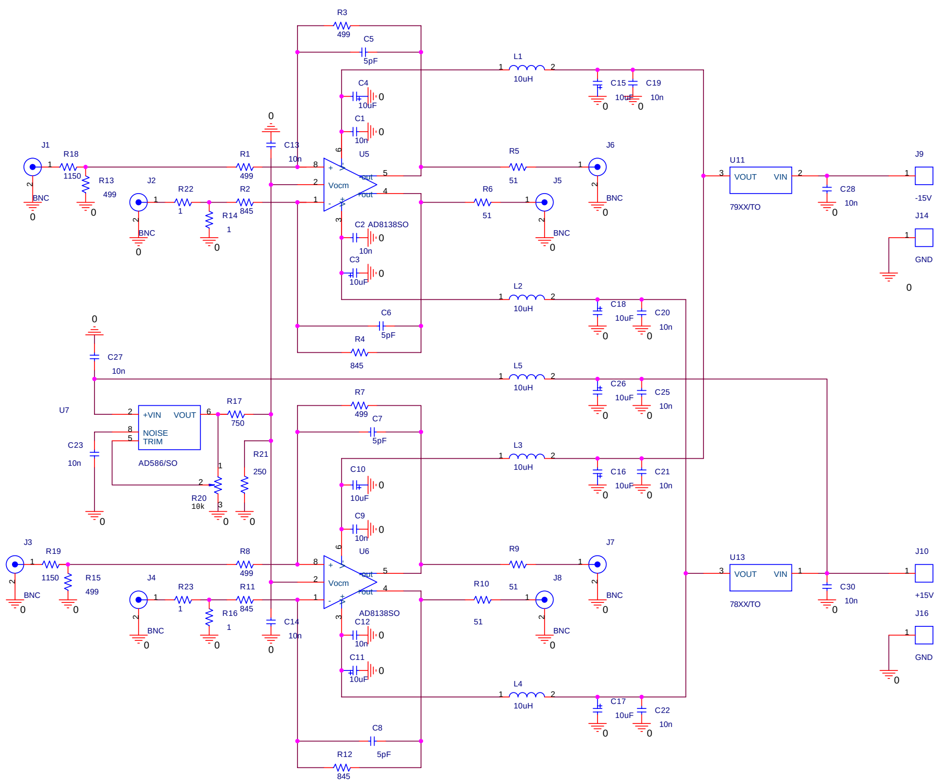

Figure B.1.: Schematic of the vector modulator driver

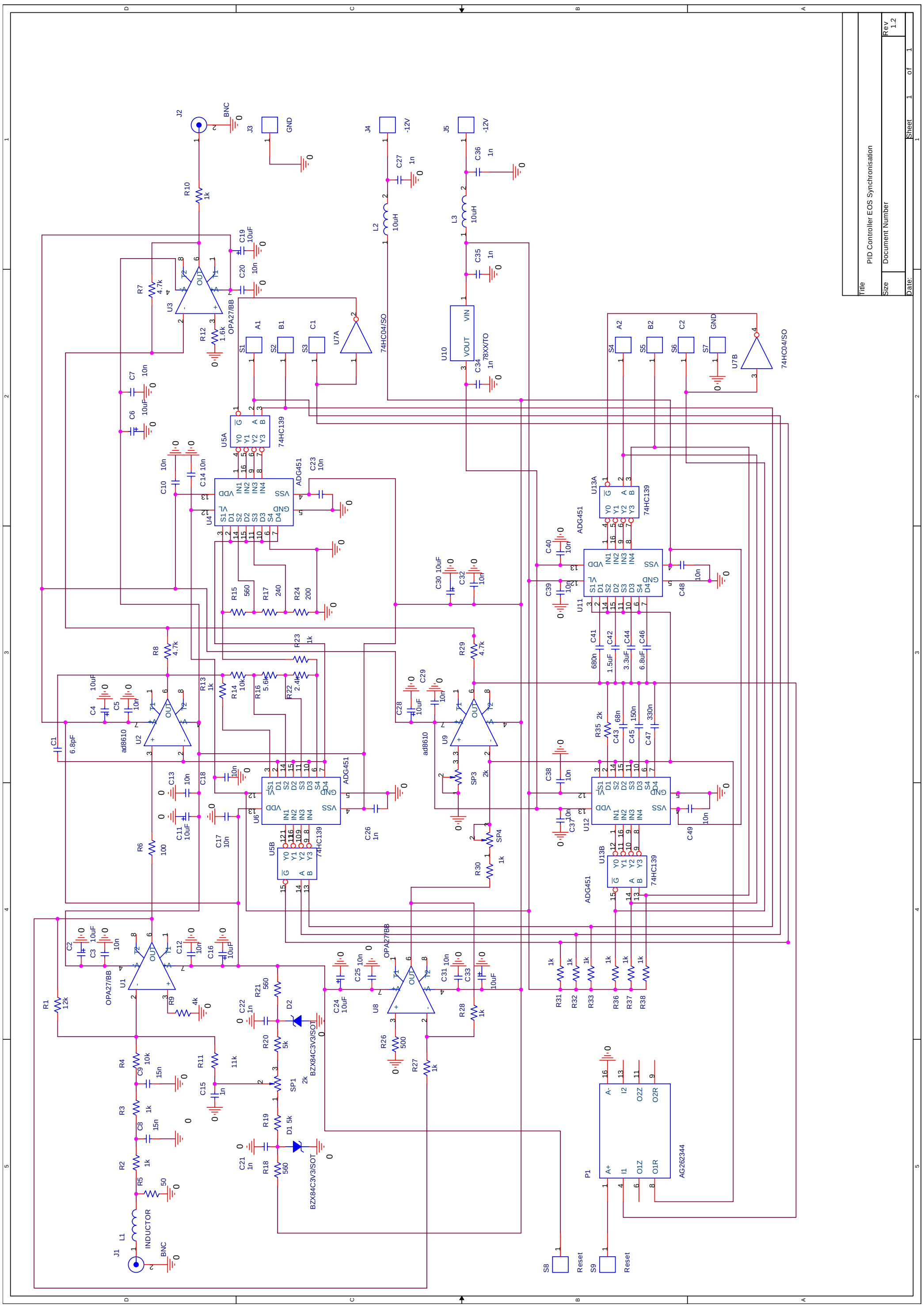

Figure B.2.: Schematic of the PI controller

List of Figures

List of Tables

Bibliography

[Bak98] BAKKER ET. AL., H. J.: *Distortion of terahertz pulses in electro-optic sampling.* Journal of the Optical Society of America B, 15:17951801, 1998.

[BG00] BOLOTOVSKY, B. M. and E. A. GALST'YAN: *diffraction and diffraction radiation.* Dokl. Phys., 43:755–775, 2000.

[Bri02] BRINKMANN ET. AL.(EDITORS), R.: *TESLA XFEL Technical Design Report Supplement.* Technical Report, 2002.

[Bru03] BRUNKEN ET. AL., M.: *Electro-Optic Sampling at the TESLA Test Accelerator: Experimental Setup and First Results*, volume II. DESY, 2003. TESLA Report 2003-11.

[Cri99] CRIPPS, STEVE C.: *RF Power Amplifiers for Wireless Communications.* Artech House Massachusettes, 1 edition, 1999.

[Gei99] GEITZ, M.: *Investigation of the Transverse and Longitudinal Beam Parameters at the TESLA Test Facility Linac.* PhD thesis, Hamburg University, 1999. DESY-THESIS-1999-033.

[HaSS01] HONKAVAARA, K. and P. POIT AND S. SCHREIBER: *Bunch Length Measurements at the TESLA Test Facility using a Streak Camera.* In *proceedings of PAC 2001*, Chicago, 2001.

[HP98] HERZIGER, GERD and REINHART POPRAWE: *Lasertechnik I.* Fraunhofer Institut fuer Lasertechnik, Aachen, 1998. Vorlesungsscript.

[Jac99] JACKSON, J.D.: *Classical Electrodynamics.* John Wiley and Sons, Inc., 3 edition, 1999.

[J.L96] J.LUNZE: *Regelungstechnik I.* Springer Verlag Berlin, Heidelberg, 1 edition, 1996.

[LL85] LANDAU, L.D. and E.M. LIFSCHITZ: *Elektrodynamik der Kontinua.* In *Lehrbuch der Theoretischen Physik*, volume VIII. Akademie-Verlag Berlin, 1985.

[Maa88] Maas, Stephen A.: *Nonlinear Microwave Circuits.* Artech House Massachusettes, 1 edition, 1988.

[Oep99] Oepts et. al., D.: *Picosecond electronbunch length measurement using an electro-optic sensor.* In *Proceedings of the 21st International FEL Conference*, Hamburg, 1999.

[Pau04] Paul Scherrer Institute. http://sls.web.psi.ch/index.html, 2004.

[PH00] Phillips, Charles L. and Royce D. Harbor: *Feedback Control Systems.* Prentice Hall, New Jersey, 4 edition, 2000.

[Rul98] Rullière, C. (editor): *Femtosecond Laser Pulses, Principles and Experiments.* Springer, Berlin Heidelberg New York, 1998.

[SSSJ03] Suetterlin, D., V. Schlott, H. Sigg and H. Jackel: *Development of a Bunch-Length Monitor with Sub-Picosecond Time Resolution and Single-Shot Capability.* In *Proceedings of the DIPAC 2003*, Darmstadt, Germany, 2003.

[Sue04] Suetterlin, Daniel. private communication, 2004.

[YY84] Yariv, Amnon and Pochi Yeh: *Optical Waves in Crystals - Propagation and Control of Laser Radiation.* John Wiley & Sons, New York, 1984.

Acknowledgements

Without the great support I was given during the course of this thesis, its completion would not have been possible.

Firstly I would like to thank Prof. Dr. Manfred Tonutti for his encouragement to come to Hamburg and work in the field of beam diagnostics and for the weeks spent measuring at the SLS.

Secondly my thanks go to Prof. Dr. Peter Schmüser for his effort and enthusiasm in supporting my thesis in Hamburg. Without the many fruitful discussions and constructive ideas the measurements at the SLS would not have shown such good results.

My sincere thanks go to Dr. Stefan Simrock. With his many ideas, countless discussions and his formidable knowledge in low level RF regulation, the design of the synchronisation unit would not have been possible.

The results of these discussions were converted into PCB boards by Nikolai Ignashine and Sergey Sytov. Without the many nights spent, the last minute alterations would not have been possible.

My thanks go to Dr. Sara Casalbuoni for her help in getting ZEMAX to do what we wanted and for the many shifts spent measuring at the SLS.

Many thanks go to Dr. Holger Schlarb for many helpful discussions, Jan Menzel for answering my a lot of questions about analogue and digital circuits, Dr. Rasmus Ischebeck for helping me cope with Tex problems, ZEMAX, Matlab scripts and life in general, to Dr. Axel Knabbe for many fruitful discussions and to Dr. Bernhard Schmidt for his help with the simulation results and for many stimulating discussions. Finally, I am greatful for the help of Mrs. Ingrid Nikodem in coping with the DESY administration.

The help and support for the measurement by the people from the Swiss Light Source was exceptional. Without the help of Daniel Sütterlin and Dr. Volker Schlott the measurements would not have gone so well. For a lot of help with the SLS timing system my thanks go to Dr. Thomas Schilcher and Dr. Timo Korhonen. I am also greatful to Peter Hottinger for his help in performing the vibration measurements, to the SLS operators staff for their uncomplicated help and to Patrick Pollet for granting us asylum in his precious diagnostic hutch.

Special thanks go to Bernd Steffen for his big effort in making the measurements possible. Working closely together for almost a year and spending many weekends and night shifts together would not have been as easy as it was without his continuing support and the continuous motivation resulting from it.

Last but not least I would like to thank my family, colleagues and friends for their support and tolerance of my lack of communication during the last months.

Erklärung

Hiermit erkläre ich, diese Arbeit selbständig verfasst zu haben. Andere als die angegebenen Quellen und Hilfsmittel habe ich nicht benutzt.

Hamburg, im Juni 2004

(Axel Winter)